

1 2 9 0



UNIVERSIDADE D
COIMBRA

Isidro Gabriel Coelho Ribeiro

DYNAMIC INDUCTIVE POWER TRANSFER
SYSTEM IMPLEMENTED IN THE WHEELS
OF ELECTRIC VEHICLE

Master's Dissertation in Electrical and Computer Engineering, in the field of Energy supervised by Professor Doctor André Manuel dos Santos Mendes, co-supervised by Professor Doctor Marina Mendes Sargento Domingues Perdigão and presented to the Department of Electrical and Computer Engineering of Faculty of Sciences and Technology of University of Coimbra.

February of 2024



UNIVERSIDADE D
COIMBRA

**Dynamic Inductive Power Transfer
System Implemented in the Wheels of
Electric Vehicle**

Isidro Gabriel Coelho Ribeiro

Coimbra, February of 2024



FACULDADE DE
CIÊNCIAS E TECNOLOGIA
UNIVERSIDADE DE
COIMBRA

Dynamic Inductive Power Transfer System Implemented in the Wheels of Electric Vehicle

Dissertation supervised by Professor Doctor André Manuel dos Santos Mendes and submitted to the Electrical and Computer Engineering Department of the Faculty of Science and Technology of the University of Coimbra, in partial fulfilment of the requirements for the Master Degree in Electrical and Computer Engineering, specialization in Energy.

Supervisor:

Prof. Dr. André Manuel dos Santos Mendes

Co-Supervisor:

Prof. Dr. Marina Mendes Sargento Perdigão

Jury:

Prof. Dr. Sérgio Manuel Ângelo da Cruz
Prof. Dr. André Manuel dos Santos Mendes
Prof. Dr. Fernando José Teixeira Estêvão Ferreira

Coimbra, February of 2024

Acknowledgements

I would like to thank my supervisor, Professor André Mendes, that accompanied me throughout the project and provided me all the necessary material to the project. He always tried to develop in me a critical thinking and a certain level of autonomy in the project, providing me good teachings for all areas of life.

To my co-supervisor, Professor Marina Perdigão, for her support throughout the project and also for having a crucial role in connecting all the project branches and fostering connections among all team members.

To my laboratory colleagues, Valter Costa, who consistently demonstrated total availability to assist with my challenges and to Miguel Torres, whose support from the very beginning of this thesis development has been fundamental to my personal and professional growth.

I also extend my gratitude to my family, for all the unconditional support, trust, and love. They have been exemplary role models, and I only regret not always following their advice. I hope to be able to reciprocate a bit of what you represent for me.

To my girlfriend, Patrícia Martins, who has stayed by my side in all moments, offered me all the support that I could ask for, and reminded me that anything is possible to achieve. Without you, I wouldn't have made it.

Last but certainly not least, I would like to thank to all my friends, especially to Quantunna and Eletrões, and particularly to Arsénio, Castilho, Crosta and Polinómio, whom I shared great moments. Also, for making Coimbra feels like a new home for me. I will carry each of you with me for life.

Resumo

Os Veículos Elétricos (EV) estão a crescer em popularidade. Contudo, problemas relacionados com o armazenamento de energia e processos de carregamento são frequentemente alvos de preocupações e inconveniências. Tecnologias de Transferência de Energia Sem Fios oferecem soluções para vários desses problemas, principalmente relacionados com o conforto e segurança, permitindo os EV carregarem sem a interferência do utilizador. A tecnologia de Transferência de Energia por Indução (IPT) é recorrentemente utilizada em aplicações no setor dos transportes.

O carregamento pode ser estático, onde o EV permanece imóvel, ou dinâmico, onde o EV está em movimento. As aplicações dinâmicas IPT, para além dos benefícios do IPT estático, também permitem a redução da quantidade de baterias e eliminam as preocupações relacionadas com o tempo de carregamento. Contudo, o IPT dinâmico necessita de infraestruturas de carregamento especializadas, incluindo bobinas embebidas na estrada, para transferirem energia para o EV em movimento. O desalinhamento inevitável com o movimento do EV, e o desalinhamento vertical e lateral, levam a diferentes condições de acoplamento, que vão desde alinhado até completamente desalinhado.

No sistema in-wheel Inductive Power Transfer (inWIPT), a roda age como acoplamento intermediário, permitindo a transferência de energia para o veículo. O sistema sugerido minimiza o entre-ferro utilizando dois acoplamentos magnéticos para a transferência de energia, um da estrada para a roda e outro da roda para o veículo, sendo o entre-ferro quase independente do tipo de carro.

Esta dissertação apresenta o estudo e validação do sistema inWIPT para aplicações dinâmicas. Como ponto de partida, foi utilizada uma topologia ressonante já estudada e validada para aplicações dinâmicas, o Bobina-Condensador-Bobina-Série-Série (LCL-S-S). Para introduzir o tema, um panorama atual do carregamento de EV, uma revisão dos sistemas IPT e uma descrição do inWIPT foram realizados.

Posteriormente, é conduzido um estudo das indutâncias próprias e mútuas para os dois acoplamentos para diferentes condições, resultando num conhecimento dos limites físicos do sistema. Uma simulação foi desenvolvida, numa primeira instância, para o dimensionamento do sistema e segurança de implementação, e posteriormente para o estudo do comportamento do sistema.

Para culminar, um protótipo à escala real foi construído e testado para o funcionamento estático e dinâmico, de modo a provar o conceito e validar o modelo de simulação. Adicionalmente, uma comparação prática entre três topologias ressonantes foi conduzida.

Palavras-Chave: Transferência de Energia Sem Fios, Transferência de Energia por Indução, Veículos Elétricos, Carregamento Dinâmico

Abstract

Electric Vehicles (EV) are growing in popularity. However, issues related to energy storage and the charging process are frequently a target of concerns and inconveniences. Wireless Power Transfer (WPT) technology offers solutions to many of these problems, mainly on the field of comfort and safety, allowing EVs to charge without user intervention. The Inductive Power Transfer (IPT), a prevalent form of WPT technology, is extensively used for applications on the transportation sector.

The charge process can be static, where the vehicle remains stationary, or dynamic, where the car is in motion. Dynamic IPT application not only retains the benefits of static IPT but also allows for the reduction of the quantity of batteries and remove the concerns related with the time of charge. However, dynamic IPT require a specialized charging infrastructure, including coils implemented in the road, to transfer energy to the moving EV. Inherent displacements in the travel direction, as well as the already expected vertical and lateral misalignments, lead to different coupling conditions, ranging from no-coupling to full-coupling.

In the in-wheel Inductive Power Transfer (inWIPT) system, the wheel acts as an intermediary on a double coupling system, facilitating wireless energy transfer to the EV. The suggested system minimizes the air gap by employing two Magnetic Couplers (MC) for the energy transfer, one from the off-board side to the wheel and another from the wheel to the on-board side, and is nearly independent of the vehicle type.

This dissertation presents the study and validation of the inWIPT for dynamic applications. As a starting point, an already studied and suitable for dynamic operation resonant topology was used, the Inductor-Capacitor-Inductor-Series-Series double coupling Compensation Topology (LCL-S-S). A state of the art of the EV charging, an overview of IPT systems, and a description of the inWIPT introduce the theme, focusing on the key topics.

A study of the self/mutual inductances of both MC and coupling profiles for different characteristics was conducted, leading to an understanding of the limits of the physical model. A simulation model was developed, initially, as a safety precaution and sizing of the system, and then to study the behaviour of the inWIPT.

To culminate all the work, a real-scale prototype was developed and tested for static and dynamic operation in order to prove the concept and validate the simulation model. Additionally, a practical comparison between three resonant topologies was conducted.

Keywords: Wireless Power Transfer, Inductive Power Transfer, Electric Vehicle, Dynamic Charging

Contents

Acknowledgements	i
Resumo	ii
Abstract	iii
List of Acronyms	vii
List of Figures	xii
List of Tables	xiv
List of Symbols	xix
1 Introduction	1
1.1 Wireless Charging Systems	3
1.2 Motivation and Main Objectives	5
1.3 Document Outline	6
2 Inductive Power Transfer	7
2.1 Working Principles	7
2.2 Magnetic Coupler Structure	9
2.2.1 Long or Segmented Pads	9
2.2.2 Pad Geometries	10
2.2.3 Ferromagnetic Core and Shielding	11
2.3 Resonant Topology	11
2.4 Quality Factor	13
3 Double Coupling IPT System	15
3.1 Multiple coupling IPT systems	16
3.2 ORMC and IRMC	17
3.3 Magnetic Couplers Configurations	18
3.4 Analysis of LCL-S-S Topology	20
3.4.1 Circuit Analysis	21
4 Electromagnetic Characterization	23
4.1 Experimental measurement and calculation	23
4.2 Prototype	25
4.3 Experimental Results	26
4.3.1 Inner Rim Magnetic Coupler	26
4.3.2 Outer Rim Magnetic Coupler	28
5 Simulation	34
5.1 Software	34
5.2 Model	34

CONTENTS

5.2.1	Magnetic Couplers	34
5.2.2	Position Determination	37
5.2.3	Power Converters	38
5.3	Results	39
6	Experimental Validation	43
6.1	System Specifications	43
6.1.1	Power Converters	44
6.2	Results	45
6.2.1	LCL-S-S	46
6.2.2	Additional Resonant Topologies	51
7	Conclusion	57
A	Prototype Model Specifications	61
B	Detailed Results from Chapter 4	62
B.1	Dependency between ORMC and IRMC	62
B.2	IRMC	63
B.2.1	Impact of rotation between transmitter and receiver	63
B.2.2	Impact of the Coil Width/SBT	63
B.2.3	Impact of the number of turn in each coil	64
B.3	ORMC	65
B.3.1	Impact of the wheel entry angle and the misalignment on y axis for DDP-SP	65
B.3.2	Impact of the misalignment in y axis for DDP—SP, with different misalignments.	72
C	Detailed Results from Chapter 5	82
C.1	Measurement Blocks and Calculations	82
C.2	Impact of the Velocity	82
C.2.1	Time framed	82
C.2.2	Number of transmitter pads	86
C.3	Different Source Arrangements	89
D	Detailed Results from Chapter 6	91
D.1	Polarity test	91
D.2	Experimental Results	92
D.2.1	LCL-S-S	92
D.2.2	S-S-S	93
D.2.3	LCC-S-S	94

List of Acronyms

AC Alternating Current. 7, 8, 17, 38

BPP Bipolar Pad. 57

CP Circular Pad. 10, 11, 36

CPT Capacitive Power Transfer. 4, 5

DC Direct Current. 7, 15, 20, 38, 42, 46, 48

DDP Double-D Pad. v, viii, 6, 11, 18, 19, 28, 29, 31, 36, 62, 63, 65–81

EMI Electromagnetic Interference. 4, 10, 11, 17, 25, 57

EV Electric Vehicle. ii, iii, viii, 1, 2, 4–6, 9, 11, 15, 16, 21, 37, 43, 82

FEA Finite Element Analysis. 19, 23

FHA First Harmonic Approximation. 20, 21

ICE Internal Combustion Engine. 1, 2

inWIPT in-wheel Inductive Power Transfer. ii, iii, viii, 6, 15–19, 21, 23, 25, 34, 39, 43, 45, 57

IPT Inductive Power Transfer. ii, iii, viii, 4–7, 11, 13, 15–18, 21, 23, 34, 36, 51

IRMC Inner Rim Magnetic Coupler. v, viii, xiii, 6, 16–19, 23, 25–28, 31, 34, 38, 39, 46, 62, 63

LCC-S-S Inductor-Capacitor-Capacitor-Series-Series double coupling Compensation Topology. xiii, 51–54, 57

LCL-S-S Inductor-Capacitor-Inductor-Series-Series double coupling Compensation Topology. ii, iii, ix, xiii, 33, 35, 36, 46, 50–55, 92

MC Magnetic Coupler. iii, 6, 13, 15–17, 20, 23, 25, 26, 34, 43, 44, 62

OPT Optical Power Transfer. 4

ORMC Outer Rim Magnetic Coupler. v, viii, ix, xi, xiii, 6, 16–19, 23, 25, 26, 28–31, 34, 36–42, 44, 46, 48, 49, 51, 52, 55, 57, 61–63, 82, 89–91

PHS Phase Shifting. 21

RFPT Radio Frequency Power Transfer. 4

RMS Root Mean Square. 8

LIST OF ACRONYMS

RP Rectangular Pad. 10, 11

S-S-S Series-Series-Series double coupling Compensation Topology. xiii, 51–53, 92

SBT Space Between Turns. v, viii, xiii, 23, 26, 27, 63, 64

SP Solenoid Pad. v, viii, 6, 11, 18, 19, 28, 29, 31, 62–81

V2G Vehicle-to-Grid. 3

WPT Wireless Power Transfer. iii, 3, 4

List of Figures

1.1	EV cars sales, from 2010 to 2022 [1].	2
1.2	Charging topologies diagram.	5
2.1	Typical structure of a IPT system.	7
2.2	Magnetic fluxes of two inductors in the instantaneous time domain.	8
2.3	Electric equivalent model of the coupling between two coils.	9
2.4	Generic pad constitution.	9
2.5	Placement of transmitter pads on the road. a) Segmented pad; b) Long pad.	10
2.6	Different resonant compensations.	12
2.7	Schematics of: a) Open-circuit test; b) Short-circuit test.	13
3.1	Coil placement: a) Traditional; b) In-Wheel.	15
3.2	Placement of an intermediate coupler in conventional IPT systems.	16
3.3	Schematic diagram of inWIPT system.	18
3.4	Structure of inWIPT system.	18
3.5	ORMC and IRMC placement on the wheel and roadway for the inWIPT system. DDP-SP and SP-SP.	19
3.6	Equivalent circuit model for double coupling inWIPT for LCL-S-S topology.	20
4.1	Circuit connections for measurements: a) L_1 ; b) L_2 ; c) anti-series; d) series;	24
4.2	Experimental inWheel IPT setup. The aluminium structure is on the left, the preliminary wood structure is on the top right, and the back side of the aluminium structure on the bottom right corner.	25
4.3	IRMC pad geometry and placement.	27
4.4	Experimental results for IRMC as function of coil width/Space Between Turns for (a) Self-inductances L_3 and L_4 and, (b) Mutual inductance L_{34} and Coupling factor k_{34}	27
4.5	Experimental results for IRMC as function of the number of turns, considering different air gaps and, ferrite width, for (a) Self-inductances L_3 and L_4 and, (b) Mutual inductance L_{34} and Coupling factor k_{34}	28
4.6	ORMC pad geometry and placement DDP-SP.	29
4.7	Experimental results for ORMC with DDP-SP topology as function of wheel rotation angle, with different misalignment in x axis and different core width, for (a) Self-inductances L_1 and L_2 and, (b) Mutual inductance L_{12} and Coupling factor k_{12}	30
4.8	Movement and rotation of the ORMC receiver relative to the transmitter.	30
4.9	Experimental results for ORMC with DDP-SP topology as function of misalignment in x axis, with different misalignments in y axis, for (a) Self-inductances L_1 and L_2 and, (b) Mutual inductance L_{12} and Coupling factor k_{12}	31
4.10	Experimental results for ORMC with DDP-SP topology with a $y = 0$ mm as function of misalignments in x axis, for (a) Self-inductances L_1 and L_2 and, (b) Mutual inductance L_{12} and Coupling factor k_{12}	32

LIST OF FIGURES

5.1	Overall simulation model of the double-coupling LCL-S-S.	35
5.2	Overall electric schematic of the double-coupling LCL-S-S.	36
5.3	Mutual inductance blocks: a) Simscape library; b) Equivalent model.	37
5.4	One layer of the 3D array, corresponding to data from the mutual inductance of the ORMC (L_{12}) of one air gap ($x_{airgap} = 40 \text{ mm}$).	38
5.5	Electric schematic of: a) the inverter; b) the rectifier.	39
5.6	Simulation results for the impact of the air gap and misalignment. v_{in} , i_{in} , i_1 , i_2 , i_4 , v_{out} , i_{out} , L_{12} and y and z positions.	40
5.7	L_{12} values and results of i_{out} and v_{out} to velocities of 50 and 120 km/h . The "Time framed" represents tests with a d_{pad} of 500 mm and the "n° Transmitter" represents tests with a d_{pad} of 1000 mm	41
5.8	Comparison of simulation results to assess the impact of different sources arrangements. v_{in} , i_{in} and i_2 for the situation d on the first row, f on the second row and e on the third row. v_{out} , i_{out} , L_{12} and x , y and z position on the last row for all situations.	42
6.1	3D model of the prototype.	43
6.2	Final prototype. At the left a full view of the system, and at the right the support bench.	45
6.3	On the left side, a full view of the inverter fully mounted. In the bottom left corner, a back view of one half H-bridge on the assembly phase, the top MOSFET is covered by an insulating film and the bottom one with thermal paste. On the right side, a full view of the rectifier.	45
6.4	Static results for a load of 7,2 Ω on an aligned situation. $a)$ & $c)$ shows v_{in} [50V/div], i_{in} [200mA/div], i_1 [500mA/div] and i_2 [2A/div] in blue, cyan, pink and green, respectively. $b)$ and $d)$ v_{in} [50V/div], i_4 [500mA/div], v_{out} [1V/div] and i_{out} [250mA/div] in blue, orange, red and yellow, respectively.	47
6.5	Static results for a load of 7,2 Ω on an decoupled situation. $a)$ & $c)$ shows v_{in} [50V/div], i_{in} [200mA/div], i_1 [500mA/div] and i_2 [2A/div] in blue, cyan, pink and green, respectively. $b)$ and $d)$ v_{in} [50V/div], i_4 [500mA/div], v_{out} [1V/div] and i_{out} [250mA/div] in blue, orange, red and yellow, respectively.	47
6.6	Dynamic results for a load of 7,2 Ω with a d_{pad} of 500 mm and at 1,6 km/h . $a)$ & $c)$ shows v_{in} [50V/div], i_{in} [200mA/div], i_1 [250mA/div] in blue, cyan and pink, respectively. $b)$ & $d)$ shows i_4 [500mA/div], v_{Req} [5V/div] and v_{out} [2.5V/div] in orange, green and red, respectively.	49
6.7	Dynamic results for a load of 7,2 Ω with a d_{pad} of 500 mm and at 3,2 km/h . $a)$ & $c)$ shows v_{in} [50V/div], i_{in} [200mA/div], i_1 [250mA/div] in blue, cyan and pink, respectively. $b)$ & $d)$ shows i_4 [500mA/div], v_{Req} [5V/div] and v_{out} [2.5V/div] in orange, green and red, respectively.	49
6.8	Dynamic results for a load of 7,2 Ω with a d_{pad} of 1000 mm and at 1,6 km/h . $a)$ & $c)$ shows v_{in} [50V/div], i_{in} [200mA/div], i_1 [250mA/div] in blue, cyan and pink, respectively. $b)$ & $d)$ shows i_4 [500mA/div], v_{Req} [5V/div] and v_{out} [2.5V/div] in orange, green and red, respectively.	50

6.9	Static results for a load of $7,2 \Omega$ on an aligned situation. <i>a</i>) & <i>c</i>) shows v_{in} [50V/div], i_{in} [10A/div], i_1 [10A/div] and i_2 [10A/div] in blue, cyan, pink and green, respectively. <i>b</i>) and <i>d</i>) v_{in} [50V/div], i_4 [5A/div], v_{out} [10V/div] and i_{out} [2A/div] in blue, orange, red and yellow, respectively.	52
6.10	Static results for a load of $7,2 \Omega$ on an aligned situation. <i>a</i>) & <i>c</i>) shows v_{in} [50V/div], i_{in} [2A/div], i_1 [1A/div] and i_2 [5A/div] in blue, cyan, pink and green, respectively. <i>b</i>) and <i>d</i>) v_{in} [50V/div], i_4 [2A/div], v_{out} [5V/div] and i_{out} [1A/div] in blue, orange, red and yellow, respectively.	53
6.11	Static results for a load of $7,2 \Omega$ on an decoupled situation. <i>a</i>) & <i>c</i>) shows v_{in} [50V/div], i_{in} [2A/div], i_1 [1A/div] and i_2 [5A/div] in blue, cyan, pink and green, respectively. <i>b</i>) and <i>d</i>) v_{in} [50V/div], i_4 [2A/div], v_{out} [5V/div] and i_{out} [1A/div] in blue, orange, red and yellow, respectively.	54
6.12	Dynamic results for a load of $7,2 \Omega$ with a d_{pad} of 500 mm at 1,6 km/h. <i>a</i>) & <i>c</i>) shows v_{in} [50V/div], i_{in} [2A/div], i_1 [1mA/div] in blue, cyan and pink, respectively. <i>b</i> & <i>d</i> shows i_4 [1A/div], v_{Req} [10V/div] and v_{out} [5V/div] in orange, green and red, respectively.	55
6.13	Dynamic results for a load of $7,2 \Omega$ with a d_{pad} of 500 mm at 3,2 km/h. <i>a</i>) & <i>c</i>) shows v_{in} [50V/div], i_{in} [2A/div], i_1 [1mA/div] in blue, cyan and pink, respectively. <i>b</i> & <i>d</i> shows i_4 [1A/div], v_{Req} [10V/div] and v_{out} [5V/div] in orange, green and red, respectively.	55
6.14	Dynamic results for a load of $7,2 \Omega$ with a d_{pad} of 1000 mm at 1,6 km/h. <i>a</i>) & <i>c</i>) shows v_{in} [50V/div], i_{in} [2A/div], i_1 [1mA/div] in blue, cyan and pink, respectively. <i>b</i> & <i>d</i> shows i_4 [1A/div], v_{Req} [10V/div] and v_{out} [5V/div] in orange, green and red, respectively.	56
A.1	Structure components.	61
C.1	Simulation results for the impact of the vehicle velocity, 50 km/h with a distance between pads of 500 mm. v_{in} , i_{in} , i_1 , i_2 , i_4 , v_{out} , i_{out} , L_{12} and x , y and z position.	82
C.2	Simulation results for the impact of the vehicle velocity, 85 km/h with a distance between pads of 500 mm. v_{in} , i_{in} , i_1 , i_2 , i_4 , v_{out} , i_{out} , L_{12} and x , y and z position.	83
C.3	Simulation results for the impact of the vehicle velocity, 120 km/h with a distance between pads of 500 mm. v_{in} , i_{in} , i_1 , i_2 , i_4 , v_{out} , i_{out} , L_{12} and x , y and z position.	83
C.4	Simulation results for the impact of the vehicle velocity, 50 km/h with a distance between pads of 1000 mm. v_{in} , i_{in} , i_1 , i_2 , i_4 , v_{out} , i_{out} , L_{12} and x , y and z position.	84
C.5	Simulation results for the impact of the vehicle velocity, 85 km/h with a distance between pads of 1000 mm. v_{in} , i_{in} , i_1 , i_2 , i_4 , v_{out} , i_{out} , L_{12} and x , y and z position.	84
C.6	Simulation results for the impact of the vehicle velocity, 120 km/h with a distance between pads of 1000 mm. v_{in} , i_{in} , i_1 , i_2 , i_4 , v_{out} , i_{out} , L_{12} and x , y and z position.	85

LIST OF FIGURES

C.7 Simulation results for the impact of the vehicle velocity, 50 km/h with a distance between pads of 500 mm. v_{in} , i_{in} , i_1 , i_2 , i_4 , v_{out} , i_{out} , L_{12} and x , y and z position. 86

C.8 Simulation results for the impact of the vehicle velocity, 85 km/h with a distance between pads of 500 mm. v_{in} , i_{in} , i_1 , i_2 , i_4 , v_{out} , i_{out} , L_{12} and x , y and z position. 86

C.9 Simulation results for the impact of the vehicle velocity, 120 km/h with a distance between pads of 500 mm. v_{in} , i_{in} , i_1 , i_2 , i_4 , v_{out} , i_{out} , L_{12} and x , y and z position. 87

C.10 Simulation results for the impact of the vehicle velocity, 50 km/h with a distance between pads of 1000 mm. v_{in} , i_{in} , i_1 , i_2 , i_4 , v_{out} , i_{out} , L_{12} and x , y and z position. 87

C.11 Simulation results for the impact of the vehicle velocity, 85 km/h with a distance between pads of 1000 mm. v_{in} , i_{in} , i_1 , i_2 , i_4 , v_{out} , i_{out} , L_{12} and x , y and z position. 88

C.12 Simulation results for the impact of the vehicle velocity, 120 km/h with a distance between pads of 1000 mm. v_{in} , i_{in} , i_1 , i_2 , i_4 , v_{out} , i_{out} , L_{12} and x , y and z position. 88

C.13 Simulation results for the impact of the source arrangements, each ORMC transmitter pad powered individually. v_{in} , i_{in} , i_1 , i_2 , i_4 , v_{out} , i_{out} , L_{12} and x , y and z position. 89

C.14 Simulation results for the impact of the source arrangements, ORMC transmitter pads powered in parallel. v_{in} , i_{in} , i_1 , i_2 , i_4 , v_{out} , i_{out} , L_{10} and x , y and z position. 90

C.15 Simulation results for the impact of the source arrangements, ORMC transmitter pads powered in series. v_{in} , i_{in} , i_1 , i_2 , i_4 , v_{out} , i_{out} , L_{12} and x , y and z position. 90

D.1 Experimental results for both pads with the same polarity. On the left v_{in} [50V/div], i_{in} [200, A/div] and i_1 [250mV/div] in blue, cyan, and pink respectively. On the right i_4 [500mA/div], v_{Req} [5V/div], v_{out} [2.5V/div] in orange, green, and red respectively. 91

D.2 Experimental results for both pads with the opposite polarity. On the left v_{in} [50V/div], i_{in} [200mA/div] and i_1 [250mV/div] in blue, cyan, and pink respectively. On the right i_4 [500mA/div], v_{Req} [5V/div], v_{out} [2.5V/div] in orange, green, and red respectively. 92

D.3 Illustration of the interaction between two consecutive pads, with currents and magnetic fields denoted. On the left, the pads have the same polarity and on the right the pads have the opposite polarity. 92

D.4 Static results for a load of 2,4 Ω on an aligned situation. a) & c) shows v_{in} [50V/div], i_{in} [200mA/div], i_1 [500mA/div] and i_2 [2A/div] in blue, cyan, pink and green, respectively. b) and d) v_{in} [50V/div], i_4 [500mA/div], v_{out} [1V/div] and i_{out} [250mA/div] in blue, orange, red and yellow, respectively. 93

D.5 Static results for a load of $2,4 \Omega$ on an decoupled situation. *a)* & *c)* shows v_{in} [50V/div], i_{in} [200mA/div], i_1 [500mA/div] and i_2 [2A/div] in blue, cyan, pink and green, respectively. *b)* and *d)* v_{in} [50V/div], i_4 [500mA/div], v_{out} [1V/div] and i_{out} [250mA/div] in blue, orange, red and yellow, respectively. 93

D.6 Static results for a load of $2,4 \Omega$ on an aligned situation. *a)* & *c)* shows v_{in} [50V/div], i_{in} [10A/div], i_1 [10A/div] and i_2 [10A/div] in blue, cyan, pink and green, respectively. *b)* and *d)* v_{in} [50V/div], i_4 [5A/div], v_{out} [10V/div] and i_{out} [2A/div] in blue, orange, red and yellow, respectively. 94

D.7 Static results for a load of $2,4 \Omega$ on an aligned situation. *a)* & *c)* shows v_{in} [50V/div], i_{in} [2A/div], i_1 [1A/div] and i_2 [5A/div] in blue, cyan, pink and green, respectively. *b)* and *d)* v_{in} [50V/div], i_4 [2A/div], v_{out} [5V/div] and i_{out} [1A/div] in blue, orange, red and yellow, respectively. 94

D.8 Static results for a load of $2,4 \Omega$ on an decoupled situation. *a)* & *c)* shows v_{in} [50V/div], i_{in} [2A/div], i_1 [1A/div] and i_2 [5A/div] in blue, cyan, pink and green, respectively. *b)* and *d)* v_{in} [50V/div], i_4 [2A/div], v_{out} [5V/div] and i_{out} [1A/div] in blue, orange, red and yellow, respectively. 95

List of Tables

1.1	Pros and cons of each near-field wireless power transfer.	5
3.1	Comparison of different core arrangements	20
4.1	Experimental setup specifications	26
4.2	Electric parameters for LCL-S-S	33
5.1	Energy transferred depending on the velocity and the distance between pads.	41
6.1	Electric parameters for LCL-S-S	46
6.2	Electric parameters for S-S-S and LCC-S-S	52
A.1	Experimental setup specifications	61
B.1	Table structure example	62
B.2	Coupling with ORMC vs whitout ORMC	62
B.3	Couple between ORMC receiver and IRMC transmitter	63
B.4	Relative position between transmitter and receiver	63
B.5	Magnetic parameters in function of SBT	63
B.6	Magnetic parameters in function of SBT	64
B.7	Magnetic parameters in function of SBT	64
B.8	Magnetic parameters in function of number of turns in each coil	64
B.9	Magnetic parameters in function of number of turns in each coil	64
B.10	Magnetic parameters in function of number of turns in each coil	65
B.11	Magnetic parameters in function of number of turns in each coil	65
B.12	Magnetic parameters in function of the wheel's rotation angle with lateral displacement of 0 mm	66
B.13	Magnetic parameters in function of the wheel's rotation angle with lateral displacement of 50 mm	67
B.14	Magnetic parameters in function of the wheel's rotation angle with lateral displacement of -50 mm	68
B.15	Magnetic parameters in function of the wheel's rotation angle with lateral displacement of 0 mm	69
B.16	Magnetic parameters in function of the wheel's rotation angle with lateral displacement of 50 mm	70
B.17	Magnetic parameters in function of the wheel's rotation angle with lateral displacement of -50 mm	71
B.18	Magnetic parameters in function of the y misalignment with lateral displacement of 0 mm	72
B.19	Magnetic parameters in function of the y misalignment with lateral displacement of 50 mm	73
B.20	Magnetic parameters in function of the y misalignment with lateral displacement of 100 mm	74
B.21	Magnetic parameters in function of the y misalignment with lateral displacement of 150 mm	75

B.22	Magnetic parameters in function of the y misalignment with lateral displacement of 200 mm	76
B.23	Magnetic parameters in function of the y misalignment with lateral displacement of 250 mm	77
B.24	Magnetic parameters in function of the y misalignment with lateral displacement of 300 mm	78
B.25	Magnetic parameters in function of the y misalignment with lateral displacement of 350 mm	79
B.26	Magnetic parameters in function of the y misalignment with lateral displacement of 400 mm	80
B.27	Magnetic parameters in function of the y misalignment with lateral displacement of 450 mm	81

Nomenclature

α	Phase Shift Angle
$^{\circ}$	Degrees
μ	Permeability
Ω	Ohm
ω	Angular Frequency
ω_1	Natural Angular Frequency of the Transmitter Resonant Tank in Two-Coil System and Off-board Resonant Tank in inWIPT System
ω_2	Natural Angular Frequency of the Receiver Resonant Tank in Two-Coil System and Wheel Resonant Tank in inWIPT System
ω_4	Natural Angular Frequency of On-Board Resonant Tank in inWIPT System
Φ	Rate of Change
ϕ	Electromagnetic Flux
π	Pi
θ_s	Entry Angle of the Pad Geometry
A	Ampere
a	Acceleration
B	Magnetic Field
C	Capacitance
C_1	Capacitance of the Transmitter Coil in Two-Coil System and of the ORMC in inWIPT System
C_2	Capacitance of the Receiver Coil in Two-Coil System and of the ORMC in inWIPT System
C_4	Capacitance of the Receiver Coil of the IRMC in inWIPT System
$Coil_l$	Length of ORMC Transmitter or Receiver Coil
$Coil_w$	Width of ORMC Transmitter or Receiver Coil
$Coil_{lintcomb}$	Interior Combination Length of ORMC Transmitter or Receiver coil
$Coil_{lint}$	Interior Length of ORMC Transmitter or Receiver Coil
$Coil_{wint}$	Interior Width of ORMC Transmitter or Receiver Coil
$Core_w$	Core Width
d_{L2}	Length of ORMC Receiver Coil
d_{L3}	Length of IRMC Transmitter Coil
d_{L4}	Length of IRMC Receiver Coil

d_{Lx}	Values of the Diameter
d_{Litz}	Diameter of the Litz Wire
d_{r1i}	Internal Diameter of the Ring of the First Wheel
d_{r1o}	External Diameter of the Ring of the First Wheel
d_{r2i}	Internal Diameter of the Ring of the Second Wheel
d_{r2o}	External Diameter of the Ring of the Second Wheel
d_{Wheel}	Diameter of the Wheel
E	Electric Field
e	Voltage Magnitude
F	Faraday
f	Frequency
f_o	Natural Frequency
f_r	Resonance Frequency
f_s	Switching Frequency
g_{12}	ORMC air gap
g_{34}	IRMC air gap
H	Henry
h	Hour
Hz	Hertz
$i I$	Current
$i_1 I_1$	Current of the off-board ORMC Transmitter Side in inWIPT System
$i_2 I_2$	Current of the Wheel Side in inWIPT System
$i_4 I_4$	Current of the On-Board IRMC Receiver Side in inWIPT System
$i_{in} I_{in}$	Current of the Input Side in inWIPT System
I_{oc}	Open-Circuit Current
$i_{out} I_{out}$	Current at the batteries
I_{sc}	Short-Circuit Current
j	Imaginary Unity
k	Coupling Factor
k_+	Series Coupling Factor Connection
k_-	Anti-Series Coupling Factor Connection
k_{12}	Coupling Factor between the Transmitter and Receiver coils in Two-coil System and of the ORMC in inWIPT System

NOMENCLATURE

k_{34}	Coupling Factor between the Transmitter and Receiver coils of the IRMC in in-WIPT System
km	Kilometre
L	Self-Inductance
l	Coil Length
L_1	Self-Inductance of the Transmitter Coil in Two-Coil System and of the ORMC in inWIPT System
L_2	Self-Inductance of the Receiver Coil in Two-Coil System and of the ORMC in inWIPT System
L_3	Self-Inductance of the Transmitter Coil of the IRMC in inWIPT System
L_4	Self-Inductance of the Receiver Coil of the IRMC in inWIPT System
L_p	Self-Inductance of the Primary Winding
L_s	Self-Inductance at the input coil side
L_s	Self-Inductance of the Secondary Winding
L_T	Total Inductance
L_{12}	Mutual Inductance between the Transmitter and Receiver Coils in Two-Coil systems and of the ORMC in inWIPT System
L_{34}	Mutual Inductance between the Transmitter and Receiver coils of the IRMC in inWIPT System
L_{T+}	Series Inductance Connection
L_{T-}	Anti-Series Inductance Connection
M	Mutual Inductance
m	Metre
M_+	Series Mutual Inductance Connection
M_-	Anti-Series Mutual Inductance Connection
M_x	Misalignment in x axis
mm	Milimetre
N	Number of Turns of a Coil
P	Active Power
P_{oc}	Open-Circuit Power
P_{out}	Output Power
P_{sc}	Short-Circuit Power
$Piece_l$	Length of Piece of the Structure
$Piece_w$	Width of Piece of the Structure

NOMENCLATURE

Q	Reactive Power
Q_f	Quality Factor
Q_{fp}	Quality Factor of Primary Coil
Q_{fs}	Quality Factor of Secondary Coil
R	Resistance
r_1	Resistance of the Transmitter Coil of Two-Coil System and of the ORMC in in-WIPT System
r_2	Resistance of the receiver coil of two and three-coil systems and of the ORMC in inWIPT systems
r_3	Resistance of the IRMC Transmitter Coil in inWIPT System
r_4	Resistance of the IRMC Receiver Coil in inWIPT System
r_s	Resistance of the Input Coil Side
R_{eq}	Equivalent Resistance of the Batteries before Rectifier Action
R_o	Resistance of the Batteries
$Road_l$	Length of Road of the Structure
$Road_w$	Width of Road of the Structure
S	Apparent Power
s	Second
S_{su}	Uncompensated Power
$Slat_l$	Length of Slat of the Structure
$Slat_w$	Width of Slat of the Structure
t	Time
T_l	Length of the Floor Coil Support
T_l	Width of the Floor Coil Support
t_s	Sample Time
$Trailer_l$	Length of the Trailer
$Trailer_w$	Width of the Trailer
$Trailer_{tl}$	Length of the Trailer's Table
$Trailer_{tw}$	Width of the Trailer's Table
V	Volt
v_o	Initial Velocity
v_p	Primary Winding Voltage
V_s	Source Voltage

NOMENCLATURE

v_s	Secondary Winding Voltage
v_{12} V_{12}	Voltage of ORMC Transmitter Coil Linking ORMC Receiver Coil
v_{1rms}	Root Mean Square of the Inverter Voltage
v_{21} V_{21}	Voltage of ORMC Receiver coil Linking ORMC Transmitter Coil
v_{34} V_{34}	Voltage of IRMC Transmitter Coil Linking IRMC Receiver Coil
v_{43} V_{43}	Voltage of ORMC Receiver Coil Linking ORMC Transmitter Coil
V_{DC} V_{dc}	DC Bus Voltage Link
v_{in} V_{in}	Voltage at input side or at the inverter output terminals
V_{oc}	Open-Circuit Voltage
V_{out}	Voltage at the batteries
V_{sc}	Short-Circuit Voltage
$v_{load_{av}}$	Average Load Voltage
VA	Volt-Ampere
x	Lengthwise axis
x_o	Initial Position
y	Horizontal axis
Z	Impedance
z	Vertical axis
Z_1	Impedance of the ORMC Transmitter Resonant Tank in inWIPT System
Z_2	Impedance of the Wheel Resonant tank in inWIPT System
Z_4	Impedance of the IRMC Receiver Resonant Tank in inWIPT System
Z_{in}	Equivalent Impedance of the Input Side
Z_{rIRMC}	Reflected Impedance from the On-board Side onto the Wheel Side in inWIPT System
Z_{rORMC}	Reflected Impedance from the Wheel side onto the Transmitter Side in inWIPT system

NOMENCLATURE

1 Introduction

In the last decade, the Electric Vehicle (EV) market has gained more expression. Historically, the EV was invented before Internal Combustion Engine (ICE) vehicles, with the first EV being invented in 1827 and commercialized in 1839. Initially, the EV was preferred over others types of engines, even with the arrival of ICE vehicles, due to its comfort (lower noise) and easy operation (automatic start-up system).

At the beginning of the 20th century, EVs start to fall behind of ICE vehicle. On that time, the road infrastructure has improved, allowing vehicles to travel further, meaning the autonomy of EVs became too small (around 100 *km* in 1900) to trips between cities, and the lack of electric grid outside the big cities made it difficult to recharge. Later, big deposits of petroleum were found in the United States of America, which made ICE vehicles cheaper to drive. ICE vehicles overcome some issues like the start-up system and the noise produced. Lastly, through the hands of Henry Ford, in 1913 the mass production started, leading to lower prices of ICE vehicles. Some EV manufactures continued to produce some Hybrid EVs, but their prices and performance were not competitive compared to ICE. All those events combined in the dominance of ICE vehicles for 100 years, although EVs remained predominant in some sectors, such as railway [2].

Nowadays, the attention has turned again to EVs for several factors. One of them is the advance of technology, specifically on the storage field, with smaller and lighter batteries like Lithium-ion batteries, Nickel Metal Hydride and Lithium Iron Phosphate [3]; power electronics, with components to work at higher powers; and electric motors. Also, a more extensive and accessible grid and political plans focused on a power transition to electricity, resulting from environmental concerns with the proposal to reduce carbon emissions.

The ICE vehicles are one of the main sources of greenhouse gases (14% of the global emissions) with more than 800 million vehicles in circulation [2]. The viability of EV has an important role in a clean power transition is pending on the electricity generation. If the electricity consumed by the EVs is produced by fossil fuel, carbon emissions will rise, due to efficiency of all processes. But EVs will, in the worst case scenario, shift the transport emissions to outside the urban areas. The emissions produced in the electricity generation can be harvested at the power plants. And, in the best case scenario, all that energy comes from renewable sources, without any emission.

In addition to EVs, fuel-cell and hybrid EVs are also existing alternatives to ICE. Still, EV is currently the most attractive type: their efficiency is the highest, with values around 90% ("thank-to-wheel") [2]; their autonomy is already competitive with ICE, with an average range of around 350 *km*, and the highest being almost 700 *km* [4]; as already mentioned, EVs do not have local emissions; the noise level is very low, being even necessary to add some sound to it for safety reasons; it has regenerative braking, which recovers energy from the inertia of the vehicle movement and stores it in the battery, helping improve their efficiency; their high reliability, due to having fewer fast-wearing parts and moving parts, reducing the maintenance costs; and the "fuel" (Electric energy) transport is safer and cheaper in comparison to fossil fuel, which needs a big fleet, or hydrogen, that needs a big fleet or a pipe network.

All these points are accompanied by the market interest. Since 1990, many car manufacturers tried to reach the market by introducing occasionally new EV models, but just in 2010 the market started to notice their presence. Last year (2022), there was a new record in sales of electric cars (7300000 battery EVs and 2900000 Plug-in Hybrid EVs) Fig. 1.1, with a growth of 56,9%, compared to the previous year [1]. This growth happened despite the slowdown of 3% of the global car market [5]. With that numbers, EVs represented 14% of the sales share. In the near future, the expectation is that the number of EVs continues to grow and by 2030, the stock share of EVs cars will reach 15% (current share: 2.1%) [1]. This trend is not just for cars but for all road vehicles (trucks, motorcycles, buses, etc.).

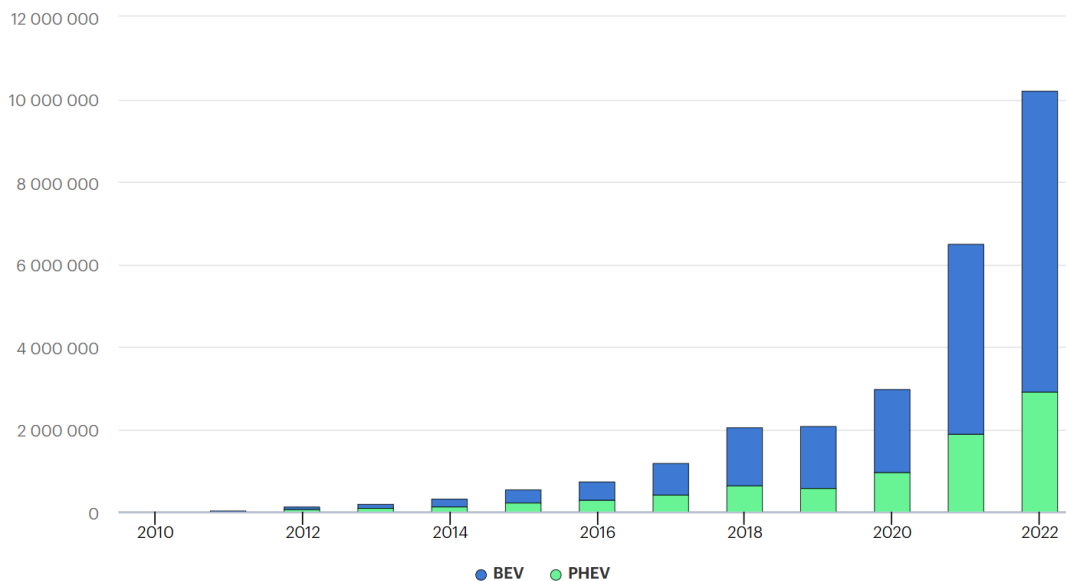


Figure 1.1: EV cars sales, from 2010 to 2022 [1].

Evidence shows that EVs have some demerit points. The main obstacles related to EVs still revolve around the batteries. Despite the autonomy being relatively competitive, this is obtained by using a large number of batteries cells to increase the total capacity. This solution presents some disadvantages, such as increasing the total price of the car (being one of the most expensive components); increasing the weight of the car, that consequently reduces the efficiency; relatively long charge time; and the economic viable deposits of lithium are reduced, and the industry is currently target of humanity and environmental concerns [2]. Another downside is the price, since EVs are more expensive than ICE for the same levels of comfort. Lastly, the current charging infrastructure is small, however, these have been increasing year by year and policy measures stimulate this. For example, the European Union is planning to invest 109 and 149 billion euros in EVs charging infrastructures and in grid and energy implications associated, respectively [6].

EV charging methods can be split into 3 categories: conductive charging, battery swapping and wireless charging [7]. The majority of commercialized EVs use the conductive charging method. This method consists of establish a physical connection between the charging station (grid) and the vehicle. It can use either on-board or off-board chargers and AC or DC source. On-board systems add weight and take up volume in the car,

1.1. WIRELESS CHARGING SYSTEMS

and these problems increase with higher power. For off-board systems, it is necessary to add a communication system, which increases their complexity, but reduces weight and volume in the vehicle, improving their efficiency [8]. Conductive charging is the most efficient, does not require high power on the point of charge, and is easily integrated with Vehicle-to-Grid (V2G). However, the long charging time, the interaction with the user and the stationary nature of the process are some downsides in terms of security and convenience fields. Concepts like range anxiety are already being applied to describe the inconvenience of planning the stops for long trips and the time wasted on the charging process. This problem can be reduced with fast charging technologies or higher capacity of the batteries, but that will decrease the lifetime of the batteries or increase the total weight of the car. Technologies like the pantograph, used for a century on trains, remove those concerns but require high investments and add others drawbacks [2].

Battery swapping works through stations that exchange a discharged battery for a charged one, and then charge the battery that remains with them for the next customer. This method solves some of the conductive charging drawbacks. The swapping time is around two minutes, which is much less than the conductive charging. Another advantage of this method is the possibility of a slower charging process, extending the lifetime of the battery. The downsides are problems related to consumer trust issues regarding the quality and life-time state of the battery delivered. Another drawback is that the number of batteries needed will increase (batteries in cars plus batteries in charging processes), and they are one of the most expensive and environmental worrisome components of the car, as already mentioned.

The wireless charging method is done without any physical connection. It is constituted by a transmitter and a receiver component and as the names suggest the transmitter transmit power to the receiver. Wireless charging can be divided in two categories: static and dynamic charging. Static wireless charging occurs while the vehicle is immobilized. In comparison with conductive charging, this option improves the comfort and safety, because it is not necessary to interact with the charger, offers galvanic isolation, is an automatic process and capable of Vehicle-to-Grid (V2G). Another advantage can be the reduction of visual pollution and space occupied on the side walk by the chargers. On the other hand, dynamic wireless charging occurs while the vehicle is in motion. This option has many advantages, i.e., the non obligation to stop, removing all the questions related with the charging stops and maintaining the comfort and safety of the process. Another advantage is that the total capacity of the batteries can be reduced, since the autonomy does not need to be so high, reducing the total price and weight of the vehicle. These technologies can be applied by many methods, appropriated for different distances between the transmitter and the receiver (air gap), applications and environments. This work is mainly focused on the dynamic wireless charging method, so this topic will be explored in the next section.

1.1 Wireless Charging Systems

The concepts of Wireless Power Transfer (WPT) dates from the late XIX century with the studies of Heinrich Hertz, which demonstrated electromagnetic wave propagation in free space. Nikola Tesla conducted several studies, including the first WPT public demon-

stration [9] and claimed a power transfer across 18 metres. At the time, despite the feat of Nikola Tesla, was achieved with his own invention (Tesla Coil), the high frequencies and voltages result in a big apparatus, making the system potentially dangerous. Throughout his study, he concluded that IPT was a more versatile technology for wireless power applications. Since then, various studies and applications have been developed over the years [10].

First, the technology evolved to telecommunication field. In the 1960s, William C. Brown has used microwaves to power a helicopter model and IPT was used in biomedical applications. In the 1970s, NASA's Jet Propulsion Laboratory transmitted a 30 *kW* DC output with microwaves over 1,5 *km* and researchers focused on higher power IPT to electric highways. Those projects were released in the 1980s, but due to materials available at the time, the projects were considered unsuccessful. In the 1990s, IPT applications started being commercialized, including the first people transport. From the 2000s to the present, with the increasing of movable loads and the popularization of WPT, more applications have become available on the market and defused into our everyday (i.e., the wireless phone charger and the robot vacuum cleaner). In recent years, high power IPT emerged again as an option to charge EVs [2, 9, 10].

WPT systems can be divided into far-field and near-field, depending on the distance range between the transmitter and the receiver. A full diagram of technologies is represented in Fig. 1.2 with the wireless technologies highlighted in grey. The far-field group includes technologies capable of transmit power for over more than a few metres of distance. Examples of technologies from this group are the Radio Frequency Power Transfer (RFPT) and the Optical Power Transfer (OPT), which use radio frequencies and light, respectively, as a means to transfer energy. Radio frequency is already implemented in many devices like radars and microwave ovens. Light is commonly implemented in communications or used in solar panels, in different contexts. Far-field power transfer systems are used in lower power applications, due to its low efficiency (around 10%), potential harmful, and other more specific constrains, such as atmospheric dependencies and only transmit in a straight and unobstructed line for OPT [2]. For charging an EV, large air gaps are not necessary, putting those options out of consideration.

Near-field power transfer systems rely mainly on two groups: the capacitive and the inductive. The Capacitive Power Transfer (CPT) transfers energy between two pairs of electrically coupled metal plates, each pair forming a capacitor capable of transmitting power through variable electrical fields. CPT has many advantages for EV charging applications: can transfer energy through metal; is more robust to lateral displacements, compared to IPT; does not require ferrites; is more compact, lightweight and less expensive; and produces less Electromagnetic Interference (EMI). The biggest downside is to reach high power transfer density for large air gaps, due to the low capacitance between the two plates. In sum, CPT it would require much larger plates than the air gap, not being practical to EV charging [10, 12].

Inductive Power Transfer systems use a variable magnetic field to transfer energy between two coupled coils. Their advantages include the high efficiency (comparable with conductive charger), versatility to different power levels, and tolerance to larger air gaps (enough for EV charging). The main disadvantage is the higher level of EMI, being controllable with shielding. Essentially, given the air gap range and absent of any

1.2. MOTIVATION AND MAIN OBJECTIVES

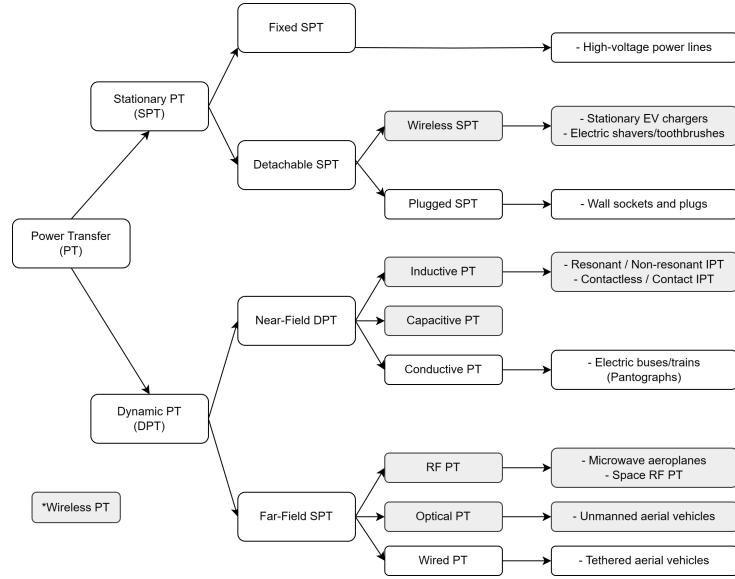


Figure 1.2: Charging topologies diagram. Adapted from [11].

unavoidable disadvantage, IPT is the main choice for EV charging and was the selected technology for this project. The Table. 1.1 present an overview of the two technologies [10].

Table 1.1: Pros and cons of each near-field wireless power transfer [10].

WPT technology	Advantages	Disadvantages
Capacitive Power Transfer	<p>Better misalignment tolerance than IPT system</p> <p>Can transfer power through metallic materials</p> <p>Light and low-cost couplers</p>	<p>Limited power due to low capacitance</p> <p>Very high electric field requirement</p>
Inductive Power Transfer	<p>Higher efficiency</p> <p>Some tolerance to displacements (although the efficiency decreases)</p> <p>Can adapt to power transfer widely ranging from MW level to some W</p>	<p>Small power transfer distance</p> <p>Need for controlling the electromagnetic emissions</p>

1.2 Motivation and Main Objectives

With the above considerations in mind, the main goal of this dissertation is, in a first stage, to study the fundamental of IPT systems and their design in order to understand

the different ways to handling them. After consolidating this knowledge, an onboarding is made to the in-wheel Inductive Power Transfer project, the project where this work fits. The in-wheel Inductive Power Transfer (inWIPT) project is an initiative by the Instituto de Telecomunicações (Coimbra) to develop an IPT technology that addresses both the limited range of an EV and electric hazard risks associated with power cord chargers [13]. Electromagnetic characterization and simulations will then be conducted with the aim of developing a final prototype. This prototype, which is a real-scale prototype, can prove the project concept and evaluate different aspects that are otherwise difficult to test.

The contributions of this dissertation include:

- Electromagnetic evaluation of the impact of different physical characteristics of the Magnetic Coupler (MC).
- Electromagnetic characterization of a in-wheel Inductive Power Transfer system for a Double-D Pad (DDP)-Solenoid Pad (SP) geometries for the Outer Rim Magnetic Coupler (ORMC) and a SP-SP geometries for the Inner Rim Magnetic Coupler (IRMC).
- Matlab[®]/Simulink[®] simulation development to emulate the system on a vehicle in motion on a charging road.
- Prototype development of the in-wheel Inductive Power Transfer (inWIPT) system on a real scale.
- Proof of concept for the dynamic operation of the inWIPT.

1.3 Document Outline

The outline of the document is as follows. Chapter 2 presents the working principles of the Inductive Power Transfer. A review of the main aspects of the Magnetic Coupler is also introduced in this chapter, as well as a review of applications for Inductive Power Transfer systems.

In Chapter 3, it is introduced the inWIPT system, the main proposal and the challenges. An electrical analysis of the resonant topologies is also presented.

In Chapter 4, a study of the electromagnetic characterization is conducted to understand some building aspects and possible optimizations. A part of the prototype is also presented in this chapter.

In Chapter 5, a look into the simulation model of an EV charging in motion is taken. The most important components are described and results are presented in order to develop the final prototype.

In Chapter 6, the rest of the prototype is explained, and power tests are conducted to prove the project concept, validate the simulation, and draw some early conclusions.

Finally, the last chapter summarizes the work of this dissertation and present some conclusions. The last chapter also provides suggestions for future research directions.

2 Inductive Power Transfer

A typical IPT can be divided into two sides, the transmitter and receiver, as shown in Fig. 2.1. The transmitter side is composed by the grid, which supplies the needed power; the rectifier, which converts AC to DC (optional, depending on the source), followed by a capacitor to generate a DC bus; the inverter, which converts DC to AC and establishes the system frequency; the resonant configuration, which improves the capability of power transfer between coils; and the transmitter coil also designated as the transmitter pad. The receiver side is composed by the receiver coil (receiver pad), which together with the transmitter pad forms the magnetic coupler, the main component of the system; a resonant compensation; an on-board power converter, which converts AC to DC to a level appropriate to the load; and the load, which can be a motor or a battery, either using or storing the transferred energy.

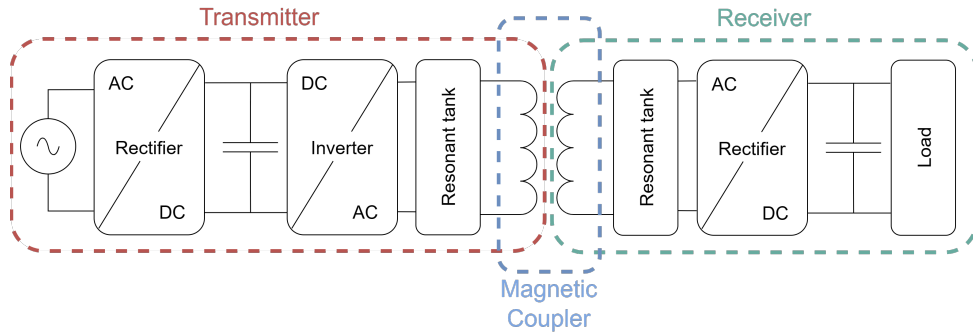


Figure 2.1: Typical structure of a IPT system.

Throughout this chapter, the working principle and some of the most critical components of the IPT system will be detailed.

2.1 Working Principles

The IPT is mainly explained by Ampere's and Faraday's laws, both related to Maxwell equations. Ampere's law or the fourth Maxwell equation, relates the current (I) passing through a closed loop wire and the magnetic field (B) around the loop, equation 2.1. These two quantities are proportional, with a constant of proportionality equal to the permeability of free space (μ_o), as is shown in equation 2.2. By Faraday's law, a variation in the magnetic field (B) induces an electric field (E) in the opposite direction (see equation 2.3). The magnitude of this electric field will be translated to a voltage when it passes through a wire loop. The magnitude of that voltage (e) will be proportional to the rate of change of the magnetic field (Φ), and the number of turns of the loop (N), as described in equation 2.4 [14].

$$\nabla * H = J \quad (2.1)$$

$$\oint B.ds = \mu_o.I \quad (2.2)$$

2. INDUCTIVE POWER TRANSFER

$$\nabla * E = -j.\omega.B \quad (2.3)$$

$$e = -N.\frac{d\Phi(\vec{B})}{dt} \quad (2.4)$$

Combining these two laws, an AC on the transmitter coil (Tx) will generate a variable magnetic field. Some lines of that magnetic field will reach the receiver coil (Rx) and induce a voltage on their terminals, other lines do not reach the receiver coil and will close around the same coil (transmitter coil), called leakage flux. If the receiver coil has a load, a current will flow. So, in the same way, the new current present in the receiver will generate a magnetic field and induce a voltage on the terminals of the transmitter coil. Leakage flux will be generated by that current too. Figure 2.2 shows the magnetic fluxes between the two coils, the transmitter magnetic field is represented in blue, and the receiver magnetic field in red. ϕ_{xy} represent the flux and the x is where are from and the y is where the flux reaches. N_p and N_s is the number of turns of the transmitter and receiver coil, respectively.

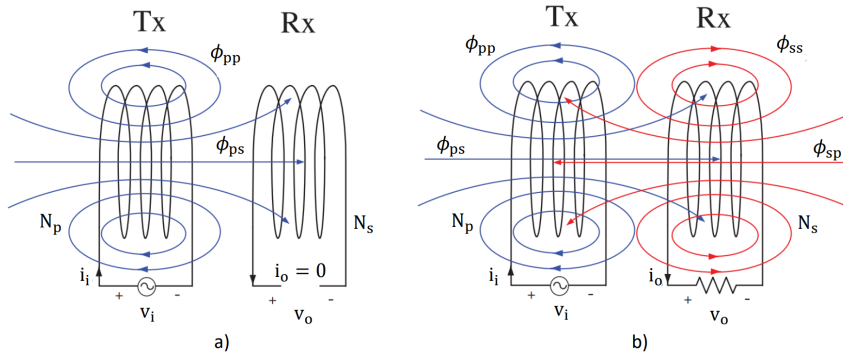


Figure 2.2: Magnetic fluxes of two inductors in the instantaneous time domain, adapted from [2].

The value of the induced voltage depends on angular frequency (ω) and the RMS value of the current (I_p), and can be obtained with the equations 2.5 and 2.6, where the subscript p and s is referred to the primary and secondary side, respectively. M is the mutual inductance between the primary and secondary coils, quantifies the magnetic coupling between the transmitter and the receiver and is dependent of physical parameter, such as the air gap (distance between the two coils), the number of turns in each coil, the lateral displacement, the dimensions, along others. Equation 2.7 relates mutual inductance (M) with the self inductance (L_p and L_s) and the coupling factor (k). k varies between 0 and 1, where 0 is no coupling and 1 is full coupling between the coils. Figure 2.3 shows the electric equivalent model of the coupling between the two coils.

$$v_p = j.\omega.Mi_s \quad (2.5)$$

$$v_s = j.\omega.Mi_p \quad (2.6)$$

$$M = k.\sqrt{L_p.L_s} \quad (2.7)$$

2.2. MAGNETIC COUPLER STRUCTURE

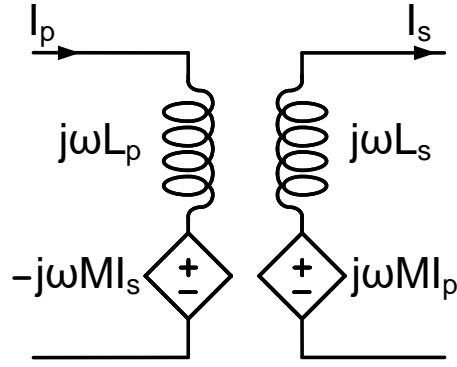


Figure 2.3: Electric equivalent model of the coupling between two coils.

2.2 Magnetic Coupler Structure

The magnetic coupler structure is composed by the transmitter and receiver pads with a certain distance between them (air gap). In turn, pads are composed by a combination of different characteristics, such as the number of turns, the geometry, the volume and shape of ferrite cores, among others. Summarizing, pads are composed by the coil, the ferrite core and the shield, as show in Fig. 2.4. For EV applications, the transmitter is buried in asphalt, and the receiver integrated in the car, usually in the car chassis. Additionally, for a dynamic case, the transmitter pad can be placed on the road as a long pad or a segmented pad. All those factors will impact on M and, consequently, on k , establishing the power transfer capability. A brief overview of some of these aspects/components will be presented in this section.

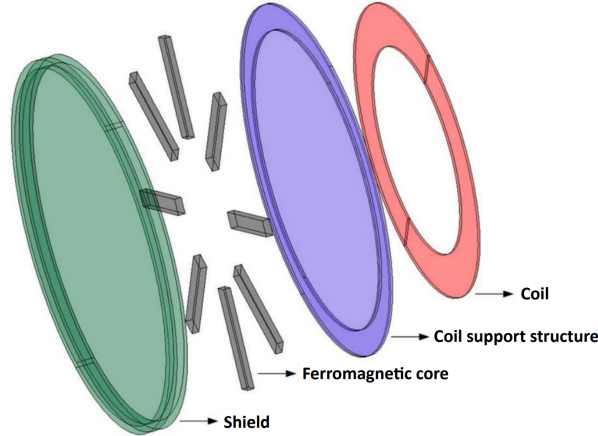


Figure 2.4: Generic pad constitution [15].

2.2.1 Long or Segmented Pads

For dynamic charging, the transmitter pad can be long where the transmitter is much larger than the receiver; or segmented, where the transmitter and receiver have a relation close to 1:1. However, in this second scenario, more transmitter pads will be used. The placement of both topologies along a stretch of road is represented in Fig. 2.5, with the

transmitter represented in red colour. The long pads were the first to be studied. The fact that the receiver is much smaller than the transmitter leads to a lower coupling factor k and a larger leakage inductances. Other downsides include higher power losses, due to increased resistance, and the possibility of having many receivers on the same transmitter pad, resulting in higher EMI. Additionally, the amount of cable required would be superior for long pads for the same covered area, which increases the total cost. For these reasons, researchers made efforts to apply segmented pads on their projects [2, 16].

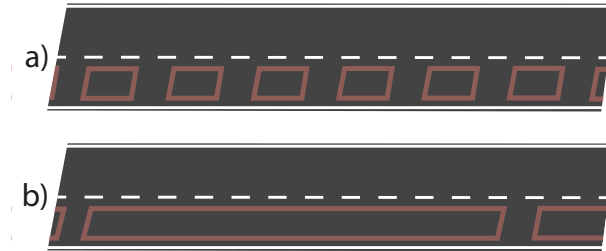


Figure 2.5: Placement of transmitter pads on the road. a) Segmented pad; b) Long pad [17].

The segmented pads, which were later applied to static charging, increase the coupling factor k and the mutual inductance M compared to long pads, resulting in better efficiency. Another advantage is easier replacement or repair. However, the control and design optimization (ideal distance between pads) increase the complexity. Moreover, the lower cost, the compactness and the robustness are necessary, as constant mechanic stress and extreme temperatures can be applied to the road, while still being easy to install and maintain [18].

2.2.2 Pad Geometries

The main parameters in the geometry design are the coupling factor, interoperability and misalignment tolerance [19]. For higher coupling factors, it is important to have the largest possible coil, which is restricted by the car. The space limitation led researchers to develop different pad geometries.

Depending on the physical placement of the pad, the flux orientation is determined as either perpendicular or parallel to the pad surface. Pad geometries can be divided into three groups: non-polarized, polarized and omni-directional. Non-polarized pads can generate and couple a parallel or a perpendicular flux component, and are only composed by one coil. Polarized pads can generate and couple both parallel and perpendicular flux components, and are composed by more than one coil. Finally, omni-directional pads can generate and couple fluxes from all directions [20].

The first pad geometry proposed was a non-polarized topology, with circular shape. For that reason, it was denominated as Circular Pad (CP). The great advantage of CP is its independence from crossing angles, being compact and low weight. On the other side, the power transfer is limited, and it has low misalignment tolerance and high leakage magnetic fields. Another common non-polarized topology is the Rectangular Pad (RP) with a rectangular shape. The proposal was to maximize the occupied available space,

2.3. RESONANT TOPOLOGY

but the behaviour is very similar to the CP. The biggest difference is around the lateral displacement. In CP the coupling profile is indifferent to the direction is the displacement, whereas in RP the coupling profiles have different shapes.

The polarized geometries, because they are constituted by two or more coils, can be connected in various ways, being able to produce and couple both flux pattern. The Solenoid Pad (SP) is mostly used in EV applications and is shaped to look similar to a cylinder. SP can reach higher coupling factors for larger air gaps and lateral displacements. The main issue lies in the generation of double-sided flux, which reduces the quality factor. To overcome this issue, the Double-D Pad (DDP) was developed, placing two RP side by side. This geometry combines some advantages of CP and SP, resulting in reduced total volume and weight while maintaining a single side flux, similar to CP. Additionally, it offers better coupling factors and a larger charging area. However, the coupling pattern varies depending on the entry axis, with null points where the transferred power is zero.

Other geometries have been studied and documented, but a selection of the most important ones was made for the present work.

2.2.3 Ferromagnetic Core and Shielding

The ferromagnetic core or ferrite can be placed beneath the coil for the transmitter pad and/or above the receiver pad. They help increase the mutual inductance M and coupling factor k , which are low due to the significant magnetic reluctance of the large air gap and misalignment. The ferrite cores have high permeability, allowing magnetic fluxes to pass through easily and reducing the flux dispersion. Other requirements include the high resistivity and low hysteresis loss, necessary for handling high switching frequencies and the levels of power transferred [15]. These type of cores are named by a letter depending on their appearance (for example: I, U, E). The geometry pads can be classified as single-sided, if the coil is only on top of the ferrite, or double-sided, if the coil is wound to the ferrite.

The double-sided topologies have leakage flux at the back of the pad. An aluminium sheet (shield) can be placed behind the pad, reducing EMI (shielding) and improving the coupling factor. On the other side, double-sided topologies ideally require only half of the amount of ferrite core than single-sided [21].

Ferrites are an expensive and fragile material, accounting for more than half of the total cost of the pad, and are easily susceptible to maintenance. Therefore, due to their high cost and the vulnerability to mechanical stress imposed by the cars, alternative ferrite-less pad topologies have been investigated [22].

2.3 Resonant Topology

The IPT system operates similarly to a transformer, with the main difference being the larger leakage inductance on both sides due to a large air gap and magnetic uncoupled inductors, resulting in a lower core permeability [2]. These leakage inductance decrease the energy power capability, increasing the reactive power. To reduce leakage inductances, a resonant compensation is placed on the pads terminals (the resonant compensation is

composed at least by a capacitor) to reduce the reactive component of leakage inductance. This approach is the same one used over the years to correct the power factor and to compensate transmission lines.

If a resonant compensation works at resonance point, where the filter natural frequency (f_0) is equal to the inverter switching frequency (f_s), the reactive component of leakage inductance is nullified. At resonance $\omega_0 = \omega^1$, the maximum power transfer capability is achieved, leading to higher overall efficiency.

The simplest resonant compensation types are the series (S) and parallel (P), where a capacitor is placed in the series or parallel with the receiver and/or transmitter coil, respectively. Additionally, more complex arrangements called hybrids can be used, including additional capacitors and/or coils in basic configurations. Among the most common are LCL, where a coil is placed before the parallel resonant compensation and LCC, where a capacitor is placed in series with the pad coil of the LCL configuration. These configurations can be arranged in any possible combination, resulting in different resonant topologies. These topologies are named based on the resonant compensation applied. Each name is composed by two acronyms of the resonant topology separated by a hyphen. The first acronym refers to the resonant compensator of the transmitter pad, and the second refers to the resonant compensator of the receiver pad. For example, an S-P resonant topology is composed by a series compensator on the transmitter pad and a parallel resonant compensation on the receiver pad. Figure 2.6 illustrates different possible compensations with the electric circuit presented.

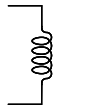
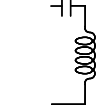
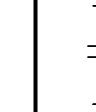
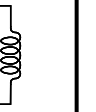
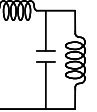
Resonant compensation	No compensation	Series compensation	Parallel compensation	LCL compensation	LCC compensation
Electrical circuit					

Figure 2.6: Different resonant compensations.

The selection of topology will impact the system behaviour. Therefore, it should be considered during the design process for the specific application. Some aspects that can improve and serve as a means of comparison between topologies include:

- The maximum frequency
- The maximum load power transfer
- Load-independent output voltage or output current
- k-independent compensation
- Allowance of no magnetic coupling ($k = 0$) [2]

¹ $\omega_0 = 2\pi \cdot f_0$; $\omega = 2\pi \cdot f_s$

2.4 Quality Factor

The quality factor (Q_f) represents the relation between the reactive and active power, as show in equation 2.8. It compares the energy stored in the resonant tank to the energy dissipated on the same, so it is based on the compensation level of the system. A higher Q_f leads to increased energy transfer capability, presenting a more efficient system due to a lower reactive power. One approach to improve Q_f is by increasing the section of the coil cable and the volume of the ferrites. However, due to space constraints in vehicles and the need for narrow bandwidth to future tuning, this is not the best solution. Another reliable approach is to the increase k .

$$Q_f = \frac{Q}{P} \quad (2.8)$$

For each resonant tank, there will be a Q_f . So, for magnetic couplers with two resonant tanks, two Q_f will exist: one for the primary side and the other for the secondary side (Q_{fp} and Q_{fs} , respectively). The relation between them is important for the system stability, and for that reason, Q_{fp} should be much higher than Q_{fs} .

The MC and the working principles of an IPT are similar to a transformer with a loose coupling between the transmitter and the receiver, as already mentioned. The open-circuit and short-circuit tests can be used to determine an approximated value of the self and mutual inductance and the power transfer capability of a MC. In the open-circuit test, the receiver coil is open-circuited, and the transmitter is connected to a full rated line voltage (V_1). The input current (I_1), input voltage (V_1) and input power (P_{oc}) are measured under those conditions. In the short-circuit test, the receiver coil is short-circuited, and it is supplied with the nominal current (I_1) to the transmitter coil. Therefore, the input current (I_1), input voltage (V_1) and input power (P_{sc}) are measured [23].

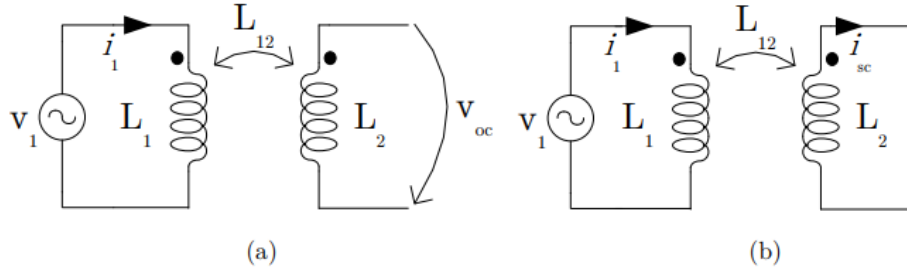


Figure 2.7: Schematics of: a) Open-circuit test; b) Short-circuit test.

$$\bar{V}_{oc} = j.\omega.M.\bar{I}_1 \quad (2.9)$$

$$\bar{I}_{sc} = \frac{\bar{V}_1}{j.\omega.L_2} = \frac{M.\bar{I}_1}{L_2} \quad (2.10)$$

The uncompensated power (S_{su}) of a magnetic coupler quantifies the power transfer capability of the structure, and it is the product of open-circuit voltage (V_{oc}) with the short-circuit current (I_{sc}), equation 2.11 [16].

2. INDUCTIVE POWER TRANSFER

$$S_{su} = \bar{V}_{oc} \cdot \bar{I}_{sc} = j \cdot \omega \cdot I_1^2 \cdot \frac{M^2}{L_2} \quad (2.11)$$

The output power (P_{out}) is obtained by multiplying the uncompensated power by the load quality factor, as shown in equation 2.12. This represents the amount of power that can be transferred from the transmitter to the receiver [16].

$$P_{out} = S_{su} \cdot Q_f = |\bar{V}_{oc}| \cdot |\bar{I}_{sc}| \cdot Q_f = \omega \cdot k^2 \cdot L_1 \cdot |\bar{I}_1|^2 \cdot Q. \quad (2.12)$$

3 Double Coupling IPT System

The system studied in this work was first mentioned in [24] and named in-wheel Inductive Power Transfer (inWIPT) system by the authors. The inWIPT is a system capable of static and dynamic charging, introducing the proposal to reduce the air gap on EV IPT charging applications by placing the receiver pad on the wheels, instead of the conventional approach of placing it on the vehicle chassis. The traditional pad placement is represented in Fig. 3.1 a), while the proposed system pad placement is shown in Fig. 3.1 b). This change allows an air gap reduction from values between 100 *mm* and 350 *mm* to 30 *mm* and 60 *mm*. Due to the new receiver position, the air gap obtains an independence from the type of vehicle (car, SUV, truck, bus, etc.), as the variation between tyre thickness is very small compared to chassis height.

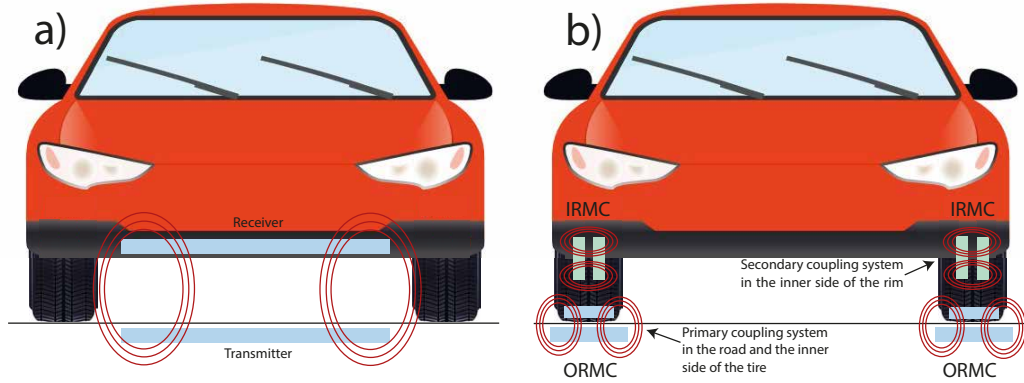


Figure 3.1: Coil placement: a) Traditional; b) in-wheel. Adapted from [24].

This project was based on [25], where the authors proposed the use of a MC with the transmitter pads embedded on the ground and receiver pads embedded in the vehicle rubber tyres. Therefore, for the power transfer between the wheel and the axle, slip rings were used via DC, similar to electric motors. However, the concept reduces its mechanical efficiency due to higher friction losses and the reliability, increasing the need of maintenance. Moreover, the placement of power converters inside the tire makes them more susceptible to mechanical impacts. To address this issue, the inWIPT system uses a second MC in the place of the slip ring to transfer power between the wheel and the car axle without any physical contact. This completely eliminates electrical system problems associated with mechanical parts. With this proposal, power converters inside the tyre are no longer necessary. The double coupling configuration consists of two MCs systems. The system belongs to the group of multiple coupling IPT systems due to the placement of two MCs structures in series. This increases the complexity of the system from the analysis to the design.

The proposed system reduces the impact of the air gap and increases the coupling factor compared to traditional EV IPT applications. The smaller air gap enables new pad design opportunities to mitigate the impact of lateral displacements and increase the charging area. The coupling factor remains low, therefore frequencies around 85 kHz and resonant tanks are used to increase the power transfer capability.

The reduced dimensions of the presented system, compared to traditional ones, result in a loss of power transfer capacity. However, unlike the traditional EV application, where only one IPT system is used, this approach can be applied for each wheel of the vehicle, compensating for the size reduction.

Moreover, such approach follows the trend line of moving the powertrain from the vehicle into the wheels. The development of new airless tyre designs, such as the Uptis model from Michelin, which utilizes non-magnetic materials, strengthens the applicability of inWIPT. These new airless tyre designs also eliminate the risk of pressure increase inside the tyre due to heating caused by the Joule losses in the receiver coils placed within the tyre. In addition, the aluminium rim shields the leakage flux lines above the receiver coils and eliminates the need for additional shielding material.

This chapter will provide a brief overview of multiple coupling IPT systems. Moreover, a more detailed analysis of the inWIPT system, the interaction between the coils (ORMC and IRMC), the structural aspects and a resonant topology will be analysed.

3.1 Multiple coupling IPT systems

Multiple coupling IPT systems are systems that contain more than one MC between the source and the load. Various studies have proposed multiple coupling systems for different applications. Some present "parallel" MC acting like intermediary coil, magnetically linked with receiver and transmitter, as represented in Fig. 3.2 a). Others introduce multiple MC in series between the source and the load, Fig. 3.2 b), which is the type of the system under study.

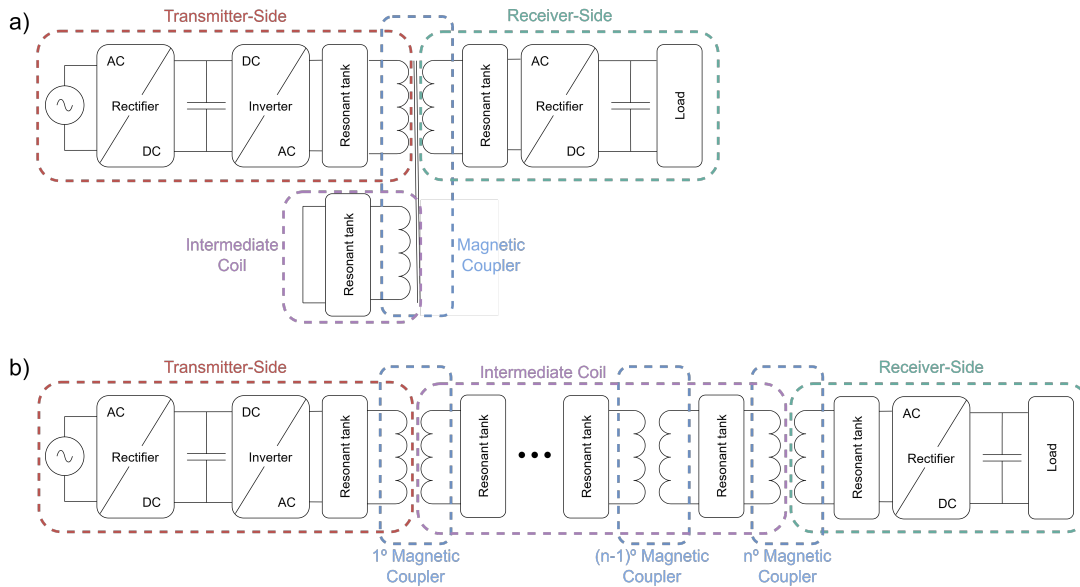


Figure 3.2: Placement of an intermediate coupler in conventional IPT systems. a) in parallel [26], and b) in series [27].

Multiple coupling IPT systems are commonly used today. They offer several advantages, including enhanced magnetic link, boosted power transfer capability and the ability

3.2. ORMC AND IRMC

to limit capability (depending on the resonant tanks) for no coupling mode (critical for dynamic IPT). The decision to use a multiple MC with multi-coils for this application was primarily driven by physical reasons, taking into account the placement of the pads and the different movements applied to them.

Several studies have compared two-coils systems with three-coils or more systems. In reference [26], the author demonstrates that a symmetric structure is necessary for higher efficiencies. Additionally, for higher air gaps, the three-coil system achieves higher efficiencies. Both systems have low robustness to load variations. In reference [28], the proposed system with four-coils all linked between each others claims to achieve higher power transfer with lower EMI, especially for higher air gaps. In reference [27], an electrical system similar to the inWIPT system with two MC in series is presented. The system has the transmitter side and the intermediate coil buried on the roadway and the receiver under the chassis of the car. As an AC-AC controller, the intermediate coil controls the current of the third coil, and communication between the transmitter and the receiver is required. Experimentally, a real scale model system achieved a transfer of 500W for two different air gaps in a static charge.

The resonant topology notation used for multiple coupling IPT systems is similar to traditional IPT systems. The process involves adding the letters corresponding to each resonant tank used, in order from the source to the load, separated by a hyphen.

3.2 ORMC and IRMC

The overall system composition of the inWIPT is similar to a typical IPT system (Fig. 2.1). As show on Fig. 3.3, the off-board and on-board sides remain the same composition as the transmitter and receiver sides of a typical IPT, respectively. Between them, a new part called wheel side is added. The first MC transfers power from the off-board to the wheel side, and it is referred to as the Outer Rim Magnetic Coupler (ORMC). The second MC transfers power from the wheel side to the on-board side and is referred to as Inner Rim Magnetic Coupler (IRMC). Therefore, the wheel side is composed by the receiver coil of the ORMC, the transmitter coil of the IRMC and a resonant tank between them, compensating for both coils. The receiver side of the ORMC and the transmitter side of IRMC are electrically connected and share the same resonant tank. In this work, a convention will be adopted in which the components related to the transmitter side of the ORMC will have the subscript 1. The receiver side of the ORMC with subscript 2. The transmitter side of IRMC with subscript 3. And the receiver side of the IRMC will have a subscript 4. For quantities referred to more than one side, such as the mutual inductance of the ORMC, two subscripts will be used, in this case 1 and 2.

For ORMC, the transmitter (off-board side) is placed along the road or in a static charging station, and the receiver (wheel side) is placed between the inner side of the tyre surface and the outer side of the rim. For the IRMC, the transmitter (wheel side) is placed on the inner side of the rim, and the receiver (on-board side) is fixed together with the breaking system in the wheel hub. Traditional pad geometries can be applied to the inWIPT system. However, due to the shape of the wheels, the receiver coil of the ORMC and the coils of IRMC will assume a cylindrical design, changing the coupling profiles of

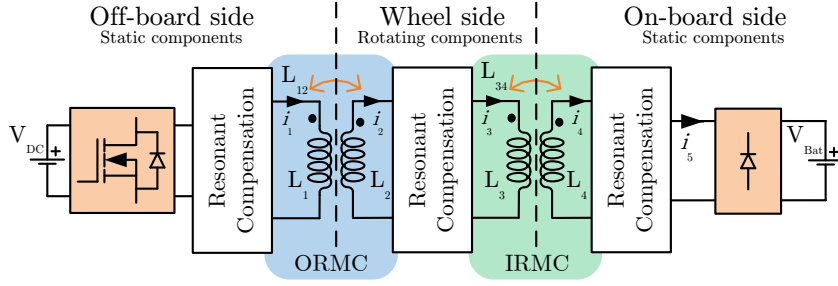


Figure 3.3: Schematic diagram of inWIPT system [29].

traditional IPT geometry pads. The placement of the coils around the rim depends on the main flux path orientation of the transmitter pad and must ensure a 360° coverage. In addition, the ferromagnetic material must be placed in the outer rim surface to mitigate the shield effect caused by the aluminium of the rim. Figure 3.4 shows the physical placement of the coils on the wheel. The impact of the new degree of freedom given by the wheel rotation will depend on the pad geometry.

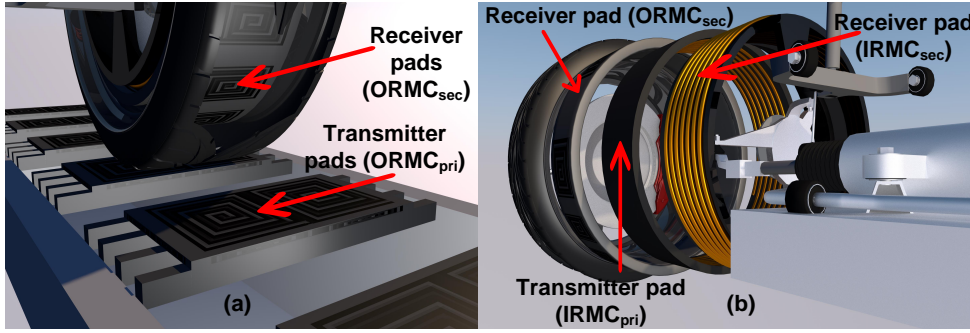


Figure 3.4: Structure of inWIPT system [30].

The coupling factor of ORMC remains dependent on the position of the vehicle and the applied geometries. Due to coils positions, the coupling factor of the IRMC ensures, in normal operation, a constant air gap regardless of the charging positions.

3.3 Magnetic Couplers Configurations

In this work, it will be adopted and analysed the following geometries pads: for the ORMC, the transmitter will be a DDP, and the receiver will be a SP (DDP-SP); for the IRMC, both coils will have a SP geometry (SP-SP). Figure 3.5 represents the placement of the pads configuration. As mentioned in Section 2.2.2, the two used geometries belong to the polarized group. In addition, DDP geometry also classified as single sided, meanwhile the SP is classified as double-sided. Due to polarization characteristics of the coil geometry, it is necessary to place the ORMC DDP transmitter in a way that the magnetic flux have a parallel orientation relative to the magnetic flux of the ORMC SP receiver. If the transmitter pad is rotated by 90° , a null coupling factor will be observed between the transmitter and receiver of the ORMC, resulting in no power transfer. In Fig. 3.5, the orientations for both configurations are shown. The transmitter DDP is rep-

3.3. MAGNETIC COUPLERS CONFIGURATIONS

resented in red and green colour and the receiver pad is represented by orange colour for SP topologies. The wheel rim is represented in light grey, while the dark grey represents the ferromagnetic cores.

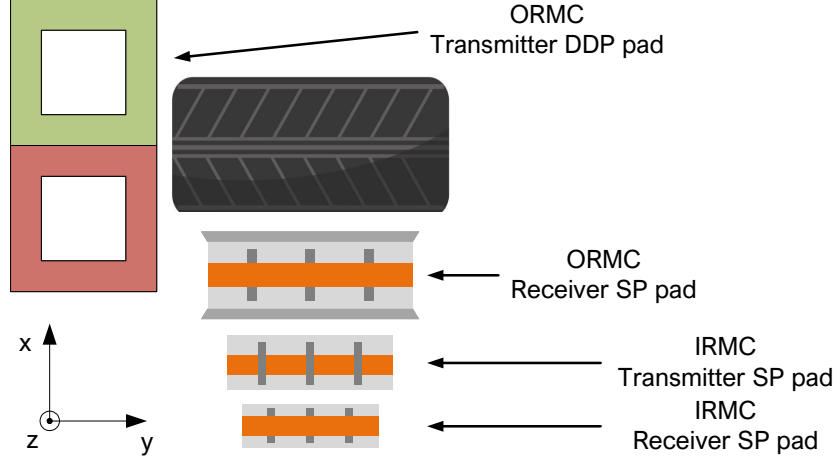


Figure 3.5: ORMC and IRMC placement on the wheel and roadway for the inWIPT system. DDP-SP and SP-SP.

The DDP is the selected geometry to the transmitter pad of ORMC due to better tolerance to lateral displacement (along y-axis) compared to non-polarized geometries, and a larger charging area. The DDP geometry adopted will be ferrite-less, due to constant mechanical impacts inherent to the nature of transmitter pads. Nevertheless, the DDP has two distinct coupling patterns with null points for some geometries.

The ORMC receiver will be placed around the rim. The simplest geometry solution is the SP, which is wound around the rim. The cylindrical design together with the rotary movement of the wheels adds complexity to the mutual coupling analysis since it creates a new movement between the transmitter and receiver pads of the ORMC. The selected geometry for the receiver of ORMC was based on the admissible combinations between geometries, followed by ensuring homogeneity of the geometry around all the rim, and lastly considering building complexity.

The choice of the SP geometries for both pads of IRMC has been made with the goal to achieve a constant coupling pattern for all situations. The aim is to maintain the coupling factor independent of the relative position between the coils. Therefore, the complexity of the entire system will be decreased, compared to variable coupling patterns.

In terms of ferromagnetic cores for the ORMC receiver pad and both IRMC pads, a previous study whit in the inWIPT project, utilized Finite Element Analysis (FEA) tool. Table. 3.1 presents three IRMC designs, labelled Type I to Type III, each with a different core layout. The first two types have segmented cores with 12 and 18 ferrite bars in each side while Type III has two cylindrical ferromagnetic cores. All designs exhibit k_{34} above 0.72 for an air gap of 15 mm and a maximum coupling of 0.785 is achieved using Type III core arrangement. In terms of S_{su} , all designs demonstrate power transfer capabilities above 13 kVA when driven by a constant current in the transmitter pad of 20 A_{rms} . Additionally, Type III has a S_{su} that exceeds Type I by a factor larger than 1.7, under the same working conditions. This difference is a consequence of the

larger increase in the self-inductance values of both the transmitter and receiver coils caused by the additional ferrite. However, the ratio of ferrite versus S_{su} is higher in Type I configuration. This means that a segmented ferromagnetic core makes better use of the ferrite than a full ferromagnetic core [31]. Therefore, the geometries adopted will incorporate some ferromagnetic core, but not throughout their entire extension. Further analyses related to this topic will be implemented in the final prototype, as discussed in the next chapter.

Table 3.1: Comparison of different core arrangements [31].

	Type I	Type II	Type III
k_{34}	0.724	0.752	0.785
P_{su} [kVA]	13.710	17.017	23.523
Ferrite [cm ³]	456	684	1322
Use [VA/cm ³]	30.07	24.88	17.79

3.4 Analysis of LCL-S-S Topology

The First Harmonic Approximation (FHA) is employed for the mathematical analysis. This involves using a sinusoidal source, characterized by its fundamental component (\bar{V}_{in}). The sinusoidal source replaces the full-wave inverter, simplifying the analysis process. The input voltage of the inverter at the fundamental harmonic ($|\bar{V}_{in}|$), can be expressed as a function of the phase shift control angle (α), where V_{DC} represents the average DC link voltage, as described in equation 3.1.

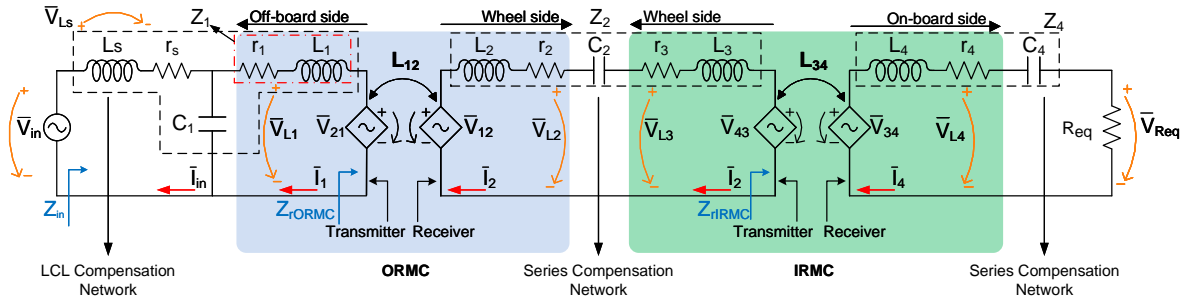


Figure 3.6: Equivalent circuit model for double coupling in WIPT for LCL-S-S topology.

$$|\bar{V}_{in}| = V_{DC} \frac{2\sqrt{2}}{\pi} \cos\left(\frac{\alpha}{2}\right), \quad (3.1)$$

The equivalent electrical circuit, based on the dependent voltage sources and circuit impedances, is used in order to replace the two MC. All compensation network circuits

3.4. ANALYSIS OF LCL-S-S TOPOLOGY

are designed to operate at the resonance point, where the imaginary part of the input impedance Z_{in} equals zero. This ensures that way the load behaves linearly from the input perspective. I_1 , I_2 , I_3 and I_4 have sinusoidal waveforms when operating under resonance, although the converter is fed by a square wave voltage. This indicates that power transfer to the equivalent load is realized by the fundamental component of the input voltage V_{in} , thus FHA is usually used in the design process.

Figure 3.6 illustrates the LCL-S-S circuit model that was suggested as the initial approach to assess the inWIPT for dynamic operation. Beyond the subscripts that have already been mentioned, an additional subscript (s) is used. It represents the components related with the inductor to form the LCL-S-S resonant tank. The r_s represents the equivalent resistance of the input series inductor L_s . The other equivalent resistance of each inductor are also represented by r_1 , r_2 , r_3 and r_4 , and include Joule and iron losses (if applicable).

These circuits incorporate resonant tanks in various meshes, containing distinct angular resonant frequencies, ω_1 , ω_2 , and ω_4 . These resonant tanks are composed by elementary electronic components (R , L and C), that together represent equivalent impedances of the resonant tanks on the off-board, wheel, and on board sides (Z_1 , Z_2 , and Z_4 , respectively). Moreover, the concept of reflected impedance in IPT systems refers to the equivalent impedance of one side seen at the terminals of the pad in the other side. Figure 3.6, illustrates the proposed circuit, containing two reflected impedance values (Z_{rORMC} and Z_{rIRMC}). The Z_{in} is the impedance seen at the input signal of the electric circuit.

For the output of these circuits, an equivalent resistance R_{eq} is used. The R_{eq} is the equivalent resistance of the batteries R_{bat} before the rectifier, and the relation between them is given by the equation 3.2.

$$R_{eq} = \frac{8 \cdot R_{bat}}{\pi^2} = \frac{8 \cdot V_{bat}}{\pi^2 \cdot I_{bat}}, \quad (3.2)$$

Usually, for static IPT applications, the inverter PHS angle is adjusted in order to control the power delivered to the load [19]. However, considering dynamic IPT operation, the inherent EV movement will lead to fast changes in the system coupling. Therefore, a fast controller will be need to control the inverter operation. To simplify the voltage control and take advantage of the LCL's current source characteristic at L_1 , $|I_1|$ remains constant for the same V_{in} , regardless of the load and coupling variations. Therefore, V_{in} remains constant throughout the process. For a constant input voltage V_{in} (load and coupling independent), the input voltage will be set at a fixed PHS.

3.4.1 Circuit Analysis

Applying the Kirchoff's laws to the circuit (Fig. 3.6), the following equations are obtained:

$$\bar{V}_{in} = r_s \cdot \bar{I}_{in} + j \cdot \omega \cdot ((L_s - 1/(\omega^2 \cdot C_1)) \bar{I}_{in} + 1/(\omega^2 \cdot C_1) \bar{I}_1), \quad (3.3)$$

$$0 = r_1 \cdot \bar{I}_1 + j \cdot \omega \cdot (1/(\omega^2 \cdot C_1) \bar{I}_{in} + (L_1 - 1/(\omega^2 \cdot C_1)) \bar{I}_1 - L_{12} \cdot \bar{I}_2), \quad (3.4)$$

$$0 = (r_2 + r_3) \cdot \bar{I}_2 + j \cdot \omega \cdot ((L_2 + L_3 - 1/(\omega^2 \cdot C_2)) \bar{I}_2 - L_{12} \cdot \bar{I}_1 - L_{34} \cdot \bar{I}_4), \quad (3.5)$$

3. DOUBLE COUPLING IPT SYSTEM

$$0 = (R_{eq} + r_4) \cdot \bar{I}_4 + j \cdot \omega \cdot (L_4 - 1/(\omega^2 \cdot C_4)) \bar{I}_4 - L_{34} \cdot \bar{I}_2, \quad (3.6)$$

The capacitors [32] values are given by

$$C_1 = 1/(\omega_1^2 \cdot L_1) = 1/(\omega_1^2 \cdot L_s), \quad (3.7)$$

$$C_2 = 1/(\omega_2^2 \cdot (L_2 + L_3)), \quad (3.8)$$

$$C_4 = 1/(\omega_4^2 \cdot L_4), \quad (3.9)$$

Solving (3.3) to (3.6) provides the current equations that accurately define the LCL-S-S model:

$$\bar{I}_{in} = \frac{\bar{V}_{in}}{Z_{in}} = \frac{\bar{V}_{in}}{r_s + j \cdot \omega \cdot L_s + \frac{1}{(j \cdot \omega \cdot C_1)} + \frac{1}{\omega^2 \cdot C_1^2 \left(Z_1 + Z_{rORMC} + \frac{1}{(j \cdot \omega \cdot C_1)} \right)}}, \quad (3.10)$$

$$\bar{I}_1 = -\bar{I}_{in} \frac{j}{\omega \cdot C_1 \left(Z_1 + Z_{rORMC} + \frac{1}{(j \cdot \omega \cdot C_1)} \right)}, \quad (3.11)$$

$$\bar{I}_2 = \bar{I}_1 \frac{j \cdot \omega \cdot L_{12}}{(Z_2 + Z_{rIRMC})}, \quad (3.12)$$

$$\bar{I}_4 = \bar{I}_2 \frac{j \cdot \omega \cdot L_{34}}{(Z_4 + R_{eq})}, \quad (3.13)$$

where Z_1 , Z_2 and Z_4 are given by

$$Z_1 = r_1 + j \cdot \omega \cdot L_1, \quad (3.14)$$

$$Z_2 = (r_2 + r_3) + j \cdot \omega \cdot (L_2 + L_3 - 1/(\omega^2 \cdot C_2)), \quad (3.15)$$

$$Z_4 = r_4 + j \cdot \omega \cdot (L_4 - 1/(\omega^2 \cdot C_4)), \quad (3.16)$$

The reflected impedance from the on-board side onto the wheel side (Z_{rIRMC}) is defined in (3.17), while the reflected impedance from the wheel side onto the off-board side (Z_{rORMC}) is described in (3.18).

$$Z_{rIRMC} = \frac{\bar{V}_{43}}{\bar{I}_3} = \frac{\omega^2 \cdot L_{34}^2}{Z_4 + R_{eq}}, \quad (3.17)$$

$$Z_{rORMC} = \frac{\bar{V}_{21}}{\bar{I}_1} = \frac{\omega^2 \cdot L_{12}^2 (Z_4 + R_{eq})}{Z_2 (Z_4 + R_{eq}) + \omega^2 \cdot L_{34}^2}. \quad (3.18)$$

4 Electromagnetic Characterization

The electromagnetic characterization of a MC has an important role in understanding, designing and improving its behaviour. In addition, another valuable application, is the capability of early problems and faults detection on the IPT system (although, this will not be applied in this work). The characterization is based on self and mutual inductances and coupling factor.

It is noteworthy that, despite this chapter being experimental, it was done prior to the simulation, which is an unusual sequence. The reason for such an approach was the data acquisition of k and the coupling profile from both MC. At this point of the work, there were two possible paths to proceed. Firstly, an electromagnetic study could be conducted on the prototype. Subsequently, the obtained results could be incorporated into the simulation, enabling the deduction of results that closely align with the intended goals. This study can either be experimental or done in a FEA tool. The second possible path is through the circuit analysis equations and to initially establish an operating point, resulting in the electromagnetic parameters. With these parameters, simulations can be conducted. However, for the prototype phase, it is necessary to replicate one of the simulation points, leading to an electromagnetic study of the prototype.

The first approach was the one chosen for this work. Firstly, considering the existence of an early prototype stage, it is mandatory to acknowledge certain limitations. For the second approach, where there is no electromagnetic study, one may choose some electromagnetic parameter that are impossible to replicate on the prototype. Then, considering that the prototype's electromagnetic study will be necessary in the two procedures and that this study is independent of the simulation, it was opted to begin with the electromagnetic study.

This chapter presents the electromagnetic characterization of the inWIPT system, considering the MC configurations already referred to in section 3.3, for both MC (IRMC and ORMC). This electromagnetic characterization has the goal of determining the coupling profile. To study the impact on self and mutual inductance and coupling factor of different building aspects, such as air gap, Space Between Turns (SBT), volume of ferrites. The relative position between the wheel and the road was also taken into consideration, as well the impact of lateral displacement and the entry angle of the wheel. Lastly, with all data gathered, the electromagnetic parameters for the final prototype are determined. An early version of the prototype was developed to allow the measurements.

4.1 Experimental measurement and calculation

The electromagnetic characterization is based on an inductor's measurements. Those measurements were conducted using a RLC meter¹. The device equipment is configured to self inductance, " L_s " mode, equivalent serial resistance, "ESR" mode, and the frequency set at 100 kHz, which is the closest to the 85 kHz.

In accordance with the connections illustrated in Fig. 4.1, the self inductances of

¹LRC meter model: 889A from B&K PRECISION

4. ELECTROMAGNETIC CHARACTERIZATION

the transmitter, L_1 a) and the receiver, L_2 b), the anti-series, L_{T-} c) and series, L_{T+} d) arrangements are measured. It is important that during the procedure, the possible excess of cable from points in measurements are completely unwound and faraway from other cable or the returning portion of the same cable. The excess cable from non-used points should be stretched in a different direction. That way, unwanted magnetic fields crossing cables are minimized, resulting in more accurate values. The best solution for more accurate measures was to cut the excess cable, but would result in an unnecessary waste of material and higher costs of the experiment.

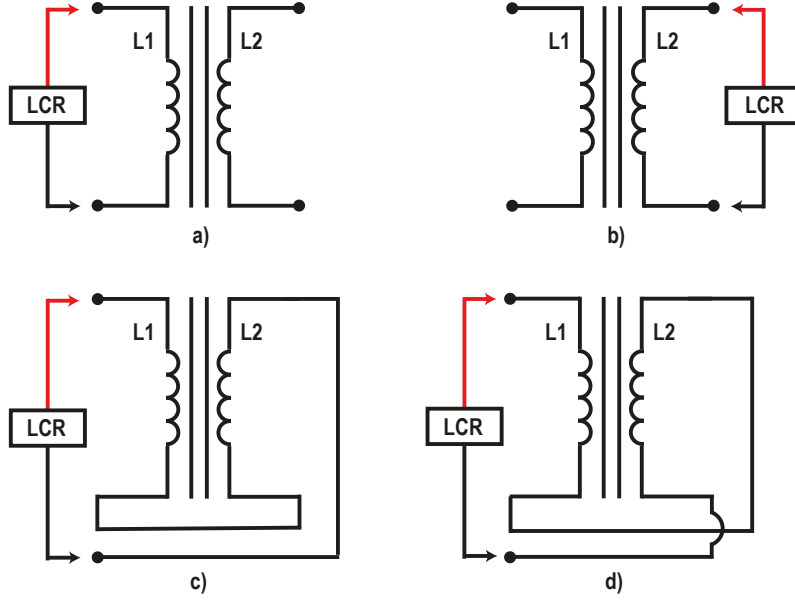


Figure 4.1: Circuit connections for measurements: a) L_1 ; b) L_2 ; c) anti-series; d) series. Adapted from [33].

With the measured values, mutual inductance and coupling factor are calculated from equations 4.2, 4.3, 4.4 and 4.5. In theory, M_+ and M_- should be equal, like k_+ and k_- , but in practice some variations will exist. The total inductance expression, in equation 4.1, is used to write the mutual inductances equations.

$$L_T = L_1 + L_2 \pm 2M \quad (4.1)$$

$$M_+ = \frac{L_{T_+} - L_1 - L_2}{2} \quad (4.2)$$

$$M_- = \frac{L_1 + L_2 - L_{T_-}}{2} \quad (4.3)$$

$$k_+ = \frac{M_+}{\sqrt{L_1 L_2}} \quad (4.4)$$

$$k_- = \frac{M_-}{\sqrt{L_1 L_2}} \quad (4.5)$$

4.2 Prototype

Previously on the inWIPT project, a prototype with a wood structure was built (Fig. 4.2, top right). However, due to the material properties, the shield effect of the rim was despised, and the results were incorrect in comparison with the real application. Another issue was the static behaviour on the x, y and z axis, only possible to rotate on itself. That makes it impossible to the dynamic behaviour of a wheel on a moving car and the relative position to the ground.

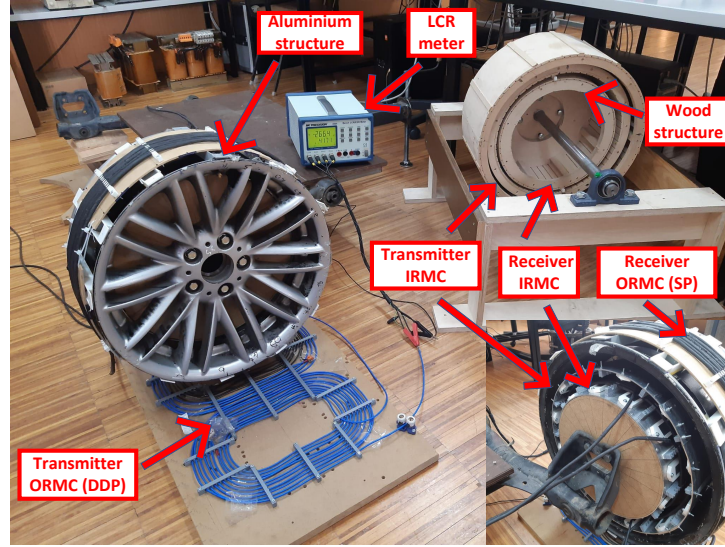


Figure 4.2: Experimental inWheel IPT setup. The aluminium structure is on the left, the preliminary wood structure is on the top right, and the back side of the aluminium structure on the bottom right corner.

The new wheel prototype was developed based on a car rim. The rim is attached to a wheel hub, for now just for support reasons, but later this will offer the possibility of the desired mobility. The rim itself helps with the shielding for the EMI and to block magnetic fields between different MC, and works as support for the pads. Two cylindrical shaped aluminium sheets are used for shielding and support reasons too, on that turn for the IRMC. Another function of the aluminium sheets is to provide a physical protection against external elements, like dust. The ORMC, with the receiver mounted around the rim, is shown on the left side of the Fig. 4.2. The back side, where the two cylindrical aluminium sheets with the IRMC mounted appears, is shown on the bottom right of the Fig. 4.2. The ferromagnetic core used is formed by the N87 material from Epcos with an I shape. 3D printed pieces were developed to support the ferromagnetic cores and the coils.

In Table. 4.1, the dimensions of the prototype are presented for different geometries and air gaps. Furthermore, the values of the diameter (d_{L_x}), where the x is the number assigned to the pad as it was defined in section 3.2; the coil length ($Coil_l$); the coil width ($Coil_w$); the interior coil length ($Coil_{lint}$); the interior coil width ($Coil_{wint}$); and the interior coil length combined ($Coil_{lintcomb}$), are presented. The representation of these values will appear throughout this chapter.

Table 4.1: Experimental setup specifications

Parameter	Value	Parameter	Value
IRMC: SP-SP		ORMC transmitter: DDP	
d_{L3} ($g_{34a} = 15$ mm)	364 mm	$Coil_l$	280 mm
d_{L4} ($g_{34a} = 15$ mm)	322 mm	$Coil_w$	390 mm
d_{L3} ($g_{34b} = 10$ mm)	359 mm	$Coil_{lint}$	115 mm
d_{L4} ($g_{34b} = 10$ mm)	327 mm	$Coil_{wint}$	220 mm
ORMC receiver: SP		$Coil_{lintcomb}$	395 mm
d_{L2}	530 mm		

4.3 Experimental Results

Two sets of experiments were conducted and divided into IRMC and ORMC. An early analysis of the coupling between MCs was made, and it was concluded that the IRMC and ORMC are practically fully decoupled, due to the shielding effect from the aluminium sheets and the car rim. The results are available for review in appendix B.1. That examination validated the intended shielding effect and enabled the independent conduction of experiments for each MC.

4.3.1 Inner Rim Magnetic Coupler

As mentioned in section 3.3, the IRMC configuration will be SP-SP. The goal is to maintain the coupling factor constant, despite the relative position between the transmitter and the receiver, as the transmitter can only rotate around the receiver. An early test indicates that independence, as is shown in appendix B.2.1.

The geometry and placement of the IRMC pads are illustrated in Fig. 4.3 in two different views (front and top views). The transmitter and receiver coils are visually distinguished by the colour orange. The diameter of the coils are d_{L3} and d_{L4} , respectively and they are evenly separated by an air gap g_{34} . Each coil circumference is accompanied by 12 ferrite cores equally spaced covering all the perimeter. They are visually represented by the dark grey colour. The light grey colour represents the aluminium sheets. On the top view of the Fig. 4.3, three variables are introduced, the core width ($core_w$), Space Between Turns (SBT) and the coil width ($coil_w$). It is relevant to note the narrow relation between coil width and SBT variables.

Firstly, an assessment was conducted to determine the impact of the SBT and $coil_w$ on the IRMC characteristic. For this test, a wooden structure was used due to considerations of maximum width, that allowed to achieve a higher number of sampling points. As a result, it enables a coil with twice the width. Another advantage of using the wood structure is to avoid the aluminium shield effect and additionally, no ferromagnetic cores are used. The test was conducted for three coil arrangements with 5, 8 and 10 turns on each pad. For analysis purposes, the arrangement with 5 turns was chosen, since it has more sampling points. For this case, the SBT varied from 2 to 36 mm, which corresponds to a coil width from 42 to 169 mm. Figure 4.4 demonstrates the experimental results of

4.3. EXPERIMENTAL RESULTS

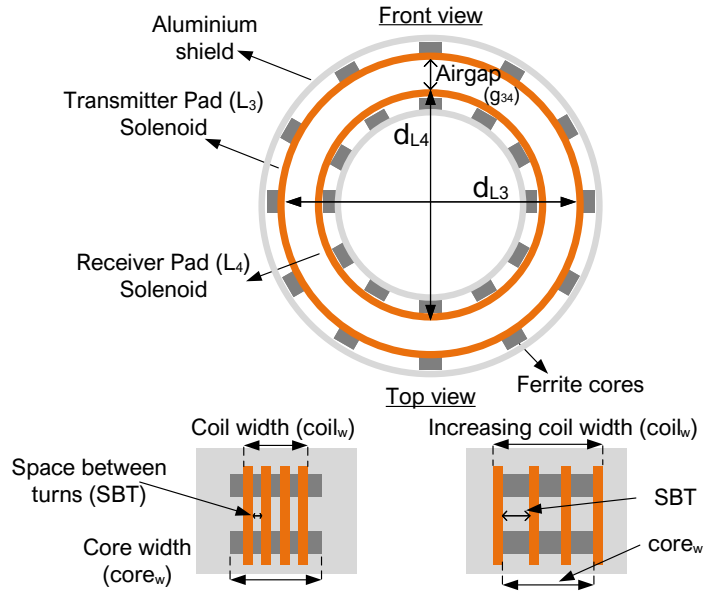


Figure 4.3: IRMC pad geometry and placement.

L_3 , L_4 , L_{34} and k_{34} for the IRMC structure as a function of $coil_w$ and SBT.

As the SBT increased, the self-inductances decreased, as a result of higher values of reluctance. The results of the values of self-inductances L_3 and L_4 , showed a maximum decrease below 42% (Fig. 4.4(a)). The mutual inductance L_{34} follows the same behaviour as the self-inductances, with a maximum decrease below 32% (Fig. 4.4(b)). However, with a higher value of SBT, the coupling factor increases and tends to stabilize around 0.6, Fig. 4.4(b). The other arrangements follow the same tendency. The detailed results for the three arrangements can be found in tables of the subchapter B.2.2 of the appendix.

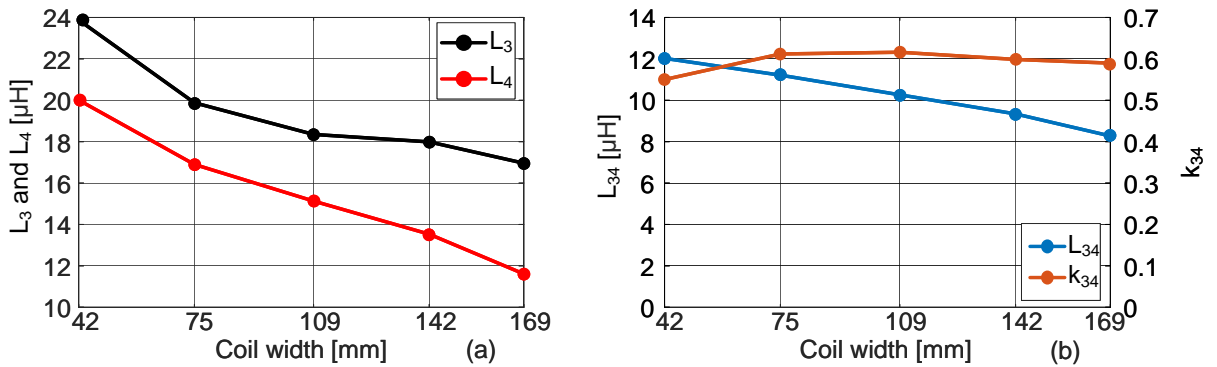


Figure 4.4: Experimental results for IRMC as function of coil width/Space Between Turns for (a) Self-inductances L_3 and L_4 and, (b) Mutual inductance L_{34} and Coupling factor k_{34} .

After completing this initial analysis and experimental tests, the IRMC was assembled in the aluminium structure. On the following test, the goal is to present the shielding effect of the aluminium sheet. This results in a prototype closer to a real implementation scenario, as presented in Fig. 4.2.

The goal of the other IRMC evaluation is to determine the impact of the number

4. ELECTROMAGNETIC CHARACTERIZATION

of turns of each coil, the air gap and the core width. The test involves conducting measurements for different combinations of turns for each pad, maintaining the same number of turns on both pads. The number of turns of the SP coils varies between 2 and 10. The test was repeated for 2 different air gaps ($g_{34a} = 15$ mm and $g_{34b} = 10$ mm) and for two core widths ($core_{w1} = 43$ mm and $core_{w2} = 86$ mm), resulting in four sets of results. The cores used had a size of 43x24x4 mm, with either one or two cores placed side-by-side for a width of 43 mm and 86 mm, respectively. Figure 4.5 shows the experimental results of L_3 , L_4 and k_{34} .

As expected, with the increase of the number of turns, L_3 , L_4 and k_{34} increase too, as shown in Fig. 4.5 a) and 4.5 b). The air gap reduction does not have a significant impact on the self-inductance, with a maximum variation below 5%. For instance, an increase of almost 30% in k_{34} is obtained when 10 turns and $core_{w1}$ are taken into account (from the blue to pink curve on Fig. 4.5(b)). Furthermore, the increase of core material leads to an increase of self-inductances and coupling factor. In this case, for 10 turns, the increase of L_3 and L_4 is close to 100% and for k_{34} around 75% for g_{34a} (from blue to red curve on Fig. 4.5(b)).

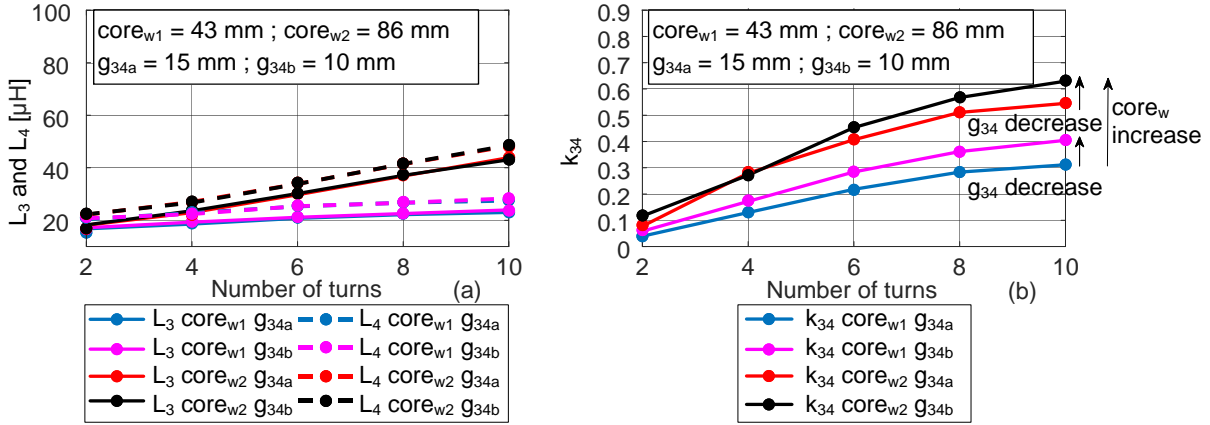


Figure 4.5: Experimental results for IRMC as function of the number of turns, considering different air gaps and, ferrite width, for (a) Self-inductances L_3 and L_4 and, (b) Mutual inductance L_{34} and Coupling factor k_{34} .

4.3.2 Outer Rim Magnetic Coupler

The ORMC pad geometry and placement (DDP-SP) is illustrated in Fig. 4.6. The transmitter geometry from a top view, with the dimensions already described in Table 4.1, are presented on the left. A front view of the ORMC transmitter and receiver is represented on the right side. The SP coil is indicated by the orange colour, the ferrite cores are in dark grey and the aluminium rim is in light grey colour. Furthermore, it introduces the air gap g_{12} , the radius of the receiver coil r_{L2} and the entry angle θ_s . The θ_s is arbitrarily defined with the sole consideration of ensuring it corresponds to a point where the ferrite core is perfectly aligned with the middle of the DDP transmitter pad. This reference point remains the same throughout the remainder of the work.

The first ORMC test evaluates the impact of the entry angle of the wheel. The test consists of varying the angle θ_s between -60° to $+60^\circ$, in intervals of $7,5^\circ$. The relative

4.3. EXPERIMENTAL RESULTS

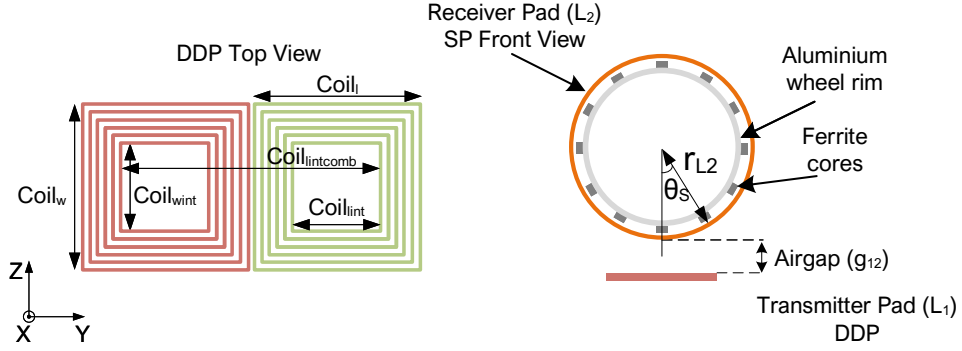


Figure 4.6: ORMC pad geometry and placement DDP-SP.

position between the wheel axel and the DDP transmitter pad remains the same through the samples. For the DDP transmitter pad with 10 turns for each coil (10+10), and for the SP receiver pad 8 turns. The test was conducted for two different core arrangements, 93x28x16mm and 186x28x16mm, which corresponds to a $core_w$ of 93 and 186 mm, and for two lateral displacements M_x , of -50mm and +50mm, beyond the aligned situation. The ORMC characteristics for L_1 , L_2 and k_{12} are presented as a function of the wheel's rotation angle on Fig. 4.7.

From Fig. 4.7, it is possible to analyse that L_1 and L_2 are approximately constant and independent of the wheel rotation angle and the considered M_x values. As expected, the increasing of the $core_w$, increases L_2 . However, it also increases L_1 , despite being on a lower scale. This variation is lower than 10% for L_1 and, around 40% for L_2 . The coupling factor k_{12} is also approximately constant, independently of the wheel entry angle, due to coil symmetry, which is one of the main advantages of the SP topology. When the higher core width ($core_w = 186mm$) is used and the transmitter and receiver pads are aligned ($M_x = 0mm$), the maximum k_{12} is obtained. This value decreases with the lateral displacement ($M_x = -50mm$ and $M_x = +50mm$) and lower core width ($core_w = 93mm$). Nonetheless, the maximum variation is under 30%. The detailed results are presented in tables in the section B.3.1 of the appendix.

Subsequently, another test similar to the previous one was conducted, but in this one, the transmitter pad emulates the movement correlated to the wheel's rotation. In simpler terms, between each measurement point, the wheel (receiver pad) will turn for one direction ($7,5^\circ$) and the transmitter pad will move the length of the perimeter section on the opposite direction (3,4 cm). This way, the dynamic behaviour of the system is replicated and the characteristic curve of the system is obtained. Figure 4.8 represents the wheel movement, the dashed line on the wheel represents a fixed orientation of the wheel. That way, the wheel moves from the left (faded colour) to the right (fully coloured) and it rotates clockwise, passing through the fixed transmitter pad. This test was repeated ten times for different misalignments, from 0 mm (the aligned situation) to 450 mm (fully decoupled) with intervals of 50 mm. The test was conducted with a DDP transmitter with 10 turns for each coil (10+10), and with a SP receiver of 8 turns. In the receiver, 12 ferrite cores were positioned, each measuring 186x28x16mm, equally spaced. That selection allows achieving the maximum coupling factor values. The ORMC characteristics for L_1 , L_2 and k_{12} as function of y misalignment are presented on Fig. 4.9.

4. ELECTROMAGNETIC CHARACTERIZATION

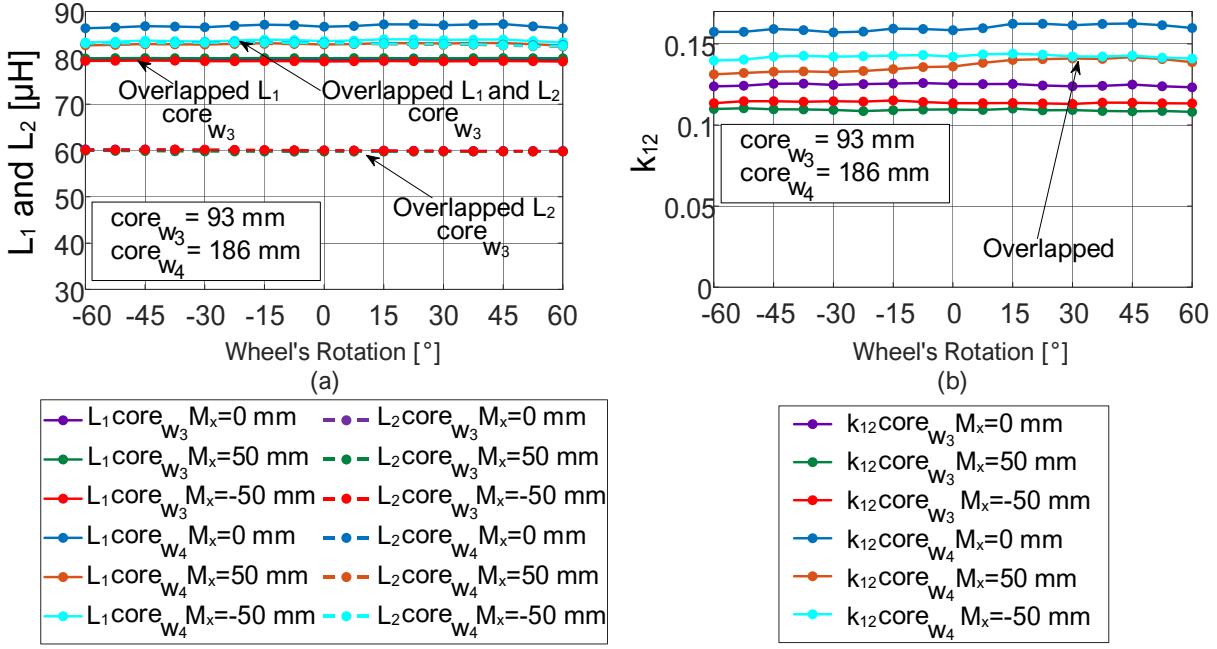


Figure 4.7: Experimental results for ORMC with DDP-SP topology as function of wheel rotation angle, with different misalignment in x axis and different core width, for (a) Self-inductances L_1 and L_2 and, (b) Mutual inductance L_{12} and Coupling factor k_{12} .

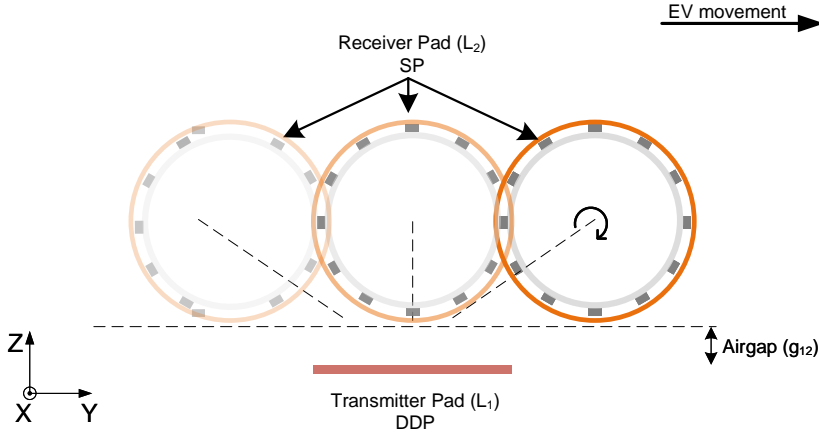


Figure 4.8: Movement and rotation of the ORMC receiver relative to the transmitter.

In Fig. 4.9, it is evident that both L_1 and L_2 are approximately constant and independent of the relative position between the transmitter and receiver pads. The L_1 has a slight variation on values around the y alignment ($y = 0 \text{ mm}$), due to the relation between the impact of the ferrite cores and the shield effect of the aluminium. In addition k_{12} , assumes a Gaussian curvature for the variation of y , with the maximum value corresponding to the aligned situation ($y = 0 \text{ mm}$). Moreover, depending on the x misalignment, the shape is more or less pronounced, being the aligned situation ($y = 0$) with the highest values throughout the curve. Therefore, a comparative analysis between the y alignment points ($y = 0$) of the curves in function of the lateral displacement (x) is presented in Fig. 4.10. It shows a maximum coupling point for $x = 0 \text{ mm}$ (aligned situation) and a

4.3. EXPERIMENTAL RESULTS

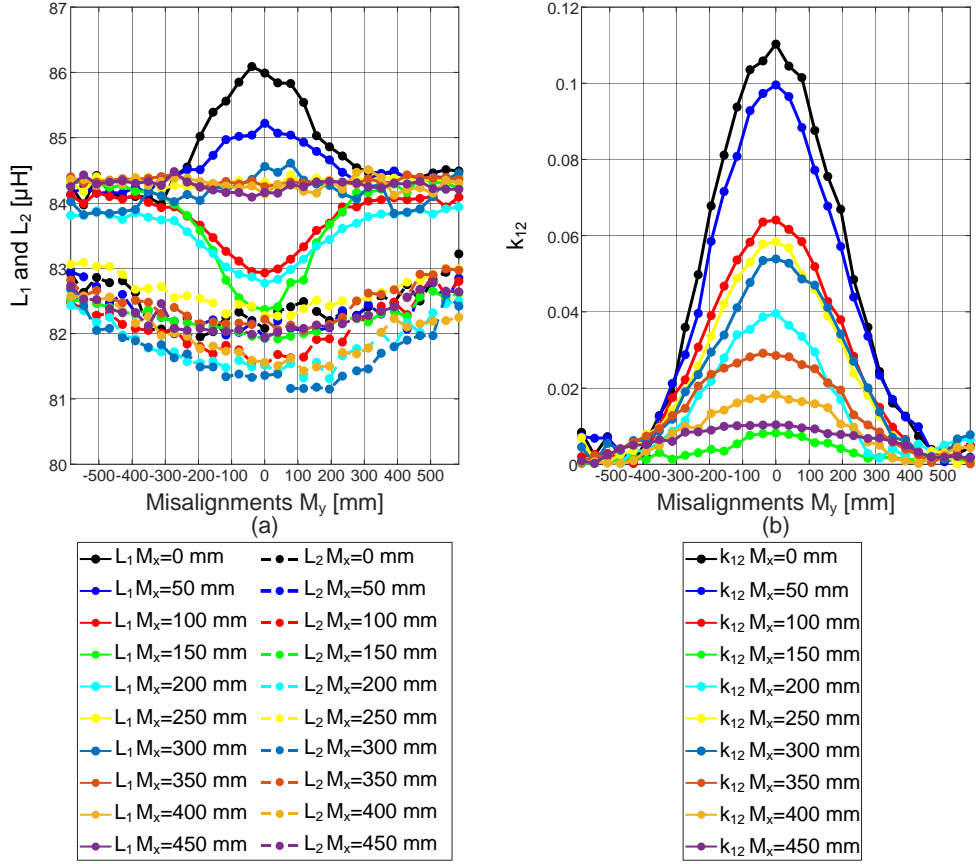


Figure 4.9: Experimental results for ORMC with DDP-SP topology as function of misalignment in x axis, with different misalignments in y axis, for (a) Self-inductances L_1 and L_2 and, (b) Mutual inductance L_{12} and Coupling factor k_{12} .

minimum for $x = 450$ mm (a decoupled situation, where the transmitter pad is out of reach of the aluminium rim). Additionally, there is an inflection point at $x = 150$ mm (where the receiver pad is aligned with the centre of one "D-Pad" of the DDP), followed by a local maximum of the coupling factor at $x = 250$ mm (where the receiver pad is aligned with the lateral of the DDP and the middle of the transmitter coil is out of the limit of the aluminium rim) of lateral displacement. This presents a disadvantage for the selected geometry configuration (DDP-SP). In practice, despite the lateral displacement tolerance being large (450 mm to each side), a point between the alignment and fully decoupled situations will have a coupling factor equal to zero. That leads to scenarios where the car, despite being close to the alignment point, will not charge.

A magnetic configuration for future simulation and prototype was selected, considering all gathered data. It was selected a DDP transmitter with 10 turns for each coil and a SP receiver with 8 turns for the ORMC. Regarding the IRMC, a SP transmitter and a SP receiver, both with 2 turns, were chosen. Those configurations were selected based on the analysis of the equation and also considering some constraints. The first constraint is the range of values available and doable on the prototype. Two others restrictions were considered - the inducted voltage across IRMC and ORMC coils at 1000 V imposed by the European Union regulation [29], and a current of 20 A limited by the cross-section

4. ELECTROMAGNETIC CHARACTERIZATION

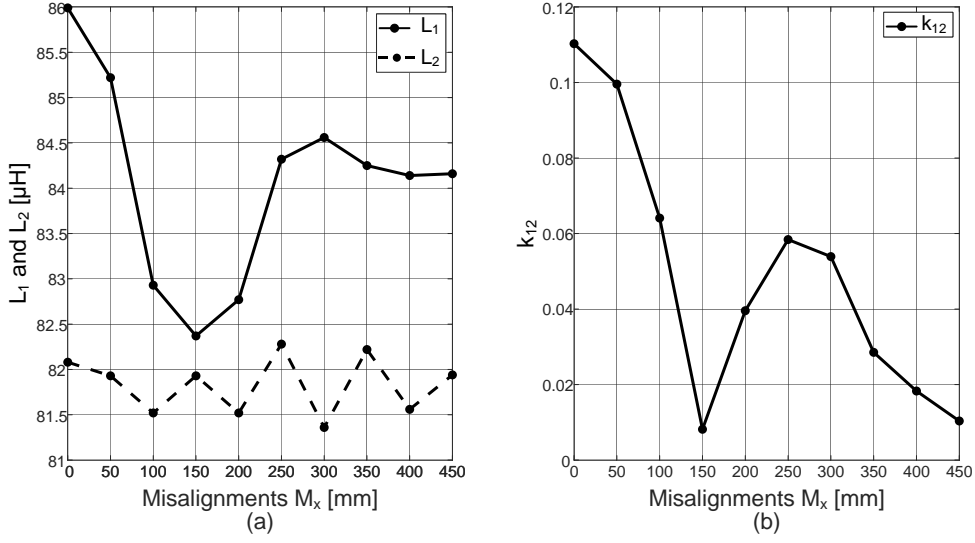


Figure 4.10: Experimental results for ORMC with DDP-SP topology with a $y = 0$ mm as function of misalignments in x axis, for (a) Self-inductances L_1 and L_2 and, (b) Mutual inductance L_{12} and Coupling factor k_{12} .

of the cable used on the coils. The methodology presented in [30] was employed for the equation analysis. First, it was considered the approximation of L_1 equal to L_2 in order to simplify the equations, resulting on equations 4.6 and 4.7. The values V_{in} , P_{bat} and V_{bat} were selected and, with those, it was calculated I_{bat} , I_4 , R_{eq} and V_{eq} . Next, the different combinations of k_{12} and L_{34} were analysed. Those produced results close to the fixed ones and do not trespass the limits previously mentioned. Between those, the combination that results in a maximum value of P_{bat} was selected. The selection obtained resulted in the maximum value of k_{12} and the minimum value of L_{34} . The selection of the highest value of k_{12} will result in a higher I_4 and minimize I_2 , equation 4.6. The value of L_{34} is selected based on the restrictions, mainly the value of I_2 , equation 4.7, and to achieve the selected I_4 . The values of magnetic parameters are presented in Table. 4.2.

$$|\bar{I}_4| = \frac{k_{12}}{L_{34}\omega} |\bar{V}_{in}|. \quad (4.6)$$

$$|\bar{I}_2| = \frac{|\bar{V}_{Req}|}{\omega \cdot L_{34}}, \quad (4.7)$$

4.3. EXPERIMENTAL RESULTS

Table 4.2: Electric parameters for LCL-S-S

Parameter	Value
ORMC	$L_1 = 85,68 \mu H; r_1 = 0,47 \Omega$ $L_2 = 82,17 \mu H; r_2 = 0,2 \Omega$ $L_{12} = [0 \rightarrow 9,61] \mu H; k_{12} = [0 \rightarrow 0,12]$
IRMC	$L_3 = 18,26 \mu H; r_3 = 0,09 \Omega$ $L_4 = 22,26 \mu H; r_4 = 0,06 \Omega$ $L_{34} = 2,74 \mu H; k_{34} = 0,136$
Resonant Components	$L_s = 85,68 \mu H; r_{ls} = 0,47 \Omega$ $C_1 = 40,92 nF; r_{c1} = 0 \Omega$ $C_2 = 34,91 nF; r_{c2} = 0 \Omega$ $C_4 = 157,5 nF; r_{c4} = 0 \Omega$

5 Simulation

This chapter will present the simulation, its results and analyses. The target of this simulation is to emulate the dynamic behaviour of an inWIPT system and assess the feasibility of the prototype, such as ensuring that the voltage and current levels fall within acceptable limits.

5.1 Software

The simulation will be developed and conducted in Matlab[®]/Simulink[®] software, in version 2021b. The Simulink[®] is a block diagram environment for multi-domain simulation and Model-Based Design, and will be used to design/simulate all the system and variables control. The program offers different block libraries for modelling and user interface¹. Simulink[®] is integrated with Matlab[®], which works on a matrix-based language and is able to analyse data, develop algorithms and create models or applications. It will be used to complete an initial data acquisition from Microsoft Excel[®] files, define and calculate some system variable, and at the end of the simulation, import its results from Simulink[®], where they will be processed.

5.2 Model

The model is divided into two main parts: one focused on the electric schematic of the inWIPT system and the other part focused on the position of the car on the road. The electric schematic is composed by four off-board sides and one wheel and on-board side, representing a four transmitter sequence and one wheel of the vehicle. Four off-board sides were selected to subsequently enable a continuous simulation with n pads. This way, when a pad ("n") already does not have influence on the wheel-side, it can replace a following transmitter ("n+4"). Figure 5.1 shows a full view of the simulation model, and Fig. 5.2 represents the electric schematic of the simulation. This subsection includes a summary of the features of the simulations and a review of the main elements.

5.2.1 Magnetic Couplers

The Simscape library already has a MC block called Mutual Inductance, represented in Fig. 5.3 a). The block accepts self and mutual inductance values and their resistances. However, the block does not allow changing the parameters during the simulation, essential to replicate the dynamic behaviour of the ORMC, varying the mutual inductance. Therefore, the Mutual Inductance block will be only used for the IRMC, which will be considered constant according to subchapter 4.3.1.

On [34] a review of three types of models for simulation of the IPT MC is made: the Mutual Inductance Model, a model using equivalent voltage sources, and a model using a

¹The two main libraries are the Simulink, for plots and mathematical operations, and the Simscape, for the electrical component's behaviour.

5.2. MODEL

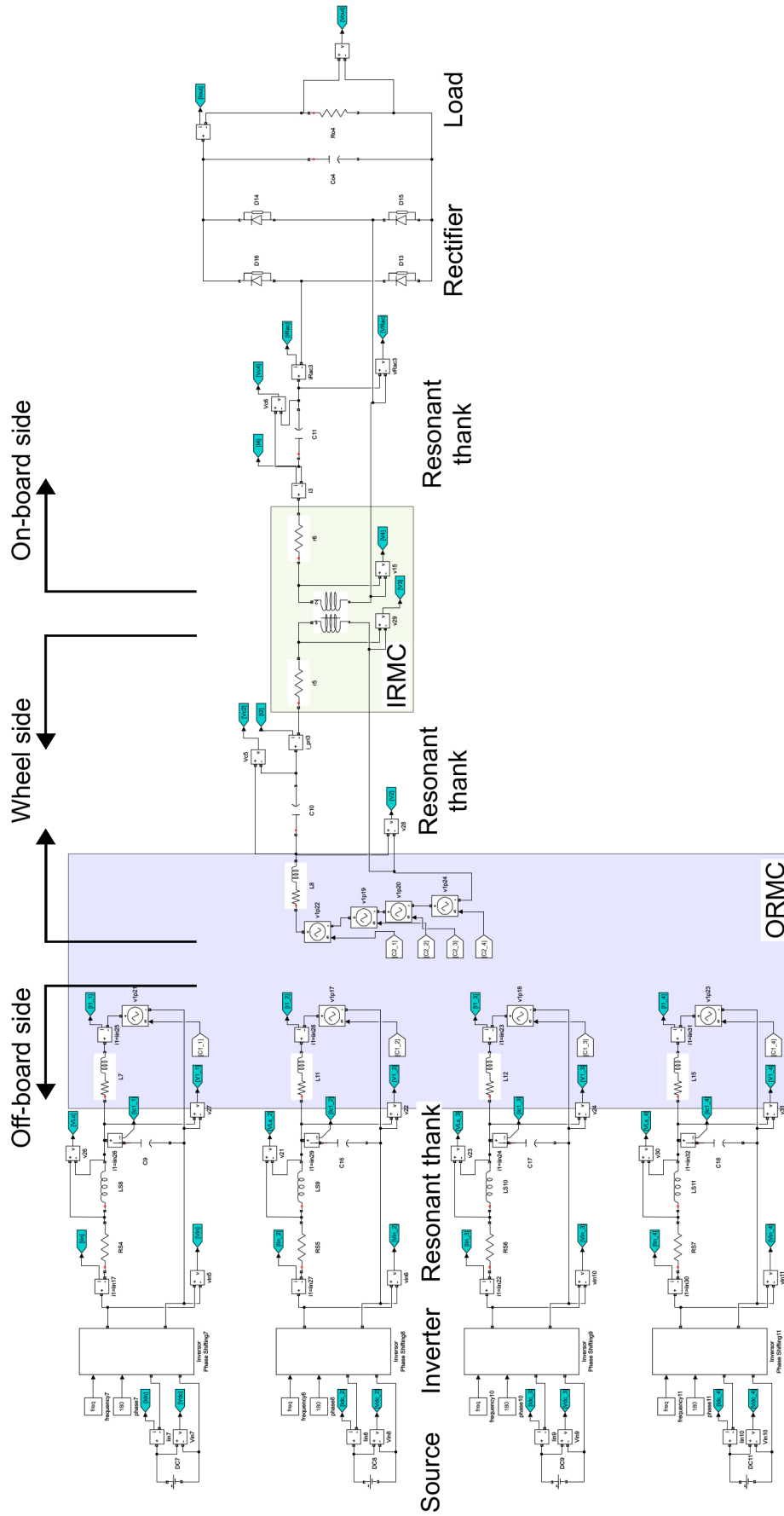


Figure 5.1: Overall simulation model of the double-coupling LCL-S-S.

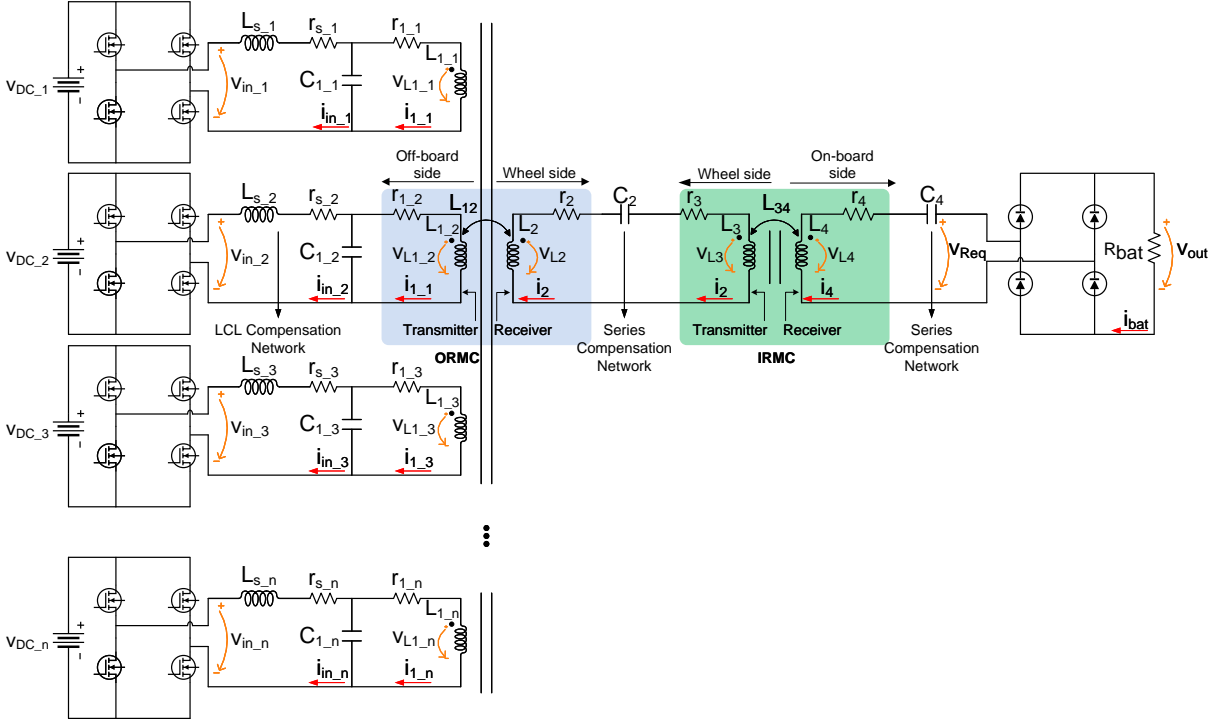


Figure 5.2: Overall electric schematic of the double-coupling LCL-S-S.

T-shaped transformer equivalent circuit. Despite the simulation software being different, some considerations can be taken. The Mutual Inductance Model is simple to implement, but as previously mentioned, it is not capable of replicating the dynamic behaviour. The T-shaped transformer equivalent circuit, proposes the simplest circuit solution and leads to the most accurate results. However, it is not possible to split the contribution of each ORMC transmitter pad and analyse the behaviour of each transmitter. Meaning that, to emulate more than one ORMC transmitter pad for the same receiver, the total profile of the mutual inductance of the path needs to be previously established [35]. The equivalent voltage sources model is the more versatile one, allowing the replication of the electrical schematic of the full system and any individual interaction between two coils. For that reason, it is used for different studies like [36], where the author refers to the example of a IPT system with a DDP-Circular Pad (CP) geometry. This study uses a resonant tank for each "D" of the DDP, two resonant tanks for DDP. This lead to a simulation with three individual coils, all interacting with each other, resulting in three different interactions. On [37] the author proposes an algorithmic control method to maximize system efficiency by altering the mutual inductance for a static application, only possible with this equivalent model.

As a way to vary the mutual inductance of the ORMC, an equivalent model based on the transformer using voltage sources will be used, illustrated in Fig. 5.3 b). The electrical equivalent model is composed of two inductors and two resistances, that will be constants and represent the self-inductances (L_1 and L_2) and their losses (R_1 and R_2), and two controlled voltage sources to emulate the mutual inductance variation. Since it is a dynamic system, depending on the spacing between transmitter pads, there will exist points where more than one transmitter pad is magnetically linked to the receiver

5.2. MODEL

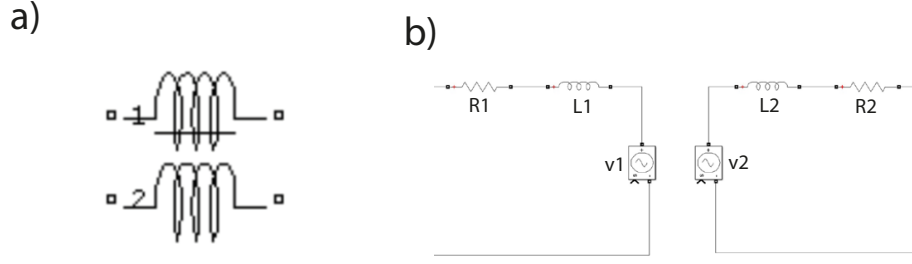


Figure 5.3: Mutual inductance blocks: a) Simscape library; b) Equivalent model.

and transferring power. The sum of the individual contributions from each pad equals the total contribution. So, to mimic that multiple contribution, more than one controlled voltage source will be presented on the receiver side connected in series, one for each linked transmitter. For this, a model with four transmitter pads will be considered, resulting in four controlled voltage sources in series on the receiver side, as is visible on Fig. 5.1.

The voltage sources under control are regulated by equations 2.5 and 2.6, as explained in equations 5.1 and 5.2, which were previously mentioned for ORMC coils. The primary and secondary-sides currents (i_1 and i_2) are measured, and the corresponding voltage is implemented by the controlled voltage sources. Mutual inductance (M_{12}) profile is considered via one 3D lookup table. This process is repeated for each transmitter. The used values were those obtained on the subchapter 4.3.2 and organized on a 3D array, in Fig. 5.4. The 3D lookup table enables the possibility of determining M_{12} from the 3 axis (x , y and z).

$$v_{21} = -M_{12} \cdot \frac{di_2}{dt} \quad (5.1)$$

$$v_{12} = M_{21} \cdot \frac{di_1}{dt} \quad (5.2)$$

5.2.2 Position Determination

Determining the position is crucial to emulate the dynamic behaviour of the EV and calculate the mutual inductance between the transmitter and receiver pads. For a simulation closer to reality, a three-axis movement system is implemented: the horizontal position, x ; the vertical displacement, y ; and the air gap, z . There are three inputs in this position determination system: y , z and v , the velocity. All those inputs are in function of the time. The x position is calculated by the velocity and the simulation time, following the positions laws (equation 5.3). As the equation will be processed every sample time (t_s), the initial position (x_0) and the initial velocity (v_0) will be the previous position ($x(t-1)$) and previous velocity ($v(t-1)$). The time t will be equal to t_s , and the acceleration will be null. Therefore, equation 5.3 results in equation 5.4.

$$x(t) = x_0 + v_0 \cdot t + \frac{1}{2} \cdot a \cdot t^2 \quad (5.3)$$

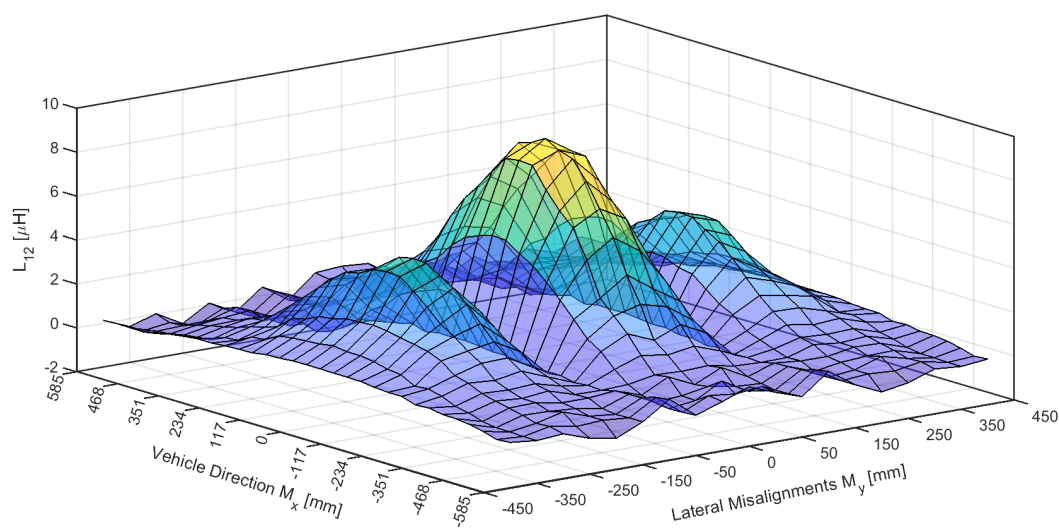


Figure 5.4: One layer of the 3D array, corresponding to data from the mutual inductance of the ORMC (L_{12}) of one air gap ($x_{airgap} = 40 \text{ mm}$).

$$x(t) = x(t - 1) + v(t - 1) \cdot t_s \quad (5.4)$$

Input variables will be defined in a different Simulink[®] file and stored in the Matlab[®] workspace. In this way, it is possible to check if any value is out of range, since the limits of the range are the extremes of the data collected. If those limits are exceeded, Matlab[®] will send a warning message and new data can be introduced or not. The position values will be used to get the mutual inductance data, so in case of out of range values, the mutual inductance will assume the value of the last point of the range of that variable.

Other parameters can be defined, such as the space between ORMC transmitter pads, the number of ORMC transmitter pads and the initial position of the car.

5.2.3 Power Converters

The model uses two types of power converters, a single-phase full-bridge inverter with four MOSFETs, and an uncontrolled single-phase bridge rectifier with four diodes. The inverter is placed between the source² and the transmitter pad of the ORMC, converting DC to AC and establishing the system frequency (85 kHz). The electric schematic is represented in Fig. 5.5 a). A square wave with 50% duty-cycle to control the MOSFETs, resulting in a fundamental harmonic component (described by equation 5.5).

$$v_{1rms} = \frac{4}{\pi \cdot \sqrt{2}} \cdot V_{DC} \quad (5.5)$$

The rectifier is placed between the IRMC receiver and the load (battery or motor), and converts from AC to DC, as shown in Fig. 5.5 b). This is an uncontrolled process, and there is no need for a control signal. The average load voltage is given by equation

²It is used a DC source.

5.3. RESULTS

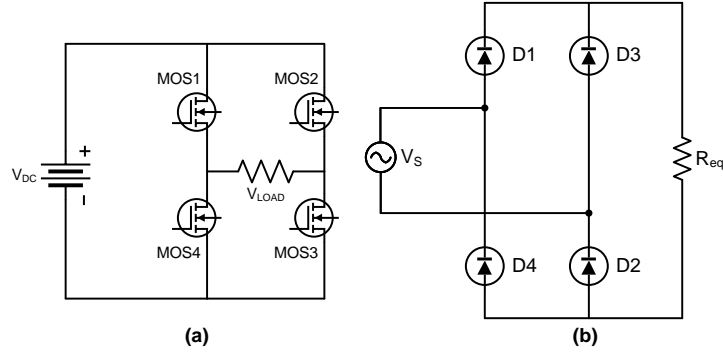


Figure 5.5: Electric schematic of: a) the inverter; b) the rectifier.

5.6 for the fundamental frequency, where the source voltage V_s is the voltage after at the resonant tank of the IRMC receiver.

$$v_{load_{av}} = \frac{1}{\pi} \int_0^{\pi} \sqrt{2} \cdot V_s \cdot \sin\theta \, d\theta = 0,9 \cdot V_s \quad (5.6)$$

5.3 Results

This subsection presents some tests conducted with the developed Simulink model. First, an exploration of aspects related to the system's capacity will be undertaken. Subsequently, an analysis of the impact of the velocity on the system will be conducted. Then, a brief comparison between the connections to power the transmitter pads will be made. Throughout this subsection, all simulations will employ the parameters outlined in Table. 4.2 and will initiate from a steady state of the system.

The first test simulates the wheel passing through a transmitter pad for the aligned situation ($y = 0$) (case a) and, following that, the simulation was repeated with 100 mm of misalignment ($y = 100$) (case c). The other variables, such as air gap and velocity, remain constant throughout and between simulations. A velocity of 50 *km/h* and an air gap of 40 *mm* were considered. Additionally, a third simulation was conducted considering the same velocity, an aligned situation and an air gap of 45 mm (case b) and afterwards compared with the previous ones. This air gap was estimated with 70% of the 40 mm air gap. That way, it is possible to compare another capability of the model. Figure 5.6 demonstrates the obtained results, where the blue curves correspond to case a, the green curves correspond to case b and the red curves to case c.

As expected, the misalignment resulted in a decrease of L_{12} , in comparison with the aligned situation. The decrease in L_{12} leads to a reduction of i_2 (equation 3.12) and consequently a decrease of i_4 (equation 3.13), resulting in a reduction of energy transmitted. However, the current in L_1 (i_1) is constant and independent of the coupling of the ORMC pads, being constant from 0 to L_{12} maximum. This is the main advantage that enables the dynamic operation of the inWIPT system.

The second group of tests aims to study the impact of the velocity on the energy transferred. Two sets of tests were conducted, one fixing the time frame throughout the

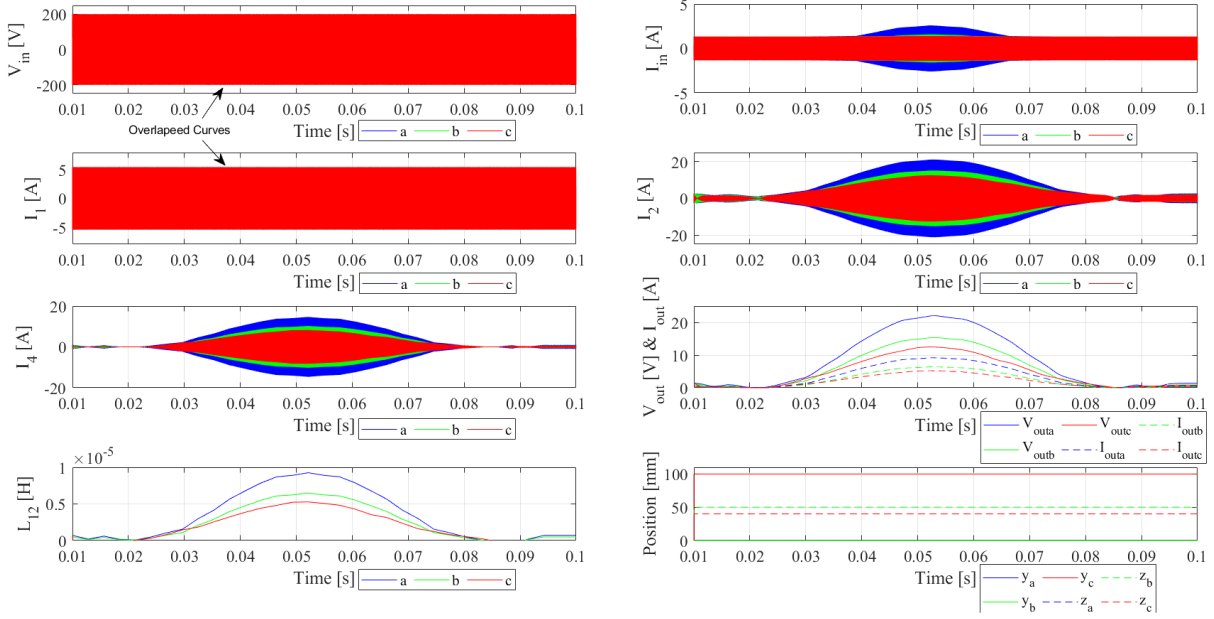


Figure 5.6: Simulation results for the impact of the air gap and misalignment. v_{in} , i_{in} , i_1 , i_2 , i_4 , v_{out} , i_{out} , L_{12} and y and z positions.

simulations and the other fixing the number of transmitter pads. The first test involved comparing the energy transferred within a time frame of 0.5 seconds, while varying the velocity of the car. The test was made for two different distances between ORMC transmitter pads (d_{pad}), 500 mm and 1000 mm, and three different velocities, 50, 85 and 120 km/h, considering the minimum and maximum velocity of highways in Portugal. Figure 5.7 shows the L_{12} , v_{out} and i_{out} for a d_{pad} of 500 mm and the minimum and maximum velocities (on the two first lines of the figure, corresponding to four graphics). Between the two lines of the "time framed" section, the time frame is constant, changing the number of peaks of L_{12} that correspond to ORMC transmitter pads. The behaviour of the system for the six situations is shown in Appendix C.2.1 and the energy transferred for one hour is presented in Table 5.1, in the "Time Framed" rows. On the table, there is also presented the number of ORMC transmitter pads that interact during the time frame.

From the examination of the energy transferred for the different velocities, it is notable that the energy transferred can increase or decrease with the increase of the velocity, depending on the d_{pad} . With an increase in d_{pad} , less energy is transferred as velocity increases. This behaviour was expected once the ORMC receiver pad has less time interacting with the ORMC transmitter pad. However, at higher speed, the ORMC receiver pad interacts with more ORMC transmitter pads. Additionally, when the d_{pad} is lower, the total L_{12} remains more constant and with a higher peak. This behaviour is attributed to the cumulative contribution of each ORMC transmitter pad, being more independent of the velocity. Consequently, the difference between the energy transferred for a d_{pad} of 500 mm can be influenced by the speed at which the first peak is reached.

Then, a second test was conducted to compare the energy transferred throughout 8 ORMC transmitter pads, while varying the velocity. The test was repeated for the same d_{pad} and velocities of the previous one. Figure 5.7 shows the L_{12} , v_{out} and i_{out} for a d_{pad} of

5.3. RESULTS

1000 *mm* and the minimum and maximum velocities (on the two bottom lines). A reverse situation occurs on the "Number of transmitters" compared with the previous test, where the number of peaks of L_{12} is constant, changing the time frame. The behaviour of the system for the six situations are shown in Appendix C.2.2 and the energy transferred for one hour is presented in Table. 5.1, on "n° Transmitters" rows.

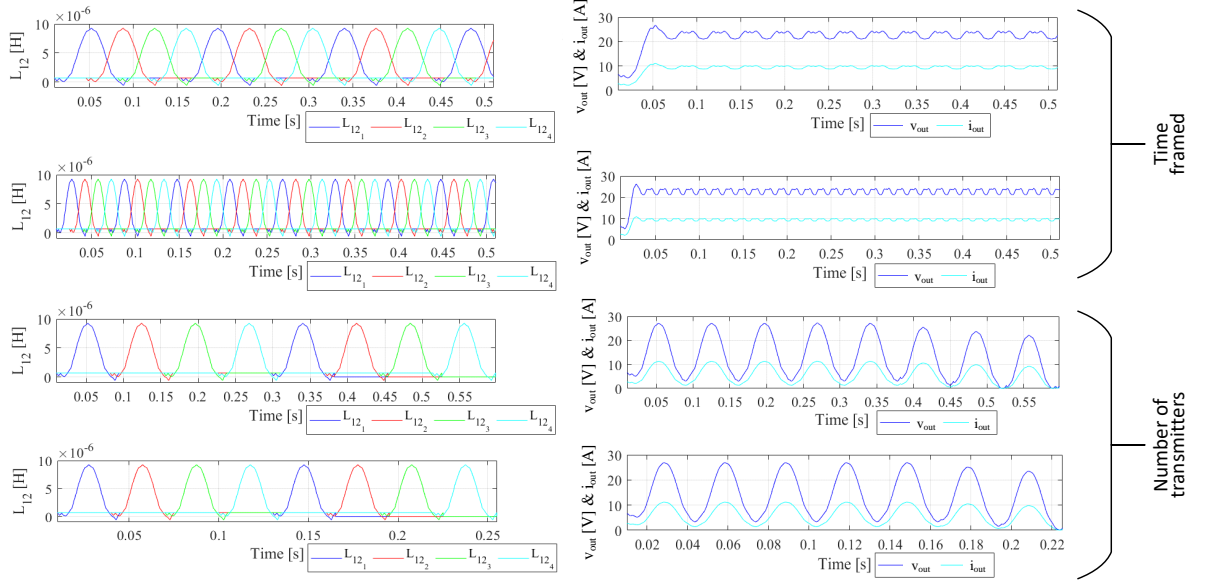


Figure 5.7: L_{12} values and results of i_{out} and v_{out} to velocities of 50 and 120 *km/h*. The "Time framed" represents tests with a d_{pad} of 500 *mm* and the "n° Transmitter" represents tests with a d_{pad} of 1000 *mm*.

Table 5.1: Energy transferred depending on the velocity and the distance between pads.

Distance between pads (d_{pad})	Velocity	Energy transferred	Number of pads	
500 <i>mm</i>	50 <i>km/h</i>	208,008 <i>Wh</i>	13	Time Framed
	85 <i>km/h</i>	212,256 <i>Wh</i>	23	
	120 <i>km/h</i>	213,696 <i>Wh</i>	33	
1000 <i>mm</i>	50 <i>km/h</i>	121,032 <i>Wh</i>	7	Time Framed
	85 <i>km/h</i>	120,744 <i>Wh</i>	12	
	120 <i>km/h</i>	118,8 <i>Wh</i>	17	
500 <i>mm</i>	50 <i>km/h</i>	171,007 <i>Wh</i>	8	n° Transmitters
	85 <i>km/h</i>	167,724 <i>Wh</i>	8	
	120 <i>km/h</i>	164,614 <i>Wh</i>	8	
1000 <i>mm</i>	50 <i>km/h</i>	102,771 <i>Wh</i>	8	n° Transmitters
	85 <i>km/h</i>	101,398 <i>Wh</i>	8	
	120 <i>km/h</i>	99,874 <i>Wh</i>	8	

On this test, it is more noticeable that for higher speeds, the energy transferred for the same distance decreases. This is the expected result, since for higher speeds, the ORMC transmitter and receiver will have less time interacting with each other. The reduction

of the energy transferred from a d_{pad} of 500 mm to 1000 mm is explained by the total distance increase of almost 75%, leading to a higher total time and the justifications already mentioned on the previous test.

The last group of tests analyses the effect of different ways to power the ORMC transmitter pads. The test is conducted with three ORMC transmitter pads compared in three distinct situations. In situation d , each pad is powered by its own power converter; in situation e , the transmitter pads are connected in series, using only one power converter; and in situation f , the transmitter pads are connected in parallel, and only one power converter is used. The remaining parameters remain constant throughout and between simulations. The results are presented in Appendix C.3 and a comparison is presented on Fig. 5.8.

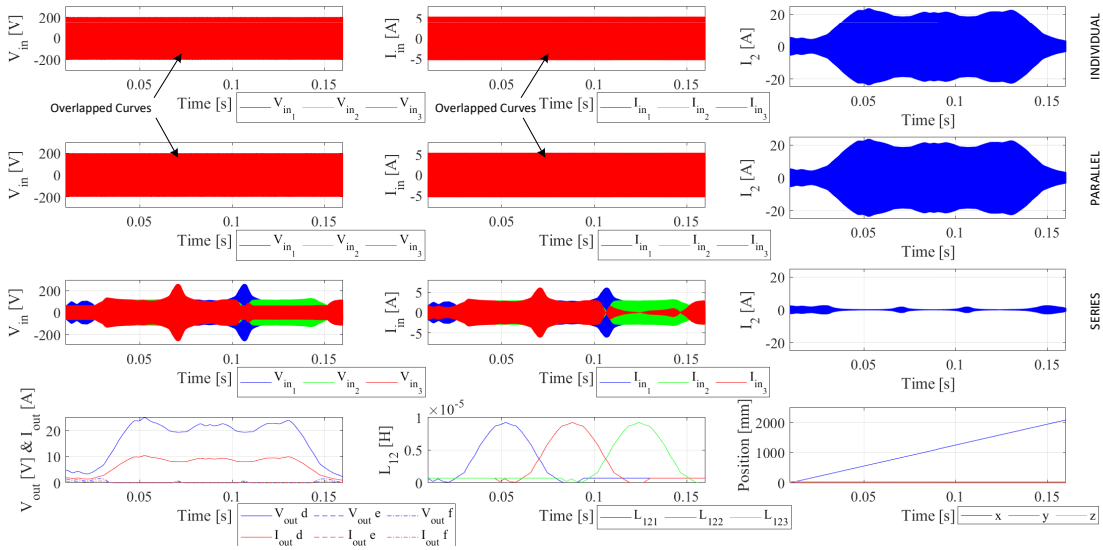


Figure 5.8: Comparison of simulation results to assess the impact of different sources arrangements. v_{in} , i_{in} and i_2 for the situation d on the first row, f on the second row and e on the third row. v_{out} , i_{out} , L_{12} and x , y and z position on the last row for all situations.

Upon initial examination of the curves, the notable difference between the situation e and the other two is evident. On situation e , the voltage delivered by the source is oddly distributed between the transmitter pads and follows the behaviour of i_1 . i_1 is dependent on the load and loses the main characteristic of this resonant tank. The current and voltage at the load are nearly zero. Situations d and f have a similar behaviour and, from the viewpoint of the vehicle, are indistinguishable. The only difference arises on the off-board side when the current delivered by the DC bus is three times larger on the situation f . This results from the characteristics of the resonant compensators used (LCL-S-S) that deliver a i_1 constant current. This way, each transmitter pad will request the same amount of current from the source, resulting on the number of transmitter pads times the current requested on situation d .

6 Experimental Validation

A real scale model was built in order to validate the simulation results and the concept of the inWIPT system. The model is designed to emulate the EV motion and the behaviour of the inWIPT system applied to one wheel. A part of the prototype was already mentioned in chapter 4, specifically the MC and the wheel design. This chapter focuses on the building aspects and elements of the prototype, presenting the results and their respective discussion.

6.1 System Specifications

A simplified 3D modelled¹ image of the final prototype is shown in Fig. 6.1. The model uses a trailer as the base structure. Two wheel hubs and rims are attached to the trailer, one to implement the inWIPT and the other is used only for the structure and balance of the model (can be used to implement other inWIPT in the future).

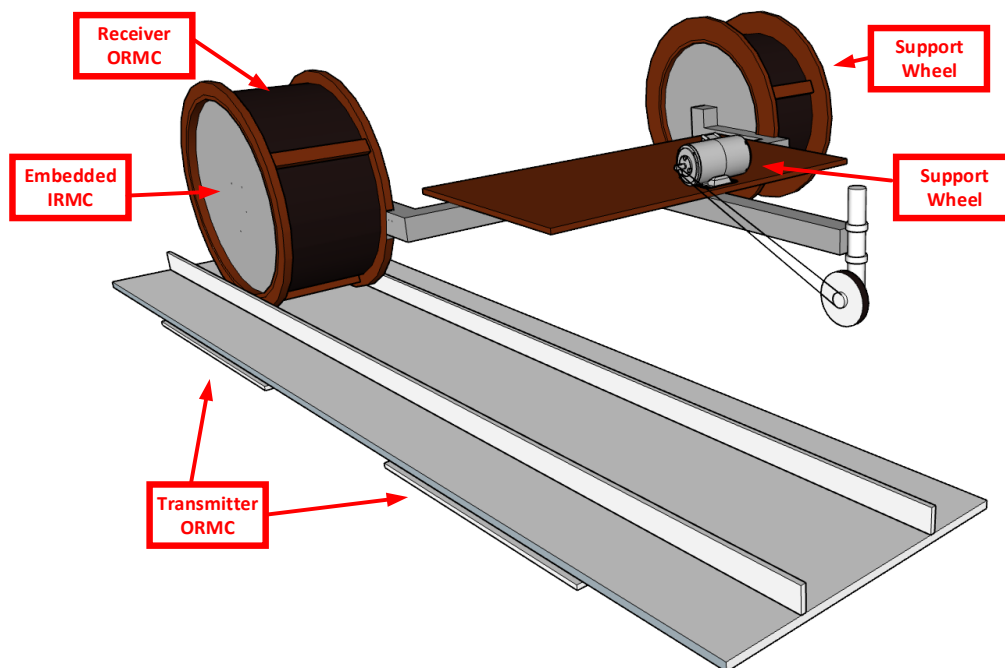


Figure 6.1: 3D model of the prototype.

Two transmitter pads coils are placed on the ground, each one supported by a medium-density fibreboard (MDF) and attached to it with 3D printed pieces. Having the two transmitter coils in separate boards allows a free placement relative to each other, being the distance between transmitter pads a component of the study. Additionally, another

¹Modelled in Sketchup

MDF is placed on top of the coils to offer protection and a smooth surface to the movement of the trailer, otherwise the bumps would influence the results. This placement independence of the transmitter pads allows the emulation of the lateral displacement. Two wooden slats are glued on top of the last MDF to serve as a guideline, limiting the movement of the wheel, in order to achieve a linear movement. To protect the receiver coils of the ORMC, two ring shaped MDF pieces are placed on the limit of the rim with a slot that fits it and are fixed using a piece of MDF screwed against the two rings, compressing the rings to the rim. On the other wheel, a similar structure is placed, but this one has the exterior diameter larger to counterbalance the height of the emulated road. All dimensions related to the MC have been already mentioned in Table. 4.1 and a full review of all dimensions is provided in appendix A.

The air gap of the model as function of the model dimensions is given by equation 6.1, where d_{r1o} is the diameter of the ring of wood that emulate the tire height, the d_{L2} is the diameter of the ORMC receiver coil (L_2), Mdf_{t_1} is the mdf thick that emulate the asphalt, and the $Suppc_t$ is the thickness of the cover of the support pieces for the coils ($Suppc_t = 2 \text{ mm}$).

$$g = \frac{d_{r1o} - d_{L2}}{2} + Mdf_{t_1} + Suppc_t \quad (6.1)$$

The Litz wire is used to build the coils in order to minimize power loss. This wire is composed of individually insulated wires that are twisted into an uniform pattern. This way, the Litz wire increases the amount of surface without increasing the size of the conductor, which reduces the skin effect² due to be more intense to higher frequencies of the system.

Lastly, a traction system had been planned to control the movement and speed of the prototype. The system was composed by a third wheel placed on the front part of the trailer and a transmission belt to transfer the motion from a motor, also fixed in front of the trailer. The control was taken from a treadmill that uses an encoder to ensure a fixed velocity. That way, the system can work at different velocities and may change during the experiment. Unfortunately, it was not possible to implement, therefore as an alternative, a third wheel was placed on the front part of the trailer to smooth the movement, and a rope was used to pull the trailer.

The final result of the prototype and the measurement equipments used are shown on Fig. 6.2.

6.1.1 Power Converters

For the prototype, three power converters were used — two inverters and one rectifier. The inverters are constituted by a H-bridge of MOSFETs, two drivers to make the control, an interface board and the Digital Signal Processor (DSP), as is shown on Fig. 6.3. The N-channel MOSFETs used were C2M0025120D, capable of supporting up to 1000

²The skin effect is the tendency of alternating high-frequency currents to crowd toward the surface of a conducting material. This phenomenon restricts the current to a small part of the total cross-sectional area and so has the effect of increasing the resistance of the conductor. [38]

6.2. RESULTS

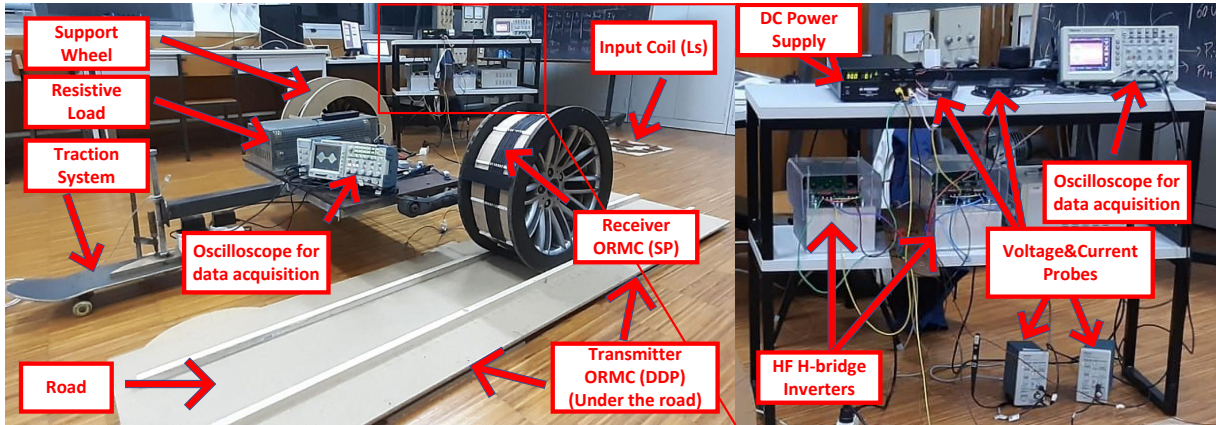


Figure 6.2: Final prototype. At the left a full view of the system, and at the right the support bench.

V and 90 A . The driver used was the PT62SCMD12 from the Prodrive Technologies, to offer galvanic isolation, fault detection and adapt the output signal. The interface board adapt the voltage values of the DSP output to use on the driver input and also offer isolation through optocouplers. The DSP used is the TMDSCNCD28335 card joint with the Peripheral Explorer, both from Texas Instruments. The DSP is responsible by generating the control signals, establishing the frequency of commutation and phase shifting. The rectifier is composed by four FEP30AP diodes, supporting until 50 V and 30 A .

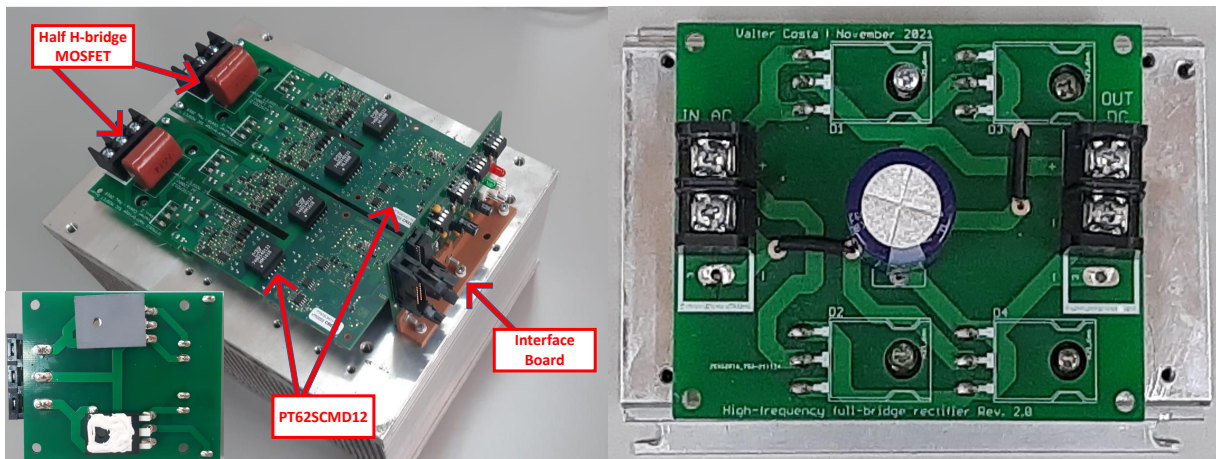


Figure 6.3: On the left side, a full view of the inverter fully mounted. In the bottom left corner, a back view of one half H-bridge on the assembly phase, the top MOSFET is covered by an insulating film and the bottom one with thermal paste. On the right side, a full view of the rectifier.

6.2 Results

To validate the Matlab[®]/Simulink[®] model and prove the concept of the inWIPT system for dynamic applications, two sets of experiments were conducted. The first set is focuses

on the analysing the system's static behaviour, while the second focuses on analysing its dynamic behaviour. Before the experimental tests, all the system elements were measured with the prototype fully mounted. The values have suffered some variation in comparison with the values presented in chapter 4. The most significant variation was on the self inductances of the IRMC, L_3 and L_4 , with a decrease of 78,59% and 53,41%, respectively. This variation occurred because the excessive cable length (reason already mentioned on the Chapter 4), was shortened in the final prototype. Table. 6.1 shows the measured values. Another difference worth of highlighting is some variation from the theoretical values of the capacitors. This will result in a different resonant frequency for each mesh. For the purposes of the test, the resonance point was taken to be the resonant frequency of the ORMC transmitter network. At the resonant frequency, the square wave at the exit of the inverter, V_{in} , presents high levels of distortion, affecting all the system. This may occur due to the dead time of the drivers and hard switching from the MOSFET's. For this reason, a frequency close to the resonant point will be used.

Table 6.1: Electric parameters for LCL-S-S

Parameter	Value
V_{dc}	30 V
f_s	84,35 kHz
ORMC	$L_1 = 84,97 \mu H; r_1 = 0,44 \Omega$ $L_2 = 77,38 \mu H; r_2 = 0,2 \Omega$ $L_{12} = [0 \rightarrow 9,05] \mu H; k_{12} = [0 \rightarrow 0,11]$
IRMC	$L_3 = 3,91 \mu H; r_3 = 0,48 \Omega$ $L_4 = 10,37 \mu H; r_4 = 0,11 \Omega$ $L_{34} = 3,06 \mu H; k_{34} = 0,48$
Resonant Components	$L_s = 83,25 \mu H; r_{ls} = 0,47 \Omega$ $C_1 = 38,8 nF; r_{c1} = 0,08 \Omega$ $C_2 = 44,01 nF; r_{c2} = 0,11 \Omega$ $C_4 = 343,43 nF; r_{c4} = 0,61 \Omega$
C_o	470 μF
R_o	2,4 or 7,2 Ω

6.2.1 LCL-S-S

Static Operation

The first set of tests aims to measure and analyse the static behaviour of the system for two distinct wheel positions, relative to the ORMC transmitter, on the x axis, and two different loads. The positions were chosen to include the maximum and minimum values of L_{12} , resulting in the positions 0 mm (aligned) and 585 mm (fully decoupled). Resistances of 2,4 Ω and 7,2 Ω were used for the load. A DC bus of 30 V was used. Figures 6.4 and 6.5 and on Appendix Fig. D.4 and D.5 presents the experimental and simulation results, in the top and bottom rows, respectively. The images on the left show the curves of v_{in} , i_{in} , i_1 and i_2 in blue, cyan, pink and green, respectively. The images on the right show the curves of v_{in} , i_4 , v_{out} and i_{out} at blue, orange, red and yellow, respectively. The

6.2. RESULTS

same scales were used for the experimental and simulation scopes. Throughout the entire chapter, the simulation results will be presented in the top row and labelled as a) and b). The experimental results will be displayed in the bottom row and labelled as c) and d).

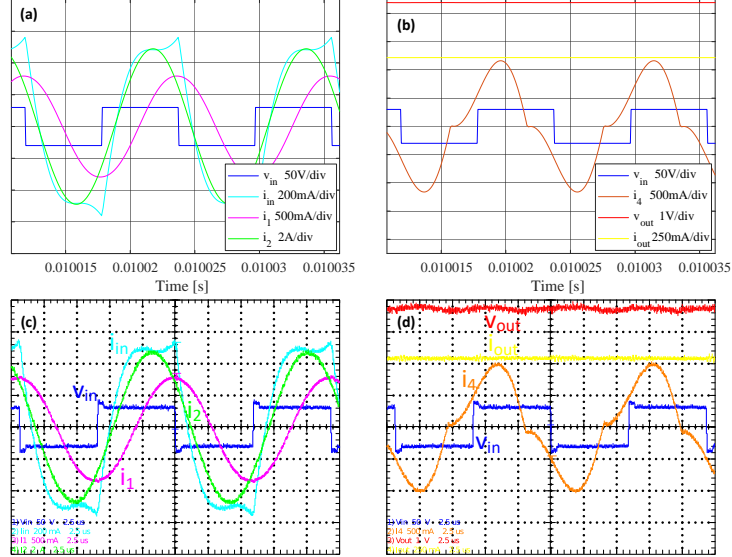


Figure 6.4: Static results for a load of $7,2 \Omega$ on an aligned situation. a) & c) shows v_{in} [50V/div], i_{in} [200mA/div], i_1 [500mA/div] and i_2 [2A/div] in blue, cyan, pink and green, respectively. b) and d) v_{in} [50V/div], i_4 [500mA/div], v_{out} [1V/div] and i_{out} [250mA/div] in blue, orange, red and yellow, respectively.

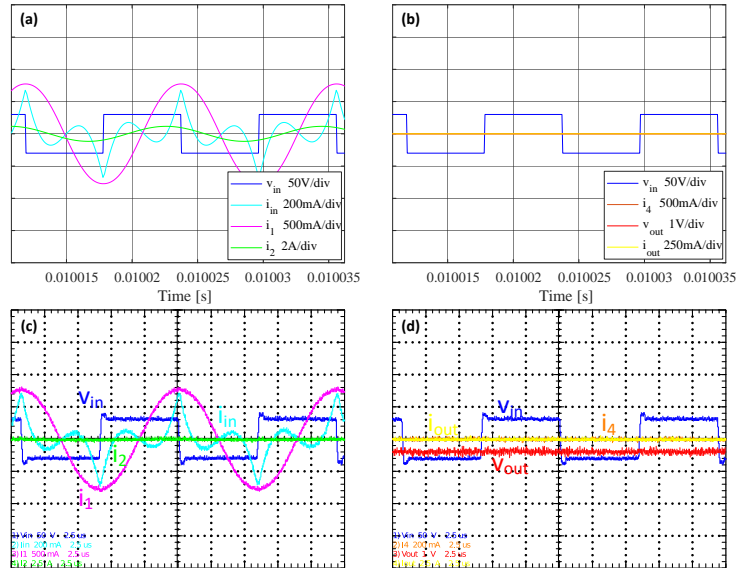


Figure 6.5: Static results for a load of $7,2 \Omega$ on a decoupled situation. a) & c) shows v_{in} [50V/div], i_{in} [200mA/div], i_1 [500mA/div] and i_2 [2A/div] in blue, cyan, pink and green, respectively. b) and d) v_{in} [50V/div], i_4 [500mA/div], v_{out} [1V/div] and i_{out} [250mA/div] in blue, orange, red and yellow, respectively.

Upon the initial analysis of the results, particularly focusing on the off-board side, it became apparent that the behaviour of i_1 is independent of the load and of L_{12} . This

characteristic, with no parameter tending to infinite, is crucial for the selection of this resonant topology for a dynamic operation. Furthermore, it was visible that the power requested from the source is regulated by the amplitude of i_{in} , with the phase between the voltage and the current being constant throughout tests. i_{in} increased with the increase of the load or of L_{12} . For the wheel side, i_2 decreased with the decrease of L_{12} or the load, as described in equation 3.12. On the on-board side, i_4 increased with the increase of i_2 . When the load increased, for the same situation, i_4 increases despite i_2 decreasing, as shown in equation 3.13. For the coupled situations, the power delivered to the load was of 2,64 and 2 W for a load of 7,2 and 2,4 Ω , respectively. The voltage gain (voltage at the load divided by the voltage at the source) was of around 0,14 and 0,07 for a load of 7,2 and 2,4 Ω , respectively. The experimental results, present values close to the simulation.

Dynamic Operation

The second set of tests consists of measurement of the dynamic behaviour of the system. An early test was conducted in order to evaluate the impact of the polarity of the transmitter pads. The behaviour of the system was measured by powering the transmitter pads with the same polarity and then changing the polarity of one of them. Results are presented on Appendix D.1. The polarity leads to a cumulative or a subtractive situation, where the L_{12} of both pads adds or cancel each other, respectively. Figure D.3 in the appendix illustrates two pairs of ORMC transmitter pads, with the currents and magnetic field orientation denoted, for both cases. On the left, the pads have the same polarity, with the current on the central part of the pad with the same orientation. This leads to a magnetic field with the same orientation on both pads, that will sum to each other. In the right, the pads have opposite polarity, with currents on the central part of the pad with opposite orientations. This leads to a magnetic field with the opposite orientations on each pad, that will subtract to each other. On the situation where the L_{12} adds to each other, the energy transferred was 111% higher than in the other. A polarity with an cumulative behaviour was used for the remaining dynamic tests.

Dynamic tests move the trailer along 2200 mm, passing through 2 ORMC transmitter pad. It was considered two d_{pad} , 500 and 1000 mm at the same velocity (approximately 1,6 km/h), and then repeated for a higher velocity (approximately 3,2 km/h) for a d_{pad} of 500 mm. The load of 7,2 Ω and a DC bus of 30 V were used. For the simulation, a velocity 10 times higher was used, due to hardware limitations. The experimental and simulation results are presented on Fig. 6.6, 6.7 and 6.8. The images on the left show the curves of v_{in} , i_{in} , and i_1 of the first transmitter pad. The images on the right show the curves of i_4 , v_{Req} , v_{out} and i_{out} . The same scales were used for the experimental and simulation scopes.

From the point of view of the off-board side, for the three samples, there were no major differences. The independence of i_1 from the load and from L_{12} , and the dependency of i_{in} , with the approximation of the wheel to the middle of the first ORMC transmitter pad were validated once more. It was deduced that the behaviour of the second pad was similar, with a shift on the timescale. For the wheel and onboard sides, all the currents and voltages increase with the proximity of the middle of the ORMC transmitter pads, being the peaks in the middle of those pads, corresponding to the higher point of L_{12} . With the increase of d_{pad} , Fig. 6.8, the peaks of the curves tend to decrease, due to the

6.2. RESULTS

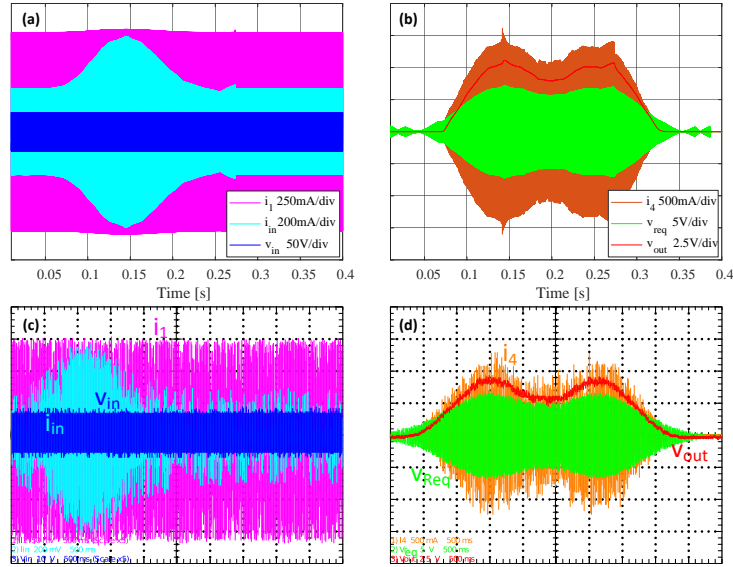


Figure 6.6: Dynamic results for a load of $7,2 \Omega$ with a d_{pad} of 500 mm and at $1,6 \text{ km/h}$. *a*) & *c*) shows v_{in} [50V/div], i_{in} [200mA/div], i_1 [250mA/div] in blue, cyan and pink, respectively. *b* & *d*) shows i_4 [500mA/div], v_{Req} [5V/div] and v_{out} [2.5V/div] in orange, green and red, respectively.

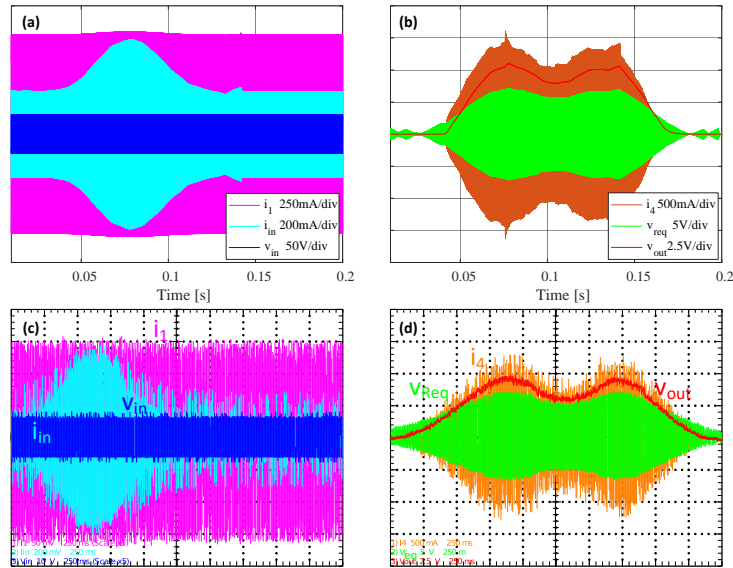


Figure 6.7: Dynamic results for a load of $7,2 \Omega$ with a d_{pad} of 500 mm and at $3,2 \text{ km/h}$. *a*) & *c*) shows v_{in} [50V/div], i_{in} [200mA/div], i_1 [250mA/div] in blue, cyan and pink, respectively. *b* & *d*) shows i_4 [500mA/div], v_{Req} [5V/div] and v_{out} [2.5V/div] in orange, green and red, respectively.

contribution of the other pad being smaller or null. It is notable that this effect only happen for smaller d_{pad} , being the peaks independent of the d_{pad} from the point where the other ORMC transmitter pads do not influence the ORMC receiver. With the increase of the velocity, Fig. 6.7, the curves maintain the same behaviour, just compacted to the new timeframe. Comparing the energy transferred, it was measured a higher transference

6. EXPERIMENTAL VALIDATION

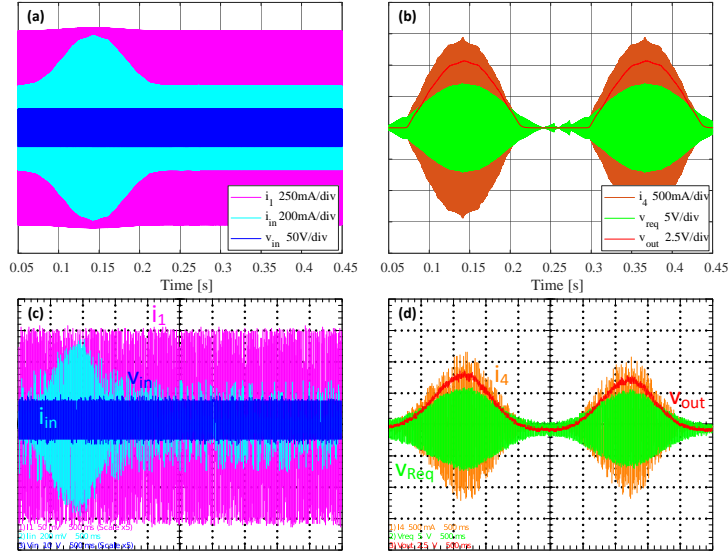


Figure 6.8: Dynamic results for a load of $7,2 \Omega$ with a d_{pad} of 1000 mm and at $1,6 \text{ km/h}$. *a*) & *c*) shows v_{in} [50V/div], i_{in} [200mA/div], i_1 [250mA/div] in blue, cyan and pink, respectively. *b* & *d*) shows i_4 [500mA/div], v_{Req} [5V/div] and v_{out} [2.5V/div] in orange, green and red, respectively.

for a higher velocity, contradicting the expected results. It is notable that in Fig. 6.6 d), the power delivered to the load, represented at red, spends more time at zero than in Fig. 6.7 d). This could be a consequence of the selected timeframe. Since it's an average of the power, all the instances on the oscilloscope screen will contribute to this calculation. The inconsistency in velocity could also contribute to this difference.

To analyse the energy transferred, a scenario was considered where the car passes through 100 km . The energy transferred was $65,51 \text{ Wh}/100\text{km}$ for a d_{pad} of 500 mm and a velocity of $1,6 \text{ km/h}$, $32,48 \text{ Wh}/100\text{km}$ for a d_{pad} of 500 mm and a velocity of $3,2 \text{ km/h}$, and $32,9 \text{ Wh}/100\text{km}$ for a d_{pad} of 1000 mm and a velocity of $1,6 \text{ km/h}$, for a total time of $6\text{h}15\text{m}$, $3\text{h}7,5\text{m}$ and $6\text{h}15\text{m}$, respectively. It is notable that, when comparing the two different velocities, the power transferred decreases almost 50% from the 32 to 16 km/h . However, if the values were scaled for the same time frame, the difference was less than 1% . As concluded in Chapter 5, this difference increase with the increase of the d_{pad} . When comparing the variation of the d_{pad} , an increase of 100% , results in a decrease of 50% . That is the result from half of the transmitter pads which interact with the receiver pad for the same time frame. Those results are in line with the simulation of the Chapter 5, and the explanation is valid for these results too. With the collected data, it is perceptible that a lower d_{pad} and lower velocity lead to a higher power transfer. However, this results in a more expensive charging structure and a longer travel duration.

The LCL-S-S topology was the first resonant topology studied and validated that fit the dynamic requirements, specifically for any operation point the current and voltage are limited. However, the experiments presented a low power delivered to the load, and a low voltage gain. The voltage gain is the relation between the voltage at the source and at the load of the system, and it is important due to the finality of those systems to be charging batteries. To charge a battery, a higher level of voltage compared to the rated

6.2. RESULTS

voltage of the battery is required, so a higher voltage gain is important to avoid high voltages at the source. For those reasons, a new set of tests was conducted for different resonant configurations.

The Series-Series-Series double coupling Compensation Topology (S-S-S) is one of the most studied topologies in IPT systems. This topology was considered the best for static operation, however, it not fit for a dynamic operation. It leads to currents on the ORMC transmitter mesh that tend to infinity when there is no coupling between the ORMC transmitter and receiver. This topology was tested solely for the static operation for comparative purposes. During the course of this work, another resonant topology that met dynamic requirements was studied — the Inductor-Capacitor-Capacitor-Series-Series double coupling Compensation Topology (LCC-S-S). The LCC-S-S only uses one more component (a capacitor) than the LCL-S-S topology. The topology maintains the advantages of the LCL-S-S and a similar behaviour. LCC-S-S benefits from a L_s lower than L_1 in terms of power delivered to the load, however, the currents and voltages were higher through all the system. For both topologies, the changes between them and the LCL-S-S were small, only requiring to disassembly of the resonant tank of the ORMC transmitter. The change in the system was simple and the conditions of the system remained the same, except for L_s , C_s , the new capacitor C_1 and the corresponding resistances, r_s , r_{cs} and r_{c1} , on the LCL-S-S topology.

C_2 and C_4 capacitors are given by equations 3.8 and 3.9 respectively, for both topologies. The capacitor C_1 for the S-S-S topology is given by $C_1 = 1/(\omega^2.L_1)$. For the LCC-S-S, C_1 is given by $C_1 = 1/(\omega^2.(L_1 - L_s))$, and C_s is given by $C_s = 1/(\omega^2.L_s)$.

The adaptation of the Matlab[®]/Simulink[®] model was necessary to ensure the safety of the implementation and to compare with the experimental results. The electrical parameters for both resonant topologies are presented in Table. 6.2.

6.2.2 Additional Resonant Topologies

Static Operation

To measure and analyse the static behaviour, the tests conducted for the LCL-S-S were repeated for S-S-S and LCC-S-S under the same conditions, in the S-S-S case, solely for the aligned position. The results for S-S-S are presented in Fig. 6.9 and in Appendix D.6 for experimental and simulation results. The images on the left show the curves of v_{in} , i_{in} , i_1 and i_2 . The images on the right show the curves of v_{in} , i_4 , v_{out} and i_{out} . The same scales were used for the experimental and simulation scopes.

The S-S-S topology from the point of view of the ORMC transmitter, the current ($i_{in} = i_1$) presented a waveform very close to a sinusoidal. Theoretically, this current is dependent on L_{12} and tended to infinity when $L_{12} = 0$. Additionally, it depends on the load, decreased as the load increases. On the wheel side, the current followed the behaviour of i_1 . On the on-board side, the currents are strongly influenced by the load, due to the Ohm's law. By analysing the circuit at the fundamental frequency without the rectifier converter, the load voltage becomes independent of the load, resulting in an inverse proportionality relation between the current and the load. On the practice, that is not proven, due to the introduction of the inverter and the other harmonic frequencies,

6. EXPERIMENTAL VALIDATION

Table 6.2: Electric parameters for S-S-S and LCC-S-S

Parameter	Value	
Topology	S-S-S	LCC-S-S
V_{dc}	30 V	
f_s	$90,1\text{ kHz}$	$84,35\text{ kHz}$
ORMC	$L_1 = 84,97\ \mu\text{H}; r_1 = 0,44\ \Omega$ $L_2 = 77,38\ \mu\text{H}; r_2 = 0,2\ \Omega$ $L_{12} = [0 \rightarrow 9,05]\ \mu\text{H}; k_{12} = [0 \rightarrow 0,11]$	
IRMC	$L_3 = 3,91\ \mu\text{H}; r_3 = 0,48\ \Omega$ $L_4 = 10,37\ \mu\text{H}; r_4 = 0,11\ \Omega$ $L_{34} = 3,06\ \mu\text{H}; k_{34} = 0,48$	
Resonant Components	$C_1 = 38,8\ \text{nF}; r_{c1} = 0,08\ \Omega$ $C_2 = 44,01\ \text{nF}; r_{c2} = 0,10\ \Omega$ $C_4 = 343,43\ \text{nF}; r_{c4} = 0,61\ \Omega$	$L_s = 24,05\ \mu\text{H}; r_{ls} = 0,2\ \Omega$ $C_s = 151,93\ \text{nF}; r_{cs} = 0,06\ \Omega$ $C_1 = 57,99\ \text{nF}; r_{c1} = 0,03\ \Omega$ $C_2 = 44,01\ \text{nF}; r_{c2} = 0,11\ \Omega$ $C_4 = 343,43\ \text{nF}; r_{c4} = 0,61\ \Omega$
C_o	$470\ \mu\text{F}$	
R_o	$2,4\text{ or }7,2\ \Omega$	

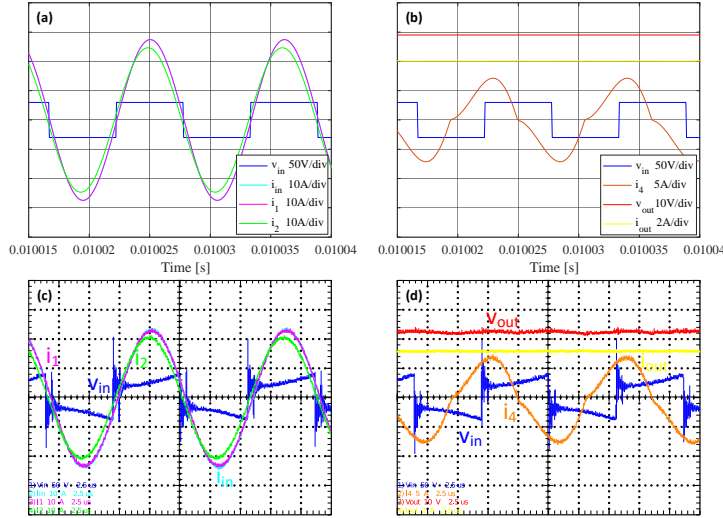


Figure 6.9: Static results for a load of $7,2\ \Omega$ on an aligned situation. *a)* & *c)* shows v_{in} [$50\text{V}/\text{div}$], i_{in} [$10\text{A}/\text{div}$], i_1 [$10\text{A}/\text{div}$] and i_2 [$10\text{A}/\text{div}$] in blue, cyan, pink and green, respectively. *b)* and *d)* v_{in} [$50\text{V}/\text{div}$], i_4 [$5\text{A}/\text{div}$], v_{out} [$10\text{V}/\text{div}$] and i_{out} [$2\text{A}/\text{div}$] in blue, orange, red and yellow, respectively.

but the dependency of the current from the load remains present. The power delivered to the load was of $190,2$ and $117,1\text{ W}$, for a load of $7,2$ and $2,4\ \Omega$, resulting in an increase of $72,05$ and $58,55$ times compared with LCL-S-S. The voltage gain was $0,97$ and $0,562$ for a load of $7,2$ and $2,4\ \Omega$, resulting in an increase of $6,93$ and $8,03$ times compared with LCL-S-S, respectively. The experimental results are a little off from the simulation. This could be result off the high dependency of the off-board side to the ORMC reflected load,

6.2. RESULTS

that include the load of the system, the L_{12} , L_{34} , as well the other components on the wheel and on-board sides. This led to a system that was more sensitive to little variations. Additionally, the curve of v_{in} present distortion compared to the simulation, where is a perfect square shape, introducing new harmonic frequencies.

The results for the LCC-S-S are presented in Fig. 6.10 and 6.11 and in Appendix D.7 and D.8, for experimental and simulation results. The images on the left show the curves of v_{in} , i_{in} , i_1 and i_2 . The images on the right show the curves of v_{in} , i_4 , v_{out} and i_{out} . The same scales were used for the experimental and simulation scopes.

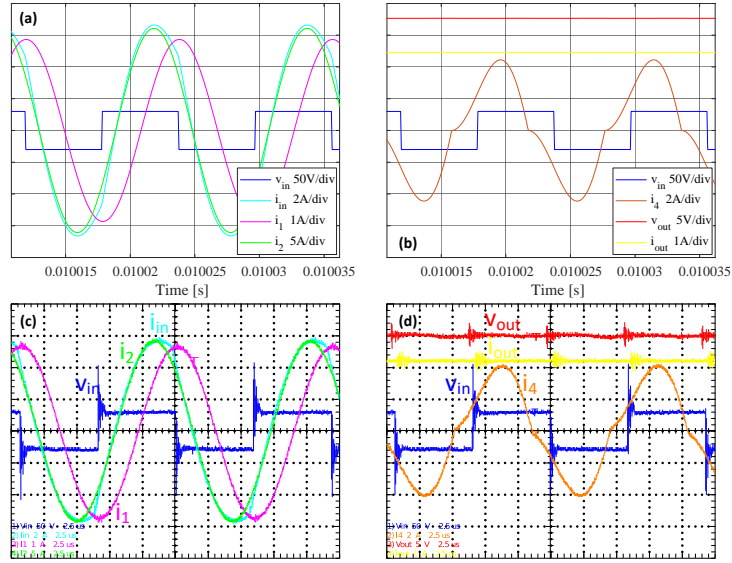


Figure 6.10: Static results for a load of $7,2 \Omega$ on an aligned situation. *a*) & *c*) shows v_{in} [50V/div], i_{in} [2A/div], i_1 [1A/div] and i_2 [5A/div] in blue, cyan, pink and green, respectively. *b*) and *d*) v_{in} [50V/div], i_4 [2A/div], v_{out} [5V/div] and i_{out} [1A/div] in blue, orange, red and yellow, respectively.

From the standpoint of the off-board side, the i_{in} maintains the behaviour of change the amplitude in function of L_{12} . Additionally, when compared to the LCL-S-S, the curves present a more smooth shape, being more close to a sinusoid on the coupled situation. The i_1 is now dependent of the load and the L_{12} , decreasing for higher L_{12} . On the wheel and the on-board side the behaviour remains the same, however, the peaks are higher, increasing the power delivered to the load. The power delivered to the load was of 43,07 and 34,89 W for a load of 7,2 and 2,4 Ω . This is a big increase compared to LCL-S-S (18 and 17,5 times respectively), however, is faraway from the values presented on S-S-S (a decrease of 0,5 and 0,31 times). Yet, compared with the S-S-S, this topology presents lower power delivered by the source, leading eventually to higher efficiencies. The voltage gain is of 0,59 and 0,31 for a load of 7,2 and 2,4 Ω , respectively. This represents an increase compared to LCL-S-S of 4,21 and 4,43 times, however a decrease of 0,61 and 0,55 times compared to S-S-S. To this system, for an static application, the S-S-S is the better topology, with higher power delivered to the load and voltage gain. The LCC-S-S presents a big upgrade to the LCL-S-S.

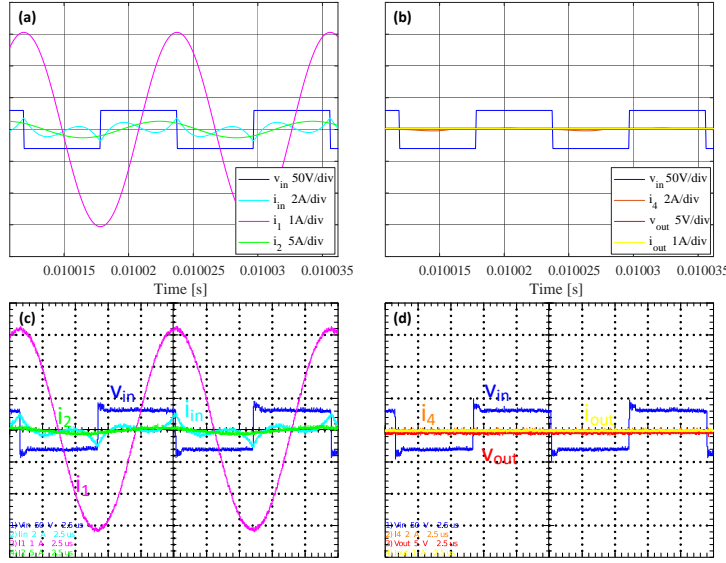


Figure 6.11: Static results for a load of $7,2 \Omega$ on an decoupled situation. *a)* & *c)* shows v_{in} [50V/div], i_{in} [2A/div], i_1 [1A/div] and i_2 [5A/div] in blue, cyan, pink and green, respectively. *b)* and *d)* v_{in} [50V/div], i_4 [2A/div], v_{out} [5V/div] and i_{out} [1A/div] in blue, orange, red and yellow, respectively.

Dynamic Operation

The dynamic test was conducted for the LCC-S-S topology and the tests of the LCL-S-S were repeated. The results of simulation and experimental are presented on Fig. 6.12, 6.13 and 6.14 on the bottom and top side, respectively. The images on the left show the curves of v_{in} , i_{in} , and i_1 of the first transmitter pad. The images on the right show the curves of i_4 , v_{Req} , v_{out} and i_{out} . The same scales were used for the experimental and simulation scopes.

It is notable that for every parameter measured for any point, there was an increase compared to LCL-S-S, except, the fixed value v_{in} that remains the same. From the perspective of the off-board side, the main difference lies in the lost of independency from the load and L_{12} but maintains the applicability on a dynamic operation. On the wheel and on-board side, the behaviour remains similar compared to LCL-S-S, where the currents and voltage are dependent on the L_{12} , however with higher values. The behaviour of the system with the increase of d_{pad} is similar to the LCL-S-S topology, where the maximum points decrease. Comparing the energy transferred for different velocities it was measured higher transference for a higher velocity, once more, contradicting the simulation results. The reasons that could lead to these results are already present in Section 6.2.1.

To analyse the energy transferred, a scenario where the car passing through 100 km was taken. The energy transferred was $259,3 Wh/100km$ for a d_{pad} of 500 mm and a velocity of 16 km/h, $119,17 Wh/100km$ for a d_{pad} of 500 mm and a velocity of 3,2 km/h, and $109,6 Wh/100km$ for a d_{pad} of 1000 mm and a velocity of 1,6 km/h, for a total time of 6h15m, 3h7,5m and 6h15m, respectively. The impact of the velocity and d_{pad} remain independent of the resonant topology used, maintain a similar analysis with the LCL-S-S.

6.2. RESULTS

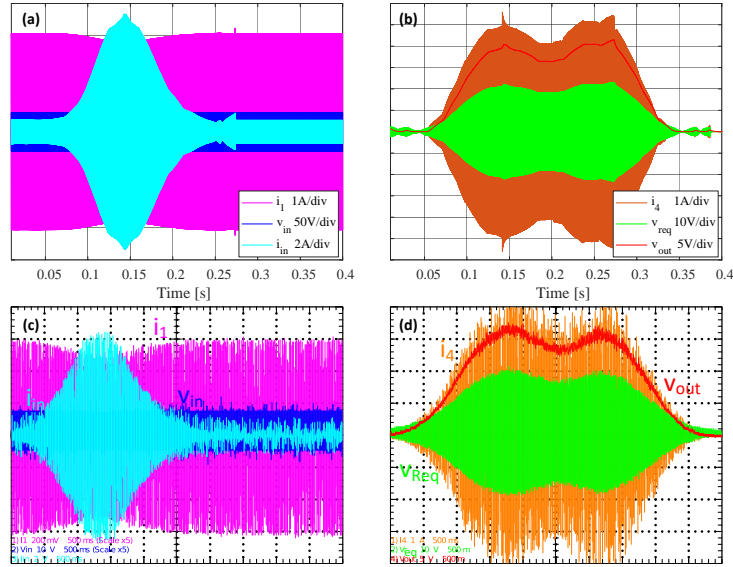


Figure 6.12: Dynamic results for a load of $7,2 \Omega$ with a d_{pad} of 500 mm at $1,6 \text{ km/h}$. *a*) & *c*) shows v_{in} [50V/div], i_{in} [2A/div], i_1 [1mA/div] in blue, cyan and pink, respectively. *b*) & *d*) shows i_4 [1A/div], v_{Req} [10V/div] and v_{out} [5V/div] in orange, green and red, respectively.

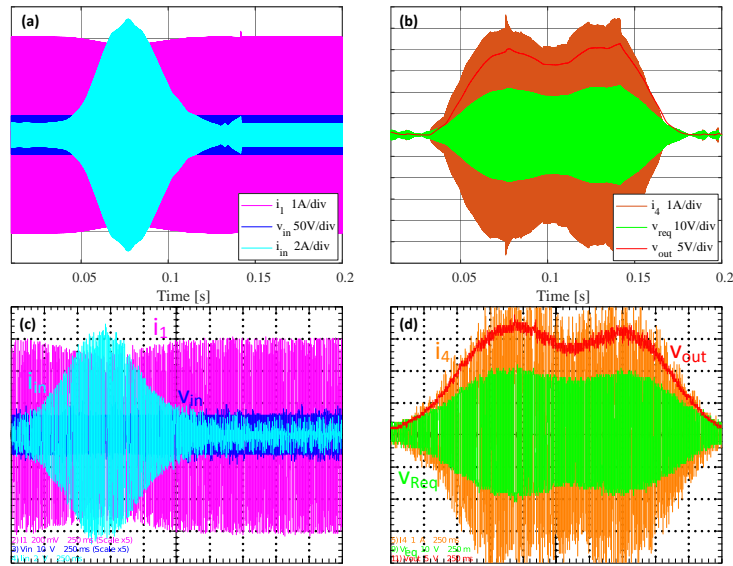


Figure 6.13: Dynamic results for a load of $7,2 \Omega$ with a d_{pad} of 500 mm at $3,2 \text{ km/h}$. *a*) & *c*) shows v_{in} [50V/div], i_{in} [2A/div], i_1 [1mA/div] in blue, cyan and pink, respectively. *b*) & *d*) shows i_4 [1A/div], v_{Req} [10V/div] and v_{out} [5V/div] in orange, green and red, respectively.

It was notable, a decreasing of 46% with the increase of the velocity, and a decrease of 42,3% with the increase of d_{pad} . The power delivered to the load compared with the LCL-S-S was much higher, with an increase of 3 to 4 times, for every situation. This represents a good alternative for a dynamic operation, with a higher versatility in the ORMC transmitter resonant tank.

6. EXPERIMENTAL VALIDATION

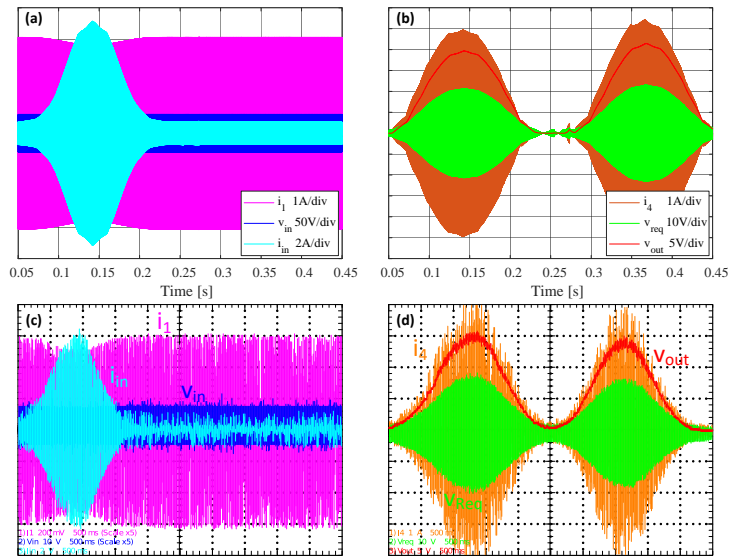


Figure 6.14: Dynamic results for a load of $7,2 \Omega$ with a d_{pad} of 1000 mm at $1,6 \text{ km/h}$. *a*) & *c*) shows v_{in} [50V/div], i_{in} [2A/div], i_1 [1mA/div] in blue, cyan and pink, respectively. *b*) & *d*) shows i_4 [1A/div], v_{Req} [10V/div] and v_{out} [5V/div] in orange, green and red, respectively.

7 Conclusion

This master's thesis aimed to prove the concept of the inWIPT system for a dynamic operation. From the developed study, it was possible to confirm the applicability on dynamic operation, depending on certain aspects, mainly the resonant topology. Beside the resonant topologies, others components (pad geometries, core placement, air gap, etc.) and the relation between them are directly responsible to influence the system performance.

The electromagnetic characterization study provided insights into the influence of physical variations, specifically on the ferromagnetic cores and the coil cable displacement. This is an important data to achieve the required magnetic parameters on a system. It is anticipated that the observed behaviour will remain, regardless of the dimensions or environments. However, others new aspects can have a heavier influence on the component, potentially leading to unexpected outcomes.

The combination of the simulation model and the real scale prototype proved to be valuable tools for studying, developing, and demonstrating the system capabilities. The simulation, being a faster and more convenient tool, is ideal for conducting new proposals and scaling up experiments. The prototype serves as a physical validation of the system.

The experimental analysis led to a comparison between resonant topologies. It was observed that a significant improvement could be achieved by merely swapping the resonant tank of the first mesh to LCC-S-S. This highlights the substantial impact of a single component on the system. Additionally, the impact of the velocity and the distance between ORMC transmitter pads was studied. This results in a perception where a system benefits from a lower velocity and a lower distance between ORMC transmitter pads. However, this will result in a more expensive charging infrastructure and increased travel time.

Future work:

- Study and characterization of different pad geometries, such as BPP.
- Implementation of variable self-inductances on the Matlab[®]/Simulink[®] model to bring it closer to reality, and optimizing model.
- Introduction of a traction system on the prototype to enable controllable velocity.
- Integration of a battery pack in the prototype.
- Assessment of the EMI.
- Determination of the optimal d_{pad} and car velocity.

Bibliography

- [1] IEA(2023). (2023) Global ev data explore. [Online]. Available: <https://www.iea.org/data-and-statistics/data-tools/global-ev-data-explorer>
- [2] C. T. Rim and C. Mi, *Wireless Power Transfer for Electric Vehicles and Mobile Devices*. Wiley-IEEE Press, 2017.
- [3] V. V, R. M, K. V, S. P. C, and P. M, “Review on selection of battery packs for pure electric vehicles and technical comparison of battery packs,” in *2021 Innovations in Power and Advanced Computing Technologies (i-PACT)*, 2021, pp. 1–6.
- [4] IEA. (2022, May) Global ev outlook 2022. [Online]. Available: <https://www.iea.org/data-and-statistics/charts/evolution-of-average-range-of-electric-vehicles-by-powertrain-2010-2021>
- [5] IEA(2023). (2023) Global ev outlook 2023. [Online]. Available: <https://www.iea.org/reports/global-ev-outlook-2023>
- [6] ACEA. (2022, Mar) Global ev data explore. [Online]. Available: <https://www.acea.auto/publication/european-electric-vehicle-charging-infrastructure-masterplan/>
- [7] S. P and N. G.K, “Review of battery charging methods for electric vehicle,” in *2022 IEEE International Conference on Signal Processing, Informatics, Communication and Energy Systems (SPICES)*, vol. 1, 2022, pp. 395–400.
- [8] A. Khaligh and S. Dusmez, “Comprehensive topological analysis of conductive and inductive charging solutions for plug-in electric vehicles,” *IEEE Transactions on Vehicular Technology*, vol. 61, no. 8, pp. 3475–3489, 2012.
- [9] J. Dai and D. C. Ludois, “A survey of wireless power transfer and a critical comparison of inductive and capacitive coupling for small gap applications,” *IEEE Transactions on Power Electronics*, vol. 30, no. 11, pp. 6017–6029, 2015.
- [10] E. G. Marques, “Mitigate the effect of coupling factor variations in inductive power transfer systems,” 2014.
- [11] B. H. Choi, E. S. Lee, Y. H. Sohn, G. C. Jang, and C. T. Rim, “Six degrees of freedom mobile inductive power transfer by crossed dipole tx and rx coils,” *IEEE Transactions on Power Electronics*, vol. 31, no. 4, pp. 3252–3272, 2016.
- [12] A. Kumar, S. Pervaiz, C.-K. Chang, S. Korhummel, Z. Popovic, and K. K. Afridi, “Investigation of power transfer density enhancement in large air-gap capacitive wireless power transfer systems,” in *2015 IEEE Wireless Power Transfer Conference (WPTC)*, 2015, pp. 1–4.
- [13] IT. (2022, Dez) Project: inwheel inductive power charging for sustainable mobility. [Online]. Available: <https://www.it.pt/Projects/Index/4849>
- [14] D. J. Griffiths, *Introduction to Electrodynamics*. Cambridge University Press, 1981.
- [15] E. G. Marques, *Transferência de Energia sem contactos para cargas de Baterias de Veículos Eléctricos*, 2014.

BIBLIOGRAPHY

- [16] V. S. Costa, E. Marques, A. P. Mendes, M. S. Perdigao, and A. M. S. Mendes, “Magnetic couplers for dynamic ipt systems,” in *2019 IEEE Vehicle Power and Propulsion Conference (VPPC)*, 2019, pp. 1–6.
- [17] E. G. Marques, V. S. Costa, A. M. S. Mendes, and M. S. Perdigão, “Inductive power transfer in electric vehicles: Past and future trends,” *IEEE Vehicular Technology Magazine*, vol. 18, no. 4, pp. 111–122, 2023.
- [18] A. P. Mendes, “Wireless power transfer system for continuous charging of electric vehicles,” 2017.
- [19] Z. H. Shi and Z. C. Qiu, “Design considerations of coils used in wireless charger for ev,” in *2018 IEEE International Conference on Applied Superconductivity and Electromagnetic Devices (ASEMD)*, 2018, pp. 1–2.
- [20] D. Lin, C. Zhang, and S. Y. R. Hui, “Mathematic analysis of omnidirectional wireless power transfer—part-ii three-dimensional systems,” *IEEE Transactions on Power Electronics*, vol. 32, no. 1, pp. 613–624, 2017.
- [21] M. Chigira, Y. Nagatsuka, Y. Kaneko, S. Abe, T. Yasuda, and A. Suzuki, “Small-size light-weight transformer with new core structure for contactless electric vehicle power transfer system,” in *2011 IEEE Energy Conversion Congress and Exposition*, 2011, pp. 260–266.
- [22] E. G. Marques and A. M. S. Mendes, “Optimization of transmitter magnetic structures for roadway applications,” in *2017 IEEE Applied Power Electronics Conference and Exposition (APEC)*, 2017, pp. 959–965.
- [23] S. Chapman, *Electrical Machinery Fundamentals*. McGraw Hill, 2011.
- [24] E. G. Marques, V. S. Costa, M. Torres, B. Rios, A. Mendes, and M. S. Perdigão, “Double coupling ipt systems for ev charging applications,” in *2021 IEEE Vehicle Power and Propulsion Conference (VPPC)*, 2021, pp. 1–6.
- [25] C. Panchal, S. Stegen, and J. Lu, “Review of static and dynamic wireless electric vehicle charging system,” *Engineering Science and Technology, an International Journal*, vol. 21, no. 5, pp. 922–937, 2018. [Online]. Available: <https://www.sciencedirect.com/science/article/pii/S221509861830154X>
- [26] D.-W. Seo, “Comparative analysis of two- and three-coil wpt systems based on transmission efficiency,” *IEEE Access*, vol. 7, pp. 151 962–151 970, 2019.
- [27] G. R. Nagendra, J. T. Boys, G. A. Covic, B. S. Riar, and A. Sondhi, “Design of a double coupled ipt ev highway,” in *IECON 2013 - 39th Annual Conference of the IEEE Industrial Electronics Society*, 2013, pp. 4606–4611.
- [28] D. M. Niculae, M. Stanculescu, S. Deleanu, M. Iordache, and L. Bobaru, “Wireless power transfer systems optimization using multiple magnetic couplings,” *Electronics*, vol. 10, no. 20, 2021. [Online]. Available: <https://www.mdpi.com/2079-9292/10/20/2463>
- [29] E. G. Marques, V. S. Costa, M. S. Perdigão, and A. M. S. Mendes, “Double coupling in-wheel ipt system for electric vehicles,” *IEEE Transactions on Vehicular Technology*, vol. 72, no. 10, pp. 12 757–12 769, 2023.

- [30] V. S. Costa, E. G. Marques, M. Torres, A. M. S. Mendes, and M. S. Perdigão, “Double coupling in-wheel dynamic ipt for ev charging,” in *2023 IEEE Energy Conversion Congress and Exposition (ECCE)*, 2023, pp. 1725–1730.
- [31] E. G. Marques, *Mitigate the Effect of Coupling Factor Variations in Inductive Power Transfer Systems*, 2023.
- [32] D. Xin, L. Weiyi, L. Yanling, S. Yugang, T. Chunsen, W. Zhihui, and S. Yue, “Improved lcl resonant network for inductive power transfer system,” in *2015 IEEE PELS Workshop on Emerging Technologies: Wireless Power (2015 WoW)*, 2015, pp. 1–5.
- [33] D. D. Hugo Lourenço, “Desenvolvimento de um protótipo para carregamento contínuo em veículos elétricos: a estrutura magnética,” 2020.
- [34] D. Dankov, “Modelling of an inductive power transfer system,” in *2020 XI National Conference with International Participation (ELECTRONICA)*, 2020, pp. 1–5.
- [35] V. Z. Barsari, D. J. Thrimawithana, G. A. Covic, and S. Kim, “A switchable inductively coupled connector for ipt roadway applications,” in *2020 IEEE PELS Workshop on Emerging Technologies: Wireless Power Transfer (WoW)*, 2020, pp. 35–39.
- [36] D. Bui, Q. Zhu, L. Zhao, and A. P. Hu, “Concentric-coil hybrid ipt system with improved tolerance to coupling and load variations,” *IEEE Journal of Emerging and Selected Topics in Power Electronics*, vol. 10, no. 4, pp. 4913–4922, 2022.
- [37] F. Xu, S.-C. Wong, and C. K. Tse, “Inductive power transfer system with maximum efficiency tracking control and real-time mutual inductance estimation,” *IEEE Transactions on Power Electronics*, vol. 37, no. 5, pp. 6156–6167, 2022.
- [38] E. Britannica, “skin effect,” *Britannica, The Editors of Encyclopaedia*, 2008. [Online]. Available: <https://www.britannica.com/science/skin-effect>

A Prototype Model Specifications

On the prototype, two thickness of MDF were used: 10 millimetres for the road (mdf_{t_1}), ORMC transmitter structure and the slats, and 19 millimetres (mdf_{t_2}) for the rings and for the pieces to fix it. On figure A.1, the MDF material is coloured white, the wires coloured orange, the wheel the tire coloured black and the rim in light grey and the trailer coloured in brown and grey. The dimensions of the prototype are summarized in table A.1. The components are represented and dimensions labelled in Fig. 4.3, 4.6 and A.1.

Table A.1: Experimental setup specifications

Parameter	Value	Parameter	Value
IRMC: SP-SP		ORMC transmitter: DDP	
d_{L3} ($g_{34a} = 15 \text{ mm}$)	364 mm	$Coil_l$	280 mm
d_{L4} ($g_{34a} = 15 \text{ mm}$)	322 mm	$Coil_w$	390 mm
d_{L3} ($g_{34b} = 10 \text{ mm}$)	359 mm	$Coil_{lint}$	115 mm
d_{L4} ($g_{34b} = 10 \text{ mm}$)	327 mm	$Coil_{wint}$	220 mm
ORMC receiver: SP		$Coil_{lintcomb}$	395 mm
d_{L2}	540 mm		
Structure			
$Slat_l$	2400 mm	$Slat_w$	20 mm
$Road_l$	2400 mm	$Road_w$	600 mm
T_i	600 mm	T_w	480 mm
d_{r1i}	476 mm	d_{r1o}	596 mm
d_{r2i}	476 mm	d_{r2o}	666 mm
$Piece_l$	208 mm	$Piece_w$	50 mm
$Trailer_{tl}$	1250 mm	$Trailer_{tw}$	1300 mm
$Trailer_l$	1000 mm	$Trailer_w$	560 mm
d_{Wheel}	496 mm	d_{Litz}	5 mm

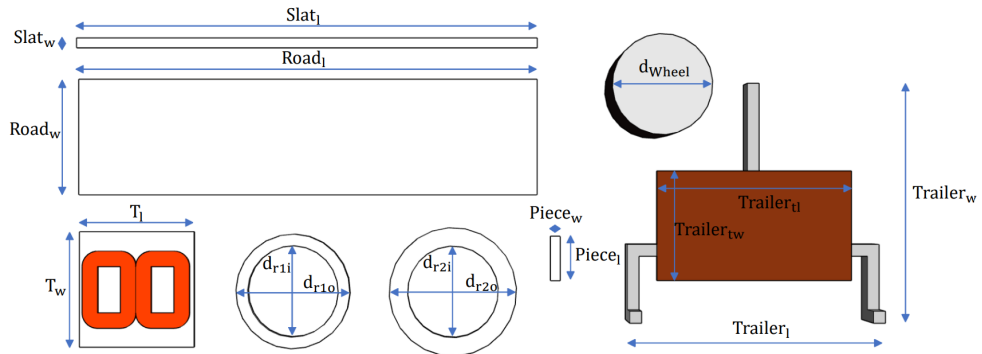


Figure A.1: Structure components.

B Detailed Results from Chapter 4

Through this appendix will be used as convention the structure presented in B.1. On the caption, the following information is presented: prototype structure (wood or aluminium), air-gap, pad geometries, number of turns of each pad, and number and volume of ferrites. PG stands for Pad Geometry, however, the majority of the test are realized only with one of the MC, so in those cases only will be present two PG. The N_x next to PG are the number of turns of the geometry implemented. F_x are the number of ferrites and t the volume implemented. t can take on two volume values: s with 43x24x4 and b with 93x28x16 mm.

Table B.1: Table structure example

Material Structure - AG - PG(N_1)+PG(N_2) : PG(N_3)+PG(N_4) - $F_1+F_2(t)$: $F_3+F_4(t)$								
Variable	L_x	L_y	L_{t+}	L_{t-}	M_+	M_-	k_+	k_-
$Variable_1$	$Value_{11}$	$Value_{12}$	$Value_{13}$	$Value_{14}$	$Value_{15}$	$Value_{16}$	$Value_{17}$	$Value_{18}$
$Variable_2$	$Value_{21}$	$Value_{22}$	$Value_{23}$	$Value_{24}$	$Value_{25}$	$Value_{26}$	$Value_{27}$	$Value_{28}$
				...				
$Variable_n$	$Value_{n1}$	$Value_{n2}$	$Value_{n3}$	$Value_{n4}$	$Value_{n5}$	$Value_{n6}$	$Value_{n7}$	$Value_{n8}$

B.1 Dependency between ORMC and IRMC

This test involved the electromagnetic characterization of IRMC without the ORMC and with ORMC mounted.

Table B.2: Coupling with ORMC vs whitout ORMC

Aluminium Structure - 10 mm - DDP(3+3)+SP(3) : SP(6)+SP(6) - 0+12(s) : 12+12(s)								
MC	L_3	L_4	L_{t+}	L_{t-}	M_+	M_-	k_+	k_-
IRMC	14,74	14,22	39,05	18,58	5,045	5,19	0,348	0,358
IRMC + ORMC	14,77	14,18	39,19	18,22	5,12	5,365	0,354	0,371

Another test to confirm the decoupling between MC's was the electromagnetic characterization between ORMC receiver and IRMC transmitter (table B.3).

B.2. IRMC

Table B.3: Couple between ORMC receiver and IRMC transmitter

Aluminium Structure - 10 mm - DDP(3+3)+SP(3) SP(6)+SP(6) - 12+12(s)							
L_3	L_4	L_{t+}	L_{t-}	M_+	M_-	k_+	k_-
15,31	14,75	30,61	29,18	0,275	0,44	0,018	0,029

B.2 IRMC

B.2.1 Impact of rotation between transmitter and receiver

Measures were conducted to evaluate the impact of the rotation between the transmitter (L_3) and the receiver (L_4) at three distinct positions (0, 120 and 240 degrees).

Table B.4: Relative position between transmitter and receiver

Aluminium Structure - 10 mm - SP(6)+SP(6) - 12+12(s)								
Degree	L_3	L_4	L_{t+}	L_{t-}	M_+	M_-	k_+	k_-
0 ^o	14,55	14,14	38,88	18,6	5,095	5,045	0,355	0,352
120 ^o	14,54	14,16	38,81	18,65	5,055	5,025	0,352	0,350
240 ^o	14,62	14,14	38,91	18,53	5,075	5,115	0,353	0,356

B.2.2 Impact of the Coil Width/SBT

The test was conducted for three different numbers of coil turns (5,8 and 9). Due to the space constraints of the support pieces, the data presented in Table. B.5 were chosen to be analysed on Section 4.3.1 based on their higher number of sample points.

Table B.5: Magnetic parameters in function of SBT

Wood Structure - 15 mm - SP(5)+SP(5) - 0+0								
SBT (mm)	L_3	L_4	L_{t+}	L_{t-}	M_+	M_-	k_+	k_-
2	23,88	20,01	67,94	18,92	12,025	12,485	0,55	0,571
9	19,88	16,9	59,21	15,93	11,215	10,425	0,612	0,569
18	18,35	15,13	54,01	15,12	10,265	9,18	0,616	0,551
27	17,99	13,53	50,2	14,51	9,34	8,505	0,599	0,545
36	16,96	11,61	45,12	14,69	8,275	6,94	0,59	0,495

Table B.6: Magnetic parameters in function of SBT

Wood Structure - 15 mm - SP(8)+SP(8) - 0+0								
SBT (mm)	L_3	L_4	L_{t+}	L_{t-}	M_+	M_-	k_+	k_-
2	56,21	43,03	155,4	42,11	28,08	28,57	0,571	0,581
9	45,64	34,87	126,3	35,11	22,895	22,7	0,574	0,569

Table B.7: Magnetic parameters in function of SBT

Wood Structure - 15 mm - SP(10)+SP(10) - 0+0								
SBT (mm)	L_3	L_4	L_{t+}	L_{t-}	M_+	M_-	k_+	k_-
2	65,99	56,17	204,01	44,08	40,925	39,04	0,672	0,641
9	56,57	44,1	167,7	35,84	33,515	32,415	0,671	0,649

B.2.3 Impact of the number of turn in each coil

This test was conducted for two different air-gaps (10 and 15 mm) and for two ferrites volumes for each air-gap, resulting in a total of four trials. Thus, the impact of the air-gap and the volume of ferrites was also analysed.

Table B.8: Magnetic parameters in function of number of turns in each coil

Aluminium Structure - 10 mm - SP(n)+SP(n) - 12+12(s)								
Number of turns (n)	L_3	L_4	L_{t+}	L_{t-}	M_+	M_-	k_+	k_-
2	17,16	20,75	40,11	35,19	1,1	1,36	0,058	0,072
4	19,29	22,38	48,82	33,77	3,575	3,95	0,172	0,19
6	21,15	25,37	59,68	33,39	6,58	6,565	0,284	0,283
8	22,55	26,66	66,95	31,51	8,87	8,85	0,362	0,361
10	23,95	28,35	73,39	30,53	10,545	10,885	0,405	0,418

Table B.9: Magnetic parameters in function of number of turns in each coil

Aluminium Structure - 15 mm - SP(n)+SP(n) - 12+12(s)								
Number of turns (n)	L_3	L_4	L_{t+}	L_{t-}	M_+	M_-	k_+	k_-
2	16,74	20,43	38,63	35,7	0,73	0,735	0,04	0,04
4	18,57	22,75	46,65	35,6	2,665	2,86	0,13	0,139
6	20,75	25,28	56,02	36,14	4,995	4,945	0,218	0,216
8	22,15	26,69	62,63	34,83	6,895	7,005	0,284	0,288
10	23	27,49	66,15	33	7,83	8,745	0,311	0,348

B.3. ORMC

Table B.10: Magnetic parameters in function of number of turns in each coil

Aluminium Structure - 10 mm - SP(n)+SP(n) - 24+24(s)								
Number of turns (n)	L_3	L_4	L_{t+}	L_{t-}	M_+	M_-	k_+	k_-
2	18,26	22,26	45,2	35,05	2,34	2,735	0,116	0,136
4	23,63	26,72	64	35,27	6,825	7,54	0,272	0,3
6	30,19	33,82	92,97	35,37	14,48	14,32	0,453	0,448
8	37,09	41,48	123,1	34,76	22,265	21,905	0,568	0,558
10	43,05	48,56	149,2	34,58	28,795	28,515	0,63	0,624

Table B.11: Magnetic parameters in function of number of turns in each coil

Aluminium Structure - 15 mm - SP(n)+SP(n) - 24+24(s)								
Number of turns (n)	L_3	L_4	L_{t+}	L_{t-}	M_+	M_-	k_+	k_-
2	18,11	22,1	43,31	35,92	1,55	2,145	0,077	0,107
4	22,93	27,02	63,87	36,45	6,96	6,75	0,28	0,271
6	29,73	33,88	89,44	37,63	12,915	12,99	0,407	0,409
8	36,84	41,38	118,1	39,75	19,94	19,235	0,511	0,493
10	43,86	48,26	142,3	38,79	25,09	26,665	0,545	0,58

B.3 ORMC

B.3.1 Impact of the wheel entry angle and the misalignment on y axis for DDP-SP

The test consist of the measurement of the magnetic parameters for different angles of the wheel (from -60 to 60 degrees) with the transmitter pad static. The test was conducted for two core widths ($core_w$) (93 and 186mm) and three misalignments on y axis: 0 mm, where the pads are aligned, -50 mm and 50 mm.

Table B.12: Magnetic parameters in function of the wheel's rotation angle with lateral displacement of 0 mm

Aluminium Structure - 20 mm - DDP(10+10)+SP(8) - 24+24(b)								
Wheel's rotation ($^{\circ}$)	L_3	L_4	L_{t+}	L_{t-}	M_+	M_-	k_+	k_-
-60	86,39	82,95	196	141,7	13,33	13,82	0,157	0,163
-52,5	86,57	83,03	196,3	141,6	13,35	14	0,157	0,165
-45	86,84	83,11	197	141,5	13,525	14,225	0,159	0,167
-37,5	86,75	83,21	196,9	141,6	13,47	14,18	0,159	0,167
-30	86,61	83,3	196,6	141,5	13,345	14,205	0,157	0,167
-22,5	86,93	83,34	197,1	141,5	13,415	14,385	0,158	0,169
-15	87,16	83,36	197,7	141,4	13,59	14,56	0,159	0,171
-7,5	87,06	83,32	197,5	141,2	13,56	14,59	0,159	0,171
0	86,72	83,25	196,9	140,9	13,465	14,535	0,158	0,171
7,5	86,87	83,18	197,2	140,7	13,575	14,675	0,16	0,173
15	87,23	83,11	198	140,6	13,83	14,87	0,162	0,175
22,5	87,22	83,03	197,9	140,6	13,825	14,825	0,162	0,174
30	87,06	82,98	197,5	140,7	13,73	14,67	0,162	0,173
37,5	87,2	82,98	197,8	140,9	13,81	14,64	0,162	0,172
45	87,29	82,85	197,8	140,8	13,83	14,67	0,163	0,173
52,5	86,8	82,72	196,9	140,7	13,69	14,41	0,162	0,17
60	86,35	82,73	196,1	140,7	13,51	14,19	0,16	0,168

B.3. ORMC

Table B.13: Magnetic parameters in function of the wheel's rotation angle with lateral displacement of 50 mm

Aluminium Structure - 20 mm - DDP(10+10)+SP(8) - 24+24(b)								
Wheel's rotation ($^{\circ}$)	L_3	L_4	L_{t+}	L_{t-}	M_+	M_-	k_+	k_-
-60	83,32	83,12	189,7	142,5	11,63	11,97	0,14	0,144
-52,5	83,48	83,14	190	142,4	11,69	12,11	0,14	0,145
-45	83,71	83,16	190,6	142,2	11,865	12,335	0,142	0,148
-37,5	83,6	83,2	190,6	142	11,9	12,4	0,143	0,149
-30	83,52	83,27	190,5	141,9	11,855	12,445	0,142	0,149
-22,5	83,71	83,3	190,8	141,8	11,895	12,605	0,142	0,151
-15	83,92	83,3	191,1	141,8	11,94	12,71	0,143	0,152
-7,5	83,83	83,25	191	142	11,96	12,54	0,143	0,15
0	83,61	83,18	190,5	141,9	11,855	12,445	0,142	0,149
7,5	83,73	83,12	190,8	141,8	11,975	12,525	0,144	0,15
15	84,01	83,04	191,1	141,8	12,025	12,625	0,144	0,151
22,5	83,96	83	190,9	141,9	11,97	12,53	0,143	0,15
30	83,83	82,94	190,5	142	11,865	12,385	0,142	0,149
37,5	83,93	82,94	190,6	142,3	11,865	12,285	0,142	0,147
45	83,96	82,73	190,5	142,4	11,905	12,145	0,143	0,146
52,5	83,62	82,56	189,7	142,4	11,76	11,89	0,142	0,143
60	83,33	82,58	189,3	142,3	11,695	11,805	0,141	0,142

Table B.14: Magnetic parameters in function of the wheel's rotation angle with lateral displacement of -50 mm

Aluminium Structure - 20 mm - DDP(10+10)+SP(8) - 24+24(b)								
Wheel's rotation ($^{\circ}$)	L_3	L_4	L_{t+}	L_{t-}	M_+	M_-	k_+	k_-
-60	82,71	82,86	187,3	144,1	10,865	10,735	0,131	0,13
-52,5	82,81	82,9	187,6	144	10,945	10,855	0,132	0,131
-45	83	82,95	188	144	11,025	10,975	0,133	0,132
-37,5	82,93	82,99	188	144	11,04	10,96	0,133	0,132
-30	82,87	83,02	187,9	144	11,005	10,945	0,133	0,132
-22,5	83,03	83,03	188,2	144	11,07	11,03	0,133	0,133
-15	83,15	83,01	188,5	143,9	11,17	11,13	0,134	0,134
-7,5	83,06	83	188,6	143,8	11,27	11,13	0,136	0,134
0	82,88	83,13	188,6	143,5	11,295	11,255	0,136	0,136
7,5	82,98	83,05	189	143,2	11,485	11,415	0,138	0,138
15	83,17	82,95	189,4	143,1	11,64	11,51	0,14	0,139
22,5	83,17	82,88	189,4	142,9	11,675	11,575	0,141	0,139
30	83,09	82,81	189,3	142,9	11,7	11,5	0,141	0,139
37,5	83,2	82,83	189,4	142,9	11,685	11,565	0,141	0,139
45	83,2	82,66	189,4	142,8	11,77	11,53	0,142	0,139
52,5	82,94	82,49	188,7	142,6	11,635	11,415	0,141	0,138
60	82,65	82,44	188	142,6	11,455	11,245	0,139	0,136

B.3. ORMC

Table B.15: Magnetic parameters in function of the wheel's rotation angle with lateral displacement of 0 mm

Aluminium Structure - 20 mm - DDP(10+10)+SP(8) - 12+12(b)								
Wheel's rotation ($^{\circ}$)	L_3	L_4	L_{t+}	L_{t-}	M_+	M_-	k_+	k_-
-60	82,23	63,31	162,3	126,8	8,38	9,37	0,116	0,13
-52,5	82,29	63,21	162,2	126,8	8,35	9,35	0,116	0,13
-45	82,41	63,12	162,5	126,8	8,485	9,365	0,118	0,13
-37,5	82,39	62,97	162,4	126,9	8,52	9,23	0,118	0,128
-30	82,33	62,84	162,3	126,9	8,565	9,135	0,119	0,127
-22,5	82,43	62,68	162,4	126,9	8,645	9,105	0,12	0,127
-15	82,54	62,51	162,5	126,9	8,725	9,075	0,121	0,126
-7,5	82,46	62,37	162,7	126,8	8,935	9,015	0,125	0,126
0	82,34	62,29	162,5	126,7	8,935	8,965	0,125	0,125
7,5	82,34	62,12	162,1	126,5	8,82	8,98	0,123	0,126
15	82,42	62,04	162	126,4	8,77	9,03	0,123	0,126
22,5	82,35	61,93	162,1	126	8,91	9,14	0,125	0,128
30	82,27	61,76	162,2	125,6	9,085	9,215	0,127	0,129
37,5	82,36	61,61	162,6	125,3	9,315	9,335	0,131	0,131
45	82,42	61,47	162,8	125,2	9,455	9,345	0,133	0,131
52,5	82,31	61,27	162,5	125,1	9,46	9,24	0,133	0,13
60	82,2	60,91	162,3	125,1	9,595	9,005	0,136	0,127

Table B.16: Magnetic parameters in function of the wheel's rotation angle with lateral displacement of 50 mm

Aluminium Structure - 20 mm - DDP(10+10)+SP(8) - 12+12(b)								
Wheel's rotation ($^{\circ}$)	L_3	L_4	L_{t+}	L_{t-}	M_+	M_-	k_+	k_-
-60	79,99	61,19	158	126,2	8,41	7,49	0,12	0,107
-52,5	80,01	61,24	158,1	126,2	8,425	7,525	0,12	0,108
-45	80,07	61,3	158,4	126,1	8,515	7,635	0,122	0,109
-37,5	80,08	61,36	158,5	126	8,53	7,72	0,122	0,11
-30	80,06	61,42	158,5	126	8,51	7,74	0,121	0,11
-22,5	80,1	61,49	158,7	126	8,555	7,795	0,122	0,111
-15	80,17	61,55	158,8	126,1	8,54	7,81	0,122	0,111
-7,5	80,17	61,62	158,7	126,2	8,455	7,795	0,12	0,111
0	80,1	61,66	158,5	126,4	8,37	7,68	0,119	0,109
7,5	80,08	61,73	158,4	126,7	8,295	7,555	0,118	0,107
15	80,09	61,79	158,5	126,8	8,31	7,54	0,118	0,107
22,5	80,07	61,93	158,4	126,4	8,2	7,8	0,116	0,111
30	80,02	61,98	158,5	126,9	8,25	7,55	0,117	0,107
37,5	80,05	62,08	158,8	125,9	8,335	8,115	0,118	0,115
45	80,1	62,22	159,6	125,4	8,64	8,46	0,122	0,12
52,5	80,08	62,38	160,2	124,5	8,87	8,98	0,125	0,127
60	80	62,53	160,6	124,6	9,035	8,965	0,128	0,127

B.3. ORMC

Table B.17: Magnetic parameters in function of the wheel's rotation angle with lateral displacement of -50 mm

Aluminium Structure - 20 mm - DDP(10+10)+SP(8) - 12+12(b)								
Wheel's rotation ($^{\circ}$)	L_3	L_4	L_{t+}	L_{t-}	M_+	M_-	k_+	k_-
-60	80,09	60,77	154,9	127,9	7,02	6,48	0,1	0,093
-52,5	80,12	60,83	154,8	127,8	6,925	6,575	0,099	0,094
-45	80,17	60,85	154,9	127,7	6,94	6,66	0,099	0,095
-37,5	80,15	60,91	154,9	127,6	6,92	6,73	0,099	0,096
-30	80,15	60,95	155	127,6	6,95	6,75	0,099	0,097
-22,5	80,2	61	155,2	127,4	7	6,9	0,1	0,099
-15	80,2	61,01	155,3	127,7	7,045	6,755	0,1	0,097
-7,5	80,18	60,99	155,4	127,6	7,115	6,785	0,102	0,097
0	80,12	60,98	155,4	127,5	7,15	6,8	0,102	0,097
7,5	80,13	60,93	155,6	127,6	7,27	6,73	0,104	0,096
15	80,14	60,92	155,8	127,5	7,37	6,78	0,105	0,097
22,5	80,11	60,92	156,9	127,2	7,935	6,915	0,114	0,099
30	80,09	60,91	156,2	127,1	7,6	6,95	0,109	0,1
37,5	80,12	60,88	156,8	127	7,9	7	0,113	0,1
45	80,11	61	157	126,6	7,945	7,255	0,114	0,104
52,5	80,05	60,99	157,1	126,4	8,03	7,32	0,115	0,105
60	80,01	60,98	157,1	126,4	8,055	7,295	0,115	0,104

B.3.2 Impact of the misalignment in y axis for DDP—SP, with different misalignments.

This subsection presents the results of the self and mutual inductances and coupling factors, for an emulation of the dynamic behaviour of the system. It was considered thirty-one points distributed equally on a length of 1170 mm , and ten misalignments from 0 to 45 mm spaced 5 mm between them.

Table B.18: Magnetic parameters in function of the y misalignment with lateral displacement of 0 mm

Aluminium Structure - 40 mm - DDP(10+10)+SP(8) - 12+12(b)								
x [mm]	L_3 [μH]	L_4 [μH]	L_{t+} [μH]	L_{t-} [μH]	M_+ [μH]	M_- [μH]	k_+	k_-
-58,5	84,27	82,92	165,79	166,45	0,7	0,37	0,0084	0,0044
-54,6	83,97	82,63	166,21	166,19	0,195	0,205	0,0023	0,0025
-50,7	84,42	82,86	166,07	165,89	0,605	0,695	0,0072	0,0083
-46,8	84,17	82,78	166,61	165,55	0,17	0,7	0,0020	0,0084
-42,9	84,08	82,81	167,04	165,09	0,075	0,9	0,0009	0,0108
-39	84,1	82,63	167,71	164,39	0,49	1,17	0,0059	0,0140
-35,1	84,09	82,06	168,27	163,42	1,06	1,365	0,0128	0,0164
-31,2	83,98	82,07	169,14	163,36	1,545	1,345	0,0186	0,0162
-27,3	84,4	82	172,38	160,65	2,99	2,875	0,0359	0,0345
-23,4	84,55	82,24	175,09	158,7	4,15	4,045	0,0498	0,0485
-19,5	85,02	81,95	178,29	156,04	5,66	5,465	0,0678	0,0655
-15,6	85,39	82,03	181	154,42	6,79	6,5	0,0811	0,0777
-11,7	85,56	82,25	183,54	152,93	7,865	7,44	0,0938	0,0887
-7,8	85,85	82,33	185,59	151,36	8,705	8,41	0,1035	0,1000
-3,9	86,09	82,2	186,1	150,28	8,905	9,005	0,1059	0,1070
0	85,99	82,08	186,6	149,85	9,265	9,11	0,1103	0,1084
3,9	85,84	82,34	185,75	151	8,785	8,59	0,1045	0,1022
7,8	85,83	82,41	185,31	151,88	8,535	8,18	0,1015	0,0973
11,7	85,54	82,49	182,75	153,21	7,36	7,41	0,0876	0,0882
15,6	85,03	82,34	180,01	154,96	6,32	6,205	0,0755	0,0742
19,5	84,86	82,2	178,24	156,61	5,59	5,225	0,0670	0,0626
23,4	84,72	82,32	175,14	158,62	4,05	4,21	0,0485	0,0504
27,3	84,54	82,28	172,82	160,49	3	3,165	0,0360	0,0380
31,2	84,48	82,41	170,95	162,81	2,03	2,04	0,0243	0,0244
35,1	84,45	82,58	169,71	163,13	1,34	1,95	0,0160	0,0234
39	84,46	82,48	169,05	163,15	1,055	1,895	0,0126	0,0227
42,9	84,4	82,75	168,38	164,49	0,615	1,33	0,0074	0,0159
46,8	84,39	82,5	167,54	164,75	0,325	1,07	0,0039	0,0128
50,7	84,46	82,83	166,97	164,99	0,16	1,15	0,0019	0,0137
54,6	84,51	82,94	167	165,35	0,225	1,05	0,0027	0,0125
58,5	84,49	83,22	166,96	165,7	0,375	1,005	0,0045	0,0120

B.3. ORMC

Table B.19: Magnetic parameters in function of the y misalignment with lateral displacement of 50 mm

Aluminium Structure - 40 mm - DDP(10+10)+SP(8) - 12+12(b)								
x [mm]	L_3 [μH]	L_4 [μH]	L_{t+} [μH]	L_{t-} [μH]	M_+ [μH]	M_- [μH]	k_+	k_-
-58,5	84,13	82,95	165,86	166,59	0,61	0,245	0,0073	0,0029
-54,6	84,25	82,87	165,98	166,46	0,57	0,33	0,0068	0,0039
-50,7	84,15	82,72	165,71	167,02	0,58	0,075	0,0070	0,0009
-46,8	84,16	82,47	166,1	166,71	0,265	0,04	0,0032	0,0005
-42,9	84,15	82,6	166,57	165,48	0,09	0,635	0,0011	0,0076
-39	84,24	82,32	166,89	165,48	0,165	0,54	0,0020	0,0065
-35,1	84,15	82,27	168,51	163,93	1,045	1,245	0,0126	0,0150
-31,2	84,4	82,25	170,18	162,56	1,765	2,045	0,0212	0,0245
-27,3	84,4	82,19	171,38	161,24	2,395	2,675	0,0288	0,0321
-23,4	84,51	81,92	173,02	159,82	3,295	3,305	0,0396	0,0397
-19,5	84,51	82,14	176,4	156,94	4,875	4,855	0,0585	0,0583
-15,6	84,73	82,21	178,89	154,68	5,975	6,13	0,0716	0,0734
-11,7	84,97	81,98	180,44	153,5	6,745	6,725	0,0808	0,0806
-7,8	85,02	82,02	182,54	152,05	7,75	7,495	0,0928	0,0898
-3,9	85,04	82,16	183,47	150,34	8,135	8,43	0,0973	0,1009
0	85,22	81,93	183,79	150,19	8,32	8,48	0,0996	0,1015
3,9	85,07	82,2	183,41	150,52	8,07	8,375	0,0965	0,1002
7,8	85,04	82,08	181,89	151,99	7,385	7,565	0,0884	0,0905
11,7	84,93	82,05	179,87	153,45	6,445	6,765	0,0772	0,0810
15,6	84,79	82,05	178,14	154,78	5,65	6,03	0,0677	0,0723
19,5	84,66	82,09	176,28	156,64	4,765	5,055	0,0572	0,0606
23,4	84,47	82,35	174,14	159,02	3,66	3,9	0,0439	0,0468
27,3	84,34	82,27	172,21	160,51	2,8	3,05	0,0336	0,0366
31,2	84,37	82,44	170,71	161,9	1,95	2,455	0,0234	0,0294
35,1	84,45	82,3	169,59	162,6	1,42	2,075	0,0170	0,0249
39	84,49	82,45	169,01	163,75	1,035	1,595	0,0124	0,0191
42,9	84,38	82,07	168,09	164,1	0,82	1,175	0,0099	0,0141
46,8	84,32	82,67	167,54	165,06	0,275	0,965	0,0033	0,0116
50,7	84,4	82,78	167,29	165,47	0,055	0,855	0,0007	0,0102
54,6	84,39	82,5	167,17	165,89	0,14	0,5	0,0017	0,0060
58,5	84,4	82,85	166,94	166,02	0,155	0,615	0,0019	0,0074

B. DETAILED RESULTS FROM CHAPTER 4

Table B.20: Magnetic parameters in function of the y misalignment with lateral displacement of 100 mm

Aluminium Structure - 40 mm - DDP(10+10)+SP(8) - 12+12(b)								
x [mm]	L_3 [μH]	L_4 [μH]	L_{t+} [μH]	L_{t-} [μH]	M_+ [μH]	M_- [μH]	k_+	k_-
-58,5	84,12	82,48	166,27	165,5	0,165	0,55	0,0020	0,0070
-54,6	83,99	82,37	165,93	165,59	0,215	0,385	0,0026	0,0046
-50,7	84,16	82,28	165,97	165,9	0,235	0,27	0,0028	0,0032
-46,8	84,1	82,31	166,18	165,62	0,115	0,395	0,0014	0,0047
-42,9	84,06	82,14	166,23	165,27	0,015	0,465	0,0002	0,0056
-39	84,12	82,08	166,83	164,67	0,315	0,765	0,0038	0,0092
-35,1	84,01	82,05	167,7	163,83	0,82	1,115	0,009	0,0134
-31,2	83,93	82,01	168,84	163,08	1,45	1,43	0,0175	0,0172
-27,3	83,94	82,08	169,7	162,35	1,84	1,835	0,0222	0,0221
-23,4	83,8	81,84	170,73	161,07	2,545	2,285	0,0307	0,0276
-19,5	83,66	81,8	171,92	158,97	3,23	3,245	0,0390	0,0392
-15,6	83,47	81,69	172,88	157,59	3,86	3,785	0,0467	0,0458
-11,7	83,26	81,82	173,93	156,26	4,425	4,41	0,0536	0,0534
-7,8	83,11	81,75	174,47	155,49	4,805	4,685	0,0583	0,0568
-3,9	82,95	81,56	174,97	154,5	5,23	5,005	0,0636	0,0608
0	82,93	81,52	174,99	154,38	5,27	5,035	0,0641	0,0612
3,9	82,99	81,68	174,82	154,44	5,075	5,115	0,0616	0,0621
7,8	83,14	81,63	174,4	155,26	4,815	4,755	0,0584	0,0577
11,7	83,33	81,64	173,53	156,47	4,28	4,25	0,0519	0,0515
15,6	83,58	81,91	172,56	157,73	3,535	3,88	0,0427	0,0469
19,5	83,69	81,92	171,89	159,27	3,14	3,17	0,0379	0,0383
23,4	83,94	81,87	170,51	160,64	2,35	2,585	0,0283	0,0312
27,3	83,94	82,23	169,37	161,88	1,6	2,145	0,0193	0,0258
31,2	84,03	82,2	168,71	162,19	1,24	2,02	0,0149	0,0243
35,1	84,05	82,42	168,09	163,49	0,81	1,49	0,0100	0,0179
39	84,08	82,48	167,64	163,94	0,54	1,31	0,0065	0,0157
42,9	84,05	82,29	166,88	165,18	0,27	0,58	0,0032	0,0070
46,8	84,07	82,6	166,39	165,41	0,14	0,63	0,0017	0,0076
50,7	84,1	82,89	166,23	165,52	0,38	0,735	0,0046	0,0090
54,6	83,94	82,58	165,87	165,51	0,325	0,505	0,0039	0,0061
58,5	84,09	82,8	166,05	165,77	0,42	0,56	0,0050	0,0067

B.3. ORMC

Table B.21: Magnetic parameters in function of the y misalignment with lateral displacement of 150 mm

Aluminium Structure - 40 mm - DDP(10+10)+SP(8) - 12+12(b)								
x [mm]	L_3 [μH]	L_4 [μH]	L_{t+} [μH]	L_{t-} [μH]	M_+ [μH]	M_- [μH]	k_+	k_-
-58,5	84,3	82,52	166,79	165,28	0,015	0,77	0,0002	0,0092
-54,6	84,33	82,49	166,76	165,48	0,03	0,67	0,0004	0,0080
-50,7	84,3	82,46	166,57	165,79	0,095	0,485	0,0011	0,0058
-46,8	84,24	82,4	166,47	165,74	0,085	0,45	0,0010	0,0054
-42,9	84,27	82,33	166,29	165,75	0,155	0,425	0,0019	0,0051
-39	84,18	82,3	166,28	165,95	0,1	0,265	0,0012	0,0032
-35,1	84,18	82,36	166,03	165,93	0,255	0,305	0,0031	0,0037
-31,2	84,11	82,25	166,14	165,87	0,11	0,245	0,0013	0,0029
-27,3	83,98	82,19	166,56	165,41	0,195	0,38	0,0023	0,0046
-23,4	83,81	82,17	166,48	165,37	0,25	0,305	0,0030	0,0037
-19,5	83,58	82,12	166,35	164,8	0,325	0,45	0,0039	0,0054
-15,6	83,27	82,11	165,95	164,52	0,285	0,43	0,0034	0,0052
-11,7	82,82	82,08	165,78	163,77	0,44	0,565	0,0053	0,0069
-7,8	82,55	82,03	165,83	163,49	0,625	0,545	0,0076	0,0066
-3,9	82,41	81,96	165,69	163,13	0,66	0,62	0,0080	0,0075
0	82,37	81,93	165,64	162,92	0,67	0,69	0,0082	0,0084
3,9	82,41	81,92	165,62	163	0,645	0,665	0,0079	0,0081
7,8	82,78	81,96	165,94	163,37	0,6	0,685	0,0073	0,0083
11,7	82,82	82	165,75	163,72	0,465	0,55	0,0056	0,0067
15,6	83,39	82,03	166,34	163,9	0,46	0,76	0,0056	0,0092
19,5	83,67	82,13	166,48	164,64	0,34	0,58	0,0041	0,0070
23,4	83,86	82,24	166,59	165,2	0,245	0,45	0,0030	0,0054
27,3	84,16	82,23	166,65	165,35	0,13	0,52	0,0016	0,0063
31,2	84,16	82,18	166,64	165,33	0,15	0,505	0,0018	0,0061
35,1	84,21	82,31	166,23	165,31	0,145	0,605	0,0017	0,0073
39	84,29	82,34	166,86	165,31	0,115	0,66	0,0014	0,0079
42,9	84,16	82,26	166,6	166,03	0,09	0,195	0,0011	0,0023
46,8	84,38	82,56	166,52	166,12	0,21	0,41	0,0025	0,0049
50,7	84,32	82,65	166,73	166,16	0,12	0,405	0,0014	0,0049
54,6	84,31	82,55	166,64	166,13	0,11	0,365	0,0013	0,0044
58,5	84,22	82,62	166,72	166,07	0,06	0,385	0,0007	0,0046

B. DETAILED RESULTS FROM CHAPTER 4

Table B.22: Magnetic parameters in function of the y misalignment with lateral displacement of 200 mm

Aluminium Structure - 40 mm - DDP(10+10)+SP(8) - 12+12(b)								
x [mm]	L_3 [μH]	L_4 [μH]	L_{t+} [μH]	L_{t-} [μH]	M_+ [μH]	M_- [μH]	k_+	k_-
-58,5	83,81	82,43	166,15	165,02	0,045	0,61	0,0005	0,0073
-54,6	83,81	82,35	166,07	164,86	0,045	0,65	0,0005	0,0078
-50,7	83,88	82,17	165,9	164,89	0,075	0,58	0,0009	0,0070
-46,8	83,82	82,25	166,1	164,79	0,015	0,64	0,0002	0,0077
-42,9	83,75	81,98	166,34	165,05	0,305	0,34	0,0037	0,0041
-39	83,85	81,92	166,33	164,71	0,28	0,53	0,0034	0,0064
-35,1	83,78	81,78	166,52	164,42	0,48	0,57	0,0058	0,0069
-31,2	83,74	81,72	166,89	163,98	0,715	0,74	0,0086	0,0089
-27,3	83,73	81,72	167,34	163,48	0,945	0,985	0,0114	0,0119
-23,4	83,56	81,57	168,12	162,82	1,495	1,155	0,0181	0,0140
-19,5	83,37	81,55	168,52	161,88	1,8	1,52	0,0218	0,0184
-15,6	83,23	81,58	169,4	160,8	2,295	2,005	0,0279	0,0243
-11,7	83,02	81,48	170,09	159,69	2,795	2,405	0,0340	0,0292
-7,8	82,91	81,59	170,32	159,08	2,91	2,71	0,0354	0,0329
-3,9	82,87	81,49	170,72	158,67	3,18	2,845	0,0387	0,0346
0	82,77	81,52	170,79	158,35	3,25	2,97	0,0396	0,0362
3,9	82,83	81,41	170,23	158,69	2,995	2,775	0,0365	0,0338
7,8	82,98	81,54	170,04	159,52	2,76	2,5	0,0336	0,0304
11,7	83,14	81,32	169,31	160,49	2,425	1,985	0,0295	0,0241
15,6	83,34	81,56	168,4	161,68	1,75	1,61	0,0212	0,0195
19,5	83,44	81,31	167,54	162,42	1,395	1,165	0,0169	0,0141
23,4	83,61	81,66	166,83	163,31	0,78	0,98	0,0094	0,0119
27,3	83,69	81,77	165,93	164,29	0,235	0,585	0,0028	0,0071
31,2	83,79	81,78	165,31	164,61	0,13	0,48	0,0016	0,0058
35,1	83,83	82,02	165,17	164,94	0,34	0,455	0,0041	0,0055
39	83,83	81,8	165,29	165,27	0,17	0,18	0,0021	0,0022
42,9	83,85	82,17	165,14	164,98	0,44	0,52	0,0053	0,0063
46,8	83,9	82,02	165,35	165,06	0,285	0,43	0,0034	0,0052
50,7	83,83	82,32	165,32	165,13	0,415	0,51	0,0050	0,0061
54,6	83,91	82,46	165,32	165,21	0,525	0,58	0,0063	0,0070
58,5	83,94	82,5	165,36	165,12	0,54	0,66	0,0065	0,0079

B.3. ORMC

Table B.23: Magnetic parameters in function of the y misalignment with lateral displacement of 250 mm

Aluminium Structure - 40 mm - DDP(10+10)+SP(8) - 12+12(b)								
x [mm]	L_3 [μH]	L_4 [μH]	L_{t+} [μH]	L_{t-} [μH]	M_+ [μH]	M_- [μH]	k_+	k_-
-58,5	84,32	83,06	166,21	164,49	0,585	1,445	0,0070	0,0173
-54,6	84,17	83,09	167,37	165,92	0,055	0,67	0,0007	0,0080
-50,7	84,4	83,03	167,54	165,95	0,055	0,74	0,0007	0,0088
-46,8	84,31	83,03	167,77	165,97	0,215	0,685	0,0026	0,0082
-42,9	84,34	82,91	167,85	165,78	0,3	0,735	0,0036	0,0088
-39	84,32	82,68	168,31	165,36	0,655	0,82	0,0078	0,0098
-35,1	84,39	82,69	168,68	164,88	0,8	1,1	0,0096	0,0132
-31,2	84,21	82,72	169,31	164,22	1,19	1,355	0,0143	0,0162
-27,3	84,27	82,55	170,04	163,22	1,61	1,8	0,0193	0,0216
-23,4	84,25	82,58	171,14	162,08	2,155	2,375	0,0258	0,0285
-19,5	84,24	82,54	172,38	160,88	2,8	2,95	0,0336	0,0354
-15,6	84,25	82,47	173,73	159,62	3,505	3,55	0,0420	0,0426
-11,7	84,31	82,3	174,73	158,21	4,06	4,2	0,0487	0,0504
-7,8	84,34	82,45	175,64	157,28	4,425	4,755	0,0531	0,0570
-3,9	84,27	82,42	176,32	156,47	4,815	5,11	0,0578	0,0613
0	84,32	82,28	176,33	156,34	4,865	5,13	0,0584	0,0616
3,9	84,25	82,27	175,98	156,72	4,73	4,9	0,0568	0,0589
7,8	84,43	82,27	174,99	157,86	4,145	4,42	0,0497	0,0530
11,7	84,3	82,38	174,33	158,75	3,825	3,965	0,0459	0,0476
15,6	84,38	82,51	173,38	159,7	3,245	3,595	0,0389	0,0431
19,5	84,33	82,42	172,24	161,05	2,745	2,85	0,0329	0,0342
23,4	84,31	82,5	170,8	162,36	1,995	2,225	0,0239	0,0267
27,3	84,38	82,5	169,91	163,33	1,515	1,775	0,0182	0,0213
31,2	84,34	82,56	169,01	164,51	1,055	1,195	0,0126	0,0143
35,1	84,39	82,63	168,28	165,07	0,63	0,975	0,0075	0,0117
39	84,38	82,68	167,97	165,46	0,455	0,8	0,0054	0,0096
42,9	84,38	82,79	167,45	165,59	0,14	0,79	0,0017	0,0095
46,8	84,33	82,81	167,72	165,82	0,29	0,66	0,0035	0,0079
50,7	84,38	82,91	167,79	165,89	0,25	0,7	0,0030	0,0084
54,6	84,33	83	167,34	165,8	0,005	0,765	0,0001	0,0091
58,5	84,4	82,99	167,55	166,13	0,08	0,63	0,0010	0,0075

B. DETAILED RESULTS FROM CHAPTER 4

Table B.24: Magnetic parameters in function of the y misalignment with lateral displacement of 300 mm

Aluminium Structure - 40 mm - DDP(10+10)+SP(8) - 12+12(b)								
x [mm]	L_3 [μH]	L_4 [μH]	L_{t+} [μH]	L_{t-} [μH]	M_+ [μH]	M_- [μH]	k_+	k_-
-58,5	84,02	82,68	165,95	165,17	0,375	0,765	0,0045	0,0092
-54,6	83,82	82,43	166,21	164,98	0,02	0,635	0,0002	0,0076
-50,7	83,86	82,05	166,82	164,96	0,455	0,475	0,0055	0,0057
-46,8	83,84	82,08	166,53	164,73	0,305	0,595	0,0037	0,0072
-42,9	83,87	81,94	166,84	164,67	0,515	0,57	0,0062	0,0069
-39	83,9	81,89	166,84	164,56	0,525	0,615	0,0063	0,0074
-35,1	84,18	81,79	167,42	164,24	0,725	0,865	0,0087	0,0104
-31,2	84,11	81,83	167,9	163,83	0,98	1,055	0,0118	0,0127
-27,3	84,02	81,63	168,8	163,28	1,575	1,185	0,0190	0,0143
-23,4	84,13	81,69	169,72	162,45	1,95	1,685	0,0235	0,0203
-19,5	84,04	81,49	170,4	161,51	2,435	2,01	0,0294	0,0243
-15,6	84,26	81,49	171,37	160,58	2,81	2,585	0,0339	0,0312
-11,7	84,21	81,34	172,35	159,73	3,4	2,91	0,0411	0,0352
-7,8	84,28	81,38	173,56	158,68	3,95	3,49	0,0477	0,0421
-3,9	84,36	81,33	174,55	157,95	4,43	3,87	0,0535	0,0467
0	84,56	81,36	174,86	157,58	4,47	4,17	0,0539	0,0503
3,9	84,47	81,38	174,6	157,54	4,375	4,155	0,0528	0,0501
7,8	84,61	81,16	173,83	157,4	4,03	4,185	0,0486	0,0505
11,7	84,35	81,16	173,29	158,15	3,89	3,68	0,0470	0,0445
15,6	84,29	81,18	172,27	159,16	3,4	3,155	0,0411	0,0381
19,5	84,27	81,15	171,07	160,31	2,825	2,555	0,0342	0,0309
23,4	84,14	81,35	169,96	161,54	2,235	1,975	0,0270	0,0239
27,3	84,06	81,43	168,81	162,42	1,66	1,535	0,0201	0,0186
31,2	84,24	81,46	167,97	163,52	1,135	1,09	0,0137	0,0132
35,1	84,29	81,7	167,16	164,27	0,585	0,86	0,0070	0,0104
39	83,84	81,8	166,67	164,54	0,515	0,55	0,0062	0,0066
42,9	83,86	81,9	166,23	164,8	0,235	0,48	0,0028	0,0058
46,8	83,91	81,97	166,22	165,38	0,17	0,25	0,0020	0,0030
50,7	84,1	81,97	165,82	165,42	0,125	0,325	0,0015	0,0039
54,6	84,35	82,6	165,84	165,07	0,555	0,94	0,0066	0,0113
58,5	84,46	82,42	165,59	165,21	0,645	0,835	0,0077	0,0100

B.3. ORMC

Table B.25: Magnetic parameters in function of the y misalignment with lateral displacement of 350 mm

Aluminium Structure - 40 mm - DDP(10+10)+SP(8) - 12+12(b)								
x [mm]	L_3 [μH]	L_4 [μH]	L_{t+} [μH]	L_{t-} [μH]	M_+ [μH]	M_- [μH]	k_+	k_-
-58,5	84,4	82,82	167,3	165,6	0,04	0,81	0,0005	0,0097
-54,6	84,31	82,58	167,27	165,66	0,19	0,615	0,0023	0,0074
-50,7	84,32	82,66	167,29	165,48	0,155	0,75	0,0019	0,0090
-46,8	84,35	82,55	167,57	165,33	0,335	0,785	0,0040	0,0094
-42,9	84,37	82,47	167,8	165,19	0,48	0,825	0,0058	0,0099
-39	84,36	82,51	168,1	165,04	0,615	0,915	0,0074	0,0110
-35,1	84,38	82,48	168,42	164,52	0,78	1,17	0,0093	0,0140
-31,2	84,4	82,31	168,84	164,06	1,065	1,325	0,0128	0,0159
-27,3	84,44	82,4	169,29	163,66	1,225	1,59	0,0147	0,0191
-23,4	84,33	82,27	170,02	163,34	1,71	1,63	0,0205	0,0196
-19,5	84,24	82,15	170,32	162,62	1,965	1,885	0,0236	0,0227
-15,6	84,28	82,18	170,66	162,17	2,1	2,145	0,0252	0,0258
-11,7	84,33	82,15	170,9	161,63	2,21	2,425	0,0266	0,0291
-7,8	84,29	82,16	171,14	161,41	2,345	2,52	0,0282	0,0303
-3,9	84,34	82,14	171,33	161,3	2,425	2,59	0,0291	0,0311
0	84,25	82,22	171,22	161,07	2,375	2,7	0,0285	0,0324
3,9	84,28	82,06	171,03	161,37	2,345	2,485	0,0282	0,0299
7,8	84,32	82,13	170,8	161,73	2,175	2,36	0,0261	0,0284
11,7	84,31	82,05	170,53	161,99	2,085	2,185	0,0251	0,0263
15,6	84,32	82,13	170,01	162,42	1,78	2,015	0,0214	0,0242
19,5	84,33	82,14	169,71	162,97	1,62	1,75	0,0195	0,0210
23,4	84,31	82,25	168,72	163,53	1,08	1,515	0,0130	0,0182
27,3	84,29	82,5	168,51	163,78	0,86	1,505	0,0103	0,0180
31,2	84,37	82,62	168,4	164,17	0,705	1,41	0,0084	0,0169
35,1	84,32	82,6	167,89	165	0,485	0,96	0,0058	0,0115
39	84,31	82,67	167,64	165,49	0,33	0,745	0,0040	0,0089
42,9	84,43	82,55	167,38	165,82	0,2	0,58	0,0024	0,0069
46,8	84,39	82,91	167,38	165,66	0,04	0,82	0,0005	0,0098
50,7	84,38	82,9	166,96	166,55	0,16	0,365	0,0019	0,0044
54,6	84,39	82,99	166,96	166,84	0,21	0,27	0,0025	0,0032
58,5	84,36	82,97	167,35	165,93	0,01	0,7	0,0001	0,0084

B. DETAILED RESULTS FROM CHAPTER 4

Table B.26: Magnetic parameters in function of the y misalignment with lateral displacement of 400 mm

Aluminium Structure - 40 mm - DDP(10+10)+SP(8) - 12+12(b)								
x [mm]	L_3 [μH]	L_4 [μH]	L_{t+} [μH]	L_{t-} [μH]	M_+ [μH]	M_- [μH]	k_+	k_-
-58,5	84,36	82,57	166,82	165,17	0,055	0,88	0,0007	0,0105
-54,6	84,36	82,57	166,82	165,17	0,055	0,88	0,0007	0,0105
-50,7	84,27	82,51	166,73	165,14	0,025	0,82	0,0003	0,0098
-46,8	84,34	82,56	166,86	165	0,02	0,95	0,0002	0,0114
-42,9	84,29	82,34	166,79	164,93	0,08	0,85	0,0010	0,0102
-39	84,39	82,16	167,11	164,73	0,28	0,91	0,0034	0,0109
-35,1	84,27	82,26	167,34	164,68	0,405	0,925	0,0049	0,0111
-31,2	84,33	81,97	167,66	164,57	0,68	0,865	0,0082	0,0104
-27,3	84,38	82,01	168,05	164,37	0,83	1,01	0,0100	0,0121
-23,4	84,38	81,96	167,89	163,95	0,775	1,195	0,0093	0,0144
-19,5	84,33	81,77	168,32	163,67	1,11	1,215	0,0134	0,0146
-15,6	84,3	81,81	168,47	163,42	1,18	1,345	0,0142	0,0162
-11,7	84,26	81,73	168,66	163,22	1,335	1,385	0,0161	0,0167
-7,8	84,23	81,72	168,8	162,93	1,425	1,51	0,0172	0,0182
-3,9	84,26	81,59	168,71	162,69	1,43	1,58	0,0172	0,0191
0	84,14	81,56	168,73	162,67	1,515	1,515	0,0183	0,0183
3,9	84,28	81,51	168,61	162,69	1,41	1,55	0,0170	0,0187
7,8	84,27	81,62	168,62	162,82	1,365	1,535	0,0165	0,0185
11,7	84,18	81,43	168,24	162,81	1,315	1,4	0,0159	0,0169
15,6	84,15	81,49	168,1	163,36	1,23	1,14	0,0149	0,0138
19,5	84,35	81,5	167,6	163,46	0,875	1,195	0,0106	0,0144
23,4	84,21	81,71	167,54	163,73	0,81	1,095	0,0098	0,0132
27,3	84,47	81,69	167,13	164,13	0,485	1,015	0,0058	0,0122
31,2	84,51	81,78	167,12	164,41	0,415	0,94	0,0050	0,0113
35,1	84,39	82,02	166,68	164,34	0,135	1,035	0,0016	0,0124
39	84,12	82,23	166,49	164,77	0,07	0,79	0,0008	0,0095
42,9	84,21	82,1	166,28	164,96	0,015	0,675	0,0002	0,0081
46,8	84,23	82,15	166,1	165,11	0,14	0,635	0,0017	0,0076
50,7	84,15	82,19	165,92	164,9	0,21	0,72	0,0025	0,0087
54,6	84,35	82,2	165,81	165,1	0,37	0,725	0,0044	0,0087
58,5	84,3	82,25	165,83	165,24	0,36	0,655	0,0043	0,0079

B.3. ORMC

Table B.27: Magnetic parameters in function of the y misalignment with lateral displacement of 450 mm

Aluminium Structure - 40 mm - DDP(10+10)+SP(8) - 12+12(b)								
x [mm]	L_3 [μH]	L_4 [μH]	L_{t+} [μH]	L_{t-} [μH]	M_+ [μH]	M_- [μH]	k_+	k_-
-58,5	84,25	82,73	167,12	165,98	0,07	0,5	0,0008	0,0060
-54,6	84,43	82,53	167	165,71	0,02	0,625	0,0002	0,0075
-50,7	84,29	82,52	167,22	165,78	0,205	0,515	0,0025	0,0062
-46,8	84,32	82,38	167,38	165,89	0,34	0,405	0,0041	0,0049
-42,9	84,34	82,32	167,49	165,67	0,415	0,495	0,0050	0,0059
-39	84,3	82,32	167,48	165,45	0,43	0,585	0,0052	0,0070
-35,1	84,33	82,12	167,53	165,15	0,54	0,65	0,0065	0,0078
-31,2	84,27	82,46	167,73	165,23	0,5	0,75	0,0060	0,0090
-27,3	84,48	82,08	167,96	165,12	0,7	0,72	0,0084	0,0086
-23,4	84,32	82,05	167,78	165,09	0,705	0,64	0,0085	0,0077
-19,5	84,25	82,08	167,82	164,81	0,745	0,76	0,0090	0,0091
-15,6	84,2	82,04	167,89	164,84	0,825	0,7	0,0099	0,0084
-11,7	84,16	82,03	167,87	164,59	0,84	0,8	0,0101	0,0096
-7,8	84,16	82,06	167,91	164,5	0,845	0,86	0,0102	0,0103
-3,9	84,09	81,99	167,79	164,5	0,855	0,79	0,0103	0,0095
0	84,16	81,94	167,82	164,45	0,86	0,825	0,0104	0,0099
3,9	84,15	82,02	167,87	164,45	0,85	0,86	0,0102	0,0104
7,8	84,28	82,09	167,96	164,66	0,795	0,855	0,0096	0,0103
11,7	84,25	82,08	167,87	164,85	0,77	0,74	0,0093	0,0089
15,6	84,32	82,13	167,79	164,92	0,67	0,765	0,0081	0,0092
19,5	84,33	82,1	167,73	165,16	0,65	0,635	0,0078	0,0076
23,4	84,32	82,15	167,72	165,23	0,625	0,62	0,0075	0,0074
27,3	84,31	82,24	167,68	165,27	0,565	0,64	0,0068	0,0077
31,2	84,25	82,28	167,67	165,37	0,57	0,58	0,0068	0,0070
35,1	84,23	82,34	167,57	165,65	0,5	0,46	0,0060	0,0055
39	84,3	82,41	167,54	165,88	0,415	0,415	0,0050	0,0050
42,9	84,29	82,56	167,38	166,3	0,265	0,275	0,0032	0,0033
46,8	84,33	82,68	167,31	166,45	0,15	0,28	0,0018	0,0034
50,7	84,22	82,79	167,33	166,45	0,16	0,28	0,0019	0,0034
54,6	84,21	82,65	167,2	166,19	0,17	0,335	0,0020	0,0040
58,5	84,21	82,64	167,12	166,58	0,135	0,135	0,0016	0,0016

C Detailed Results from Chapter 5

C.1 Measurement Blocks and Calculations

C.2 Impact of the Velocity

This section presents the detailed simulation results of the study of the impact of the velocity of the EV on the energy transferred. Two different sets of tests were made, one with a fixed time frame of 0,5 seconds, and another with a fixed number of ORMC transmitter pads of 8 pads. The test was repeated for three velocities and two d_{pads} .

C.2.1 Time framed

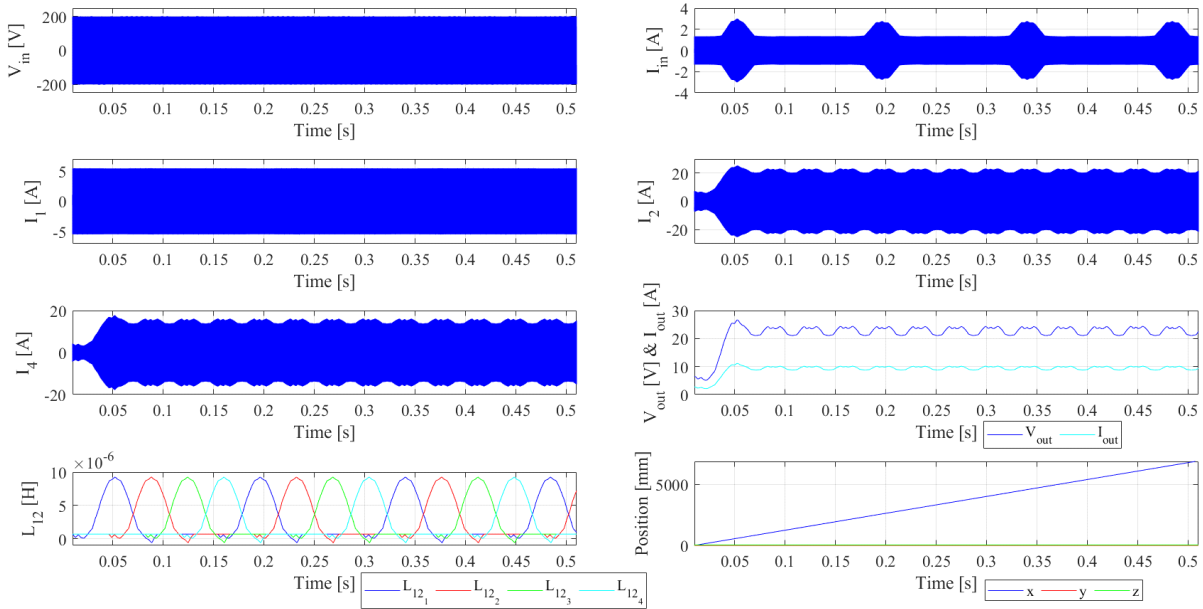


Figure C.1: Simulation results for the impact of the vehicle velocity, 50 km/h with a distance between pads of 500 mm . v_{in} , i_{in} , i_1 , i_2 , i_4 , v_{out} , i_{out} , L_{12} and x , y and z position.

C.2. IMPACT OF THE VELOCITY

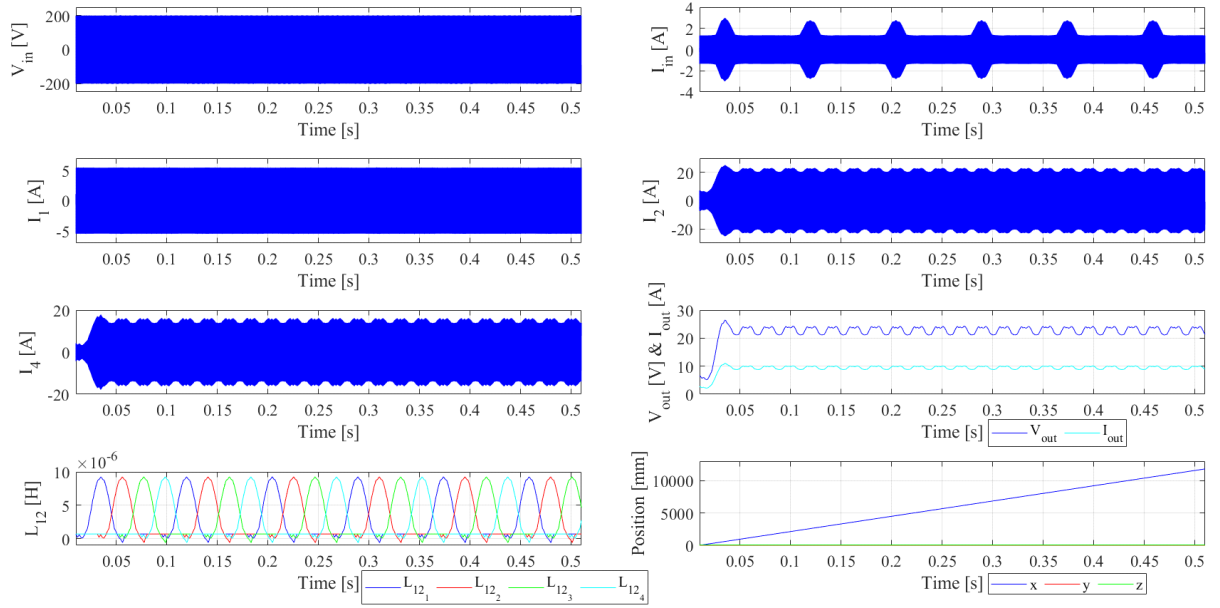


Figure C.2: Simulation results for the impact of the vehicle velocity, 85 km/h with a distance between pads of 500 mm . v_{in} , i_{in} , i_1 , i_2 , i_4 , v_{out} , i_{out} , L_{12} and x , y and z position.

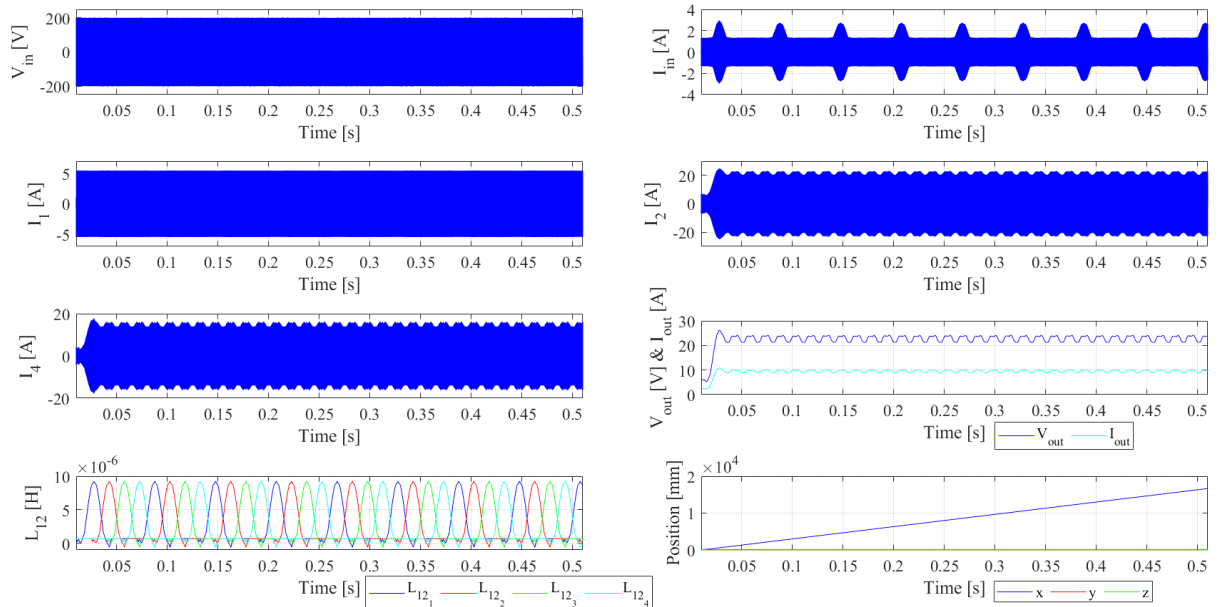


Figure C.3: Simulation results for the impact of the vehicle velocity, 120 km/h with a distance between pads of 500 mm . v_{in} , i_{in} , i_1 , i_2 , i_4 , v_{out} , i_{out} , L_{12} and x , y and z position.

C. DETAILED RESULTS FROM CHAPTER 5

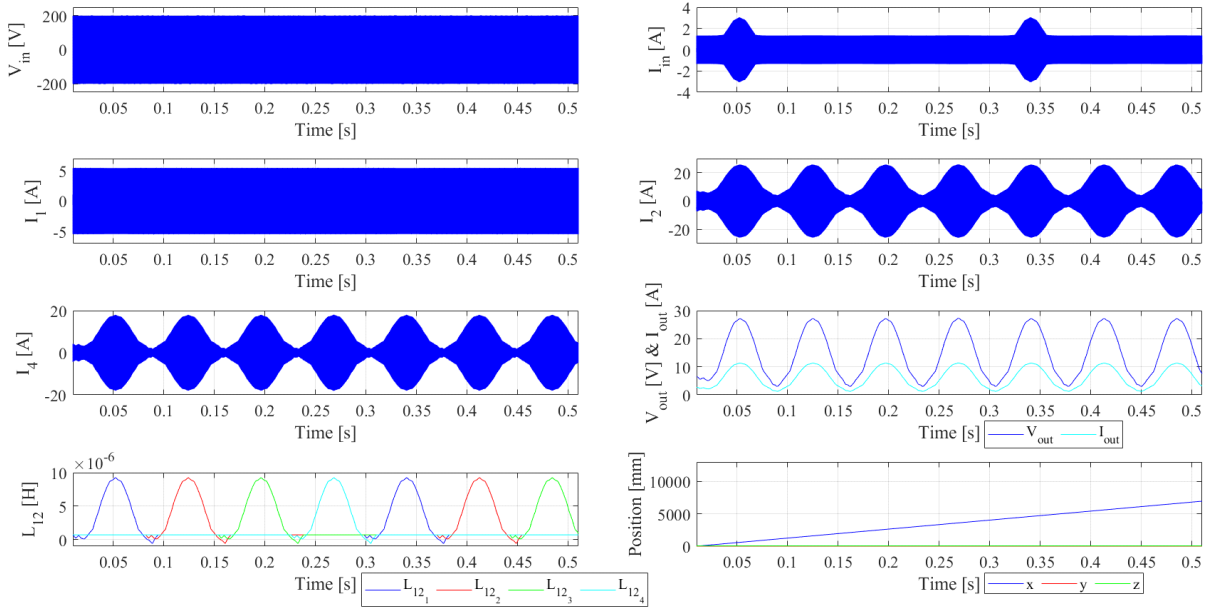


Figure C.4: Simulation results for the impact of the vehicle velocity, 50 *km/h* with a distance between pads of 1000 *mm*. v_{in} , i_{in} , i_1 , i_2 , i_4 , v_{out} , i_{out} , L_{12} and x , y and z position.

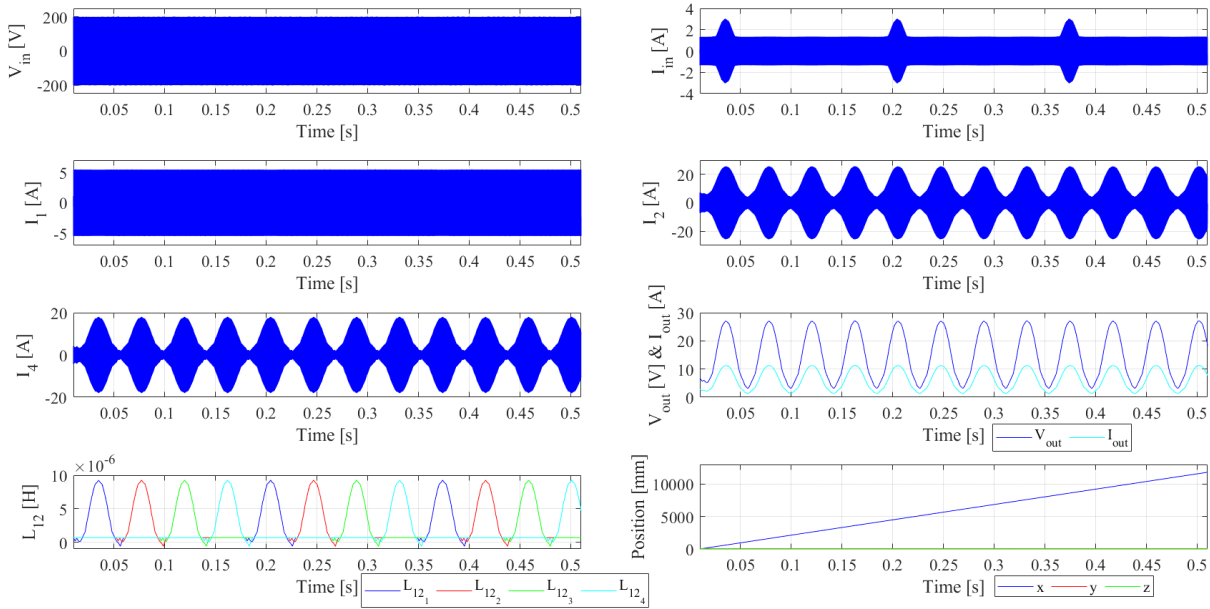


Figure C.5: Simulation results for the impact of the vehicle velocity, 85 *km/h* with a distance between pads of 1000 *mm*. v_{in} , i_{in} , i_1 , i_2 , i_4 , v_{out} , i_{out} , L_{12} and x , y and z position.

C.2. IMPACT OF THE VELOCITY

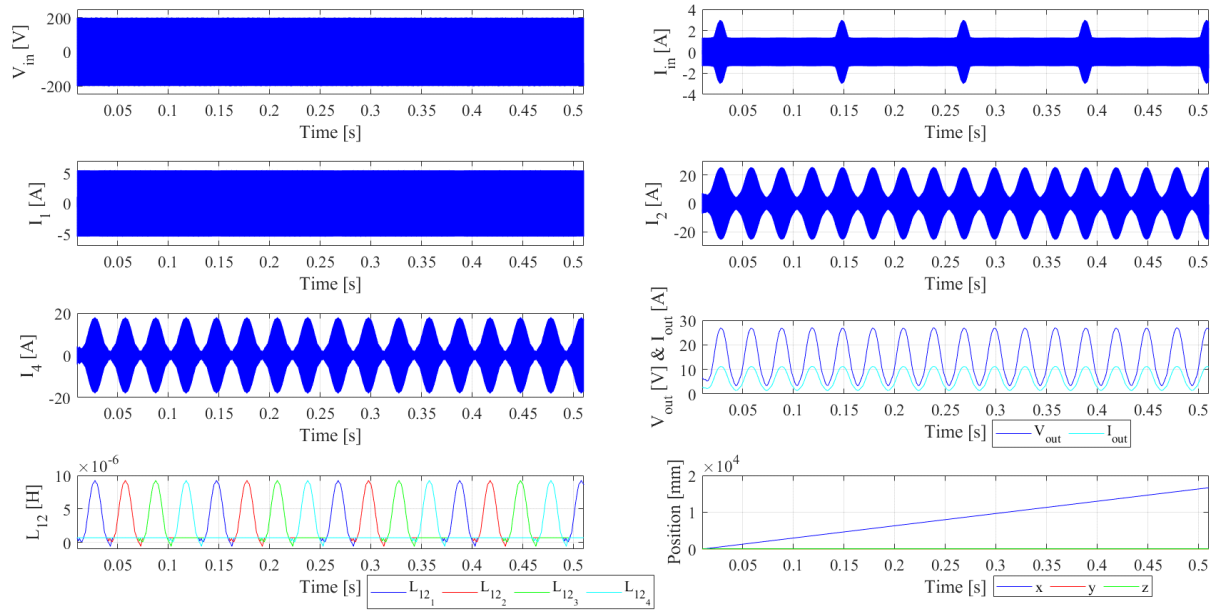


Figure C.6: Simulation results for the impact of the vehicle velocity, 120 *km/h* with a distance between pads of 1000 *mm*. v_{in} , i_{in} , i_1 , i_2 , i_4 , v_{out} , i_{out} , L_{12} and x , y and z position.

C.2.2 Number of transmitter pads

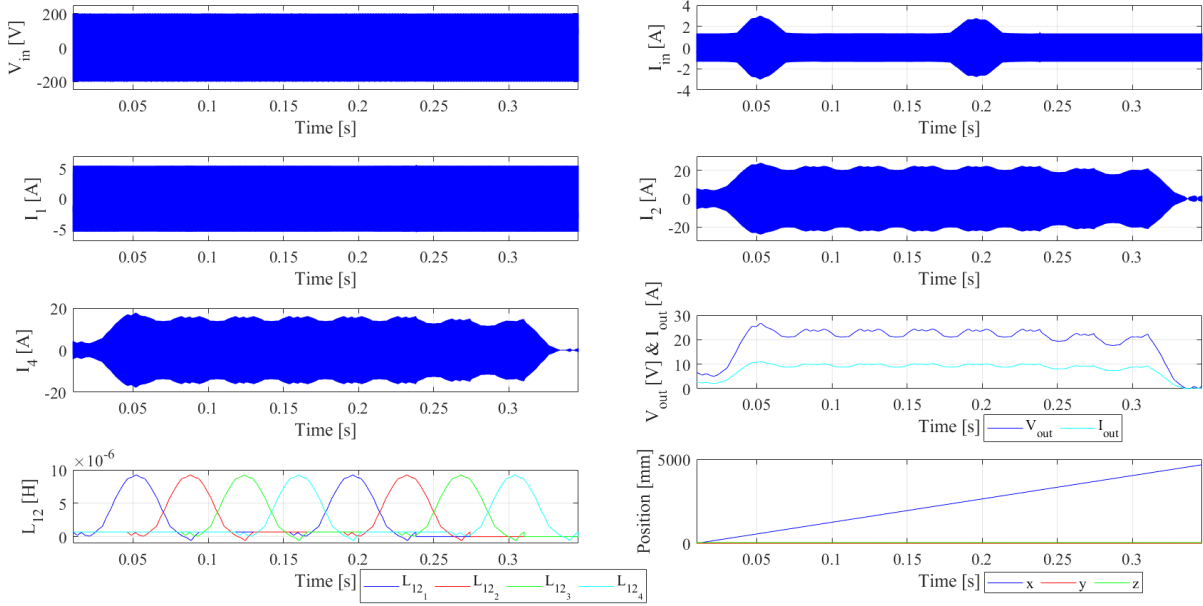


Figure C.7: Simulation results for the impact of the vehicle velocity, 50 km/h with a distance between pads of 500 mm . v_{in} , i_{in} , i_1 , i_2 , i_4 , v_{out} , i_{out} , L_{12} and x , y and z position.

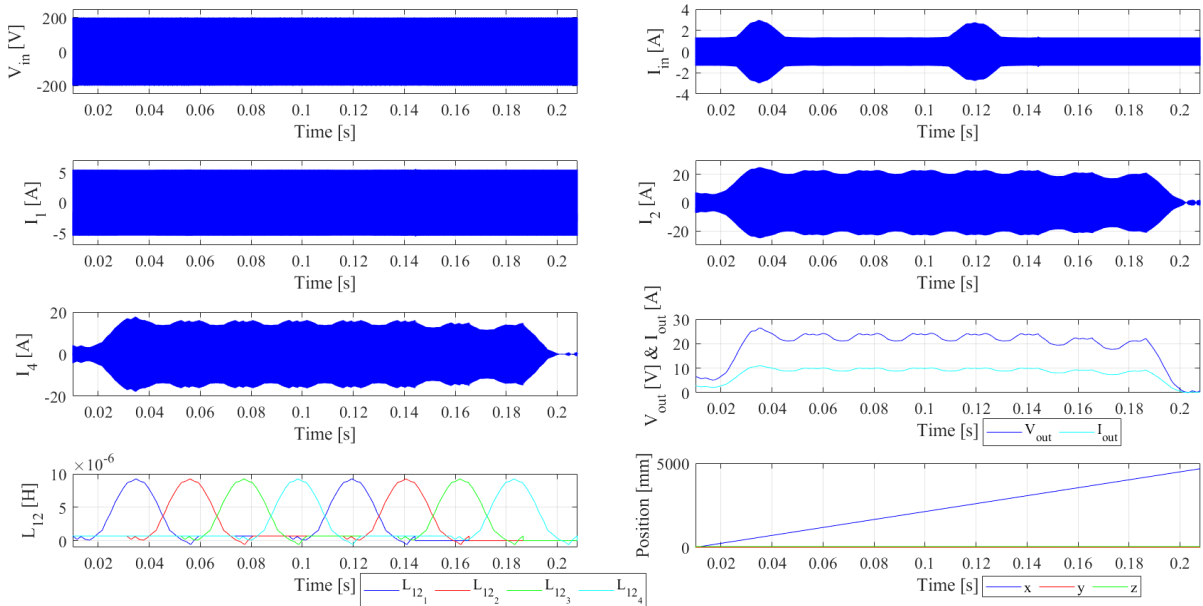


Figure C.8: Simulation results for the impact of the vehicle velocity, 85 km/h with a distance between pads of 500 mm . v_{in} , i_{in} , i_1 , i_2 , i_4 , v_{out} , i_{out} , L_{12} and x , y and z position.

C.2. IMPACT OF THE VELOCITY

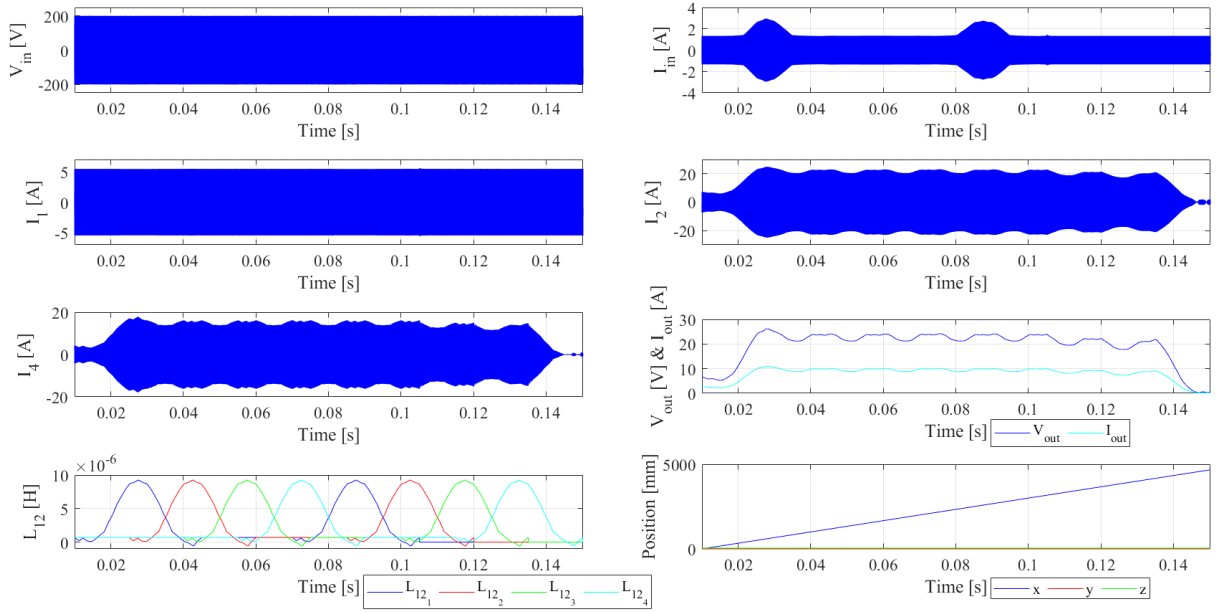


Figure C.9: Simulation results for the impact of the vehicle velocity, 120 *km/h* with a distance between pads of 500 *mm*. v_{in} , i_{in} , i_1 , i_2 , i_4 , v_{out} , i_{out} , L_{12} and x , y and z position.

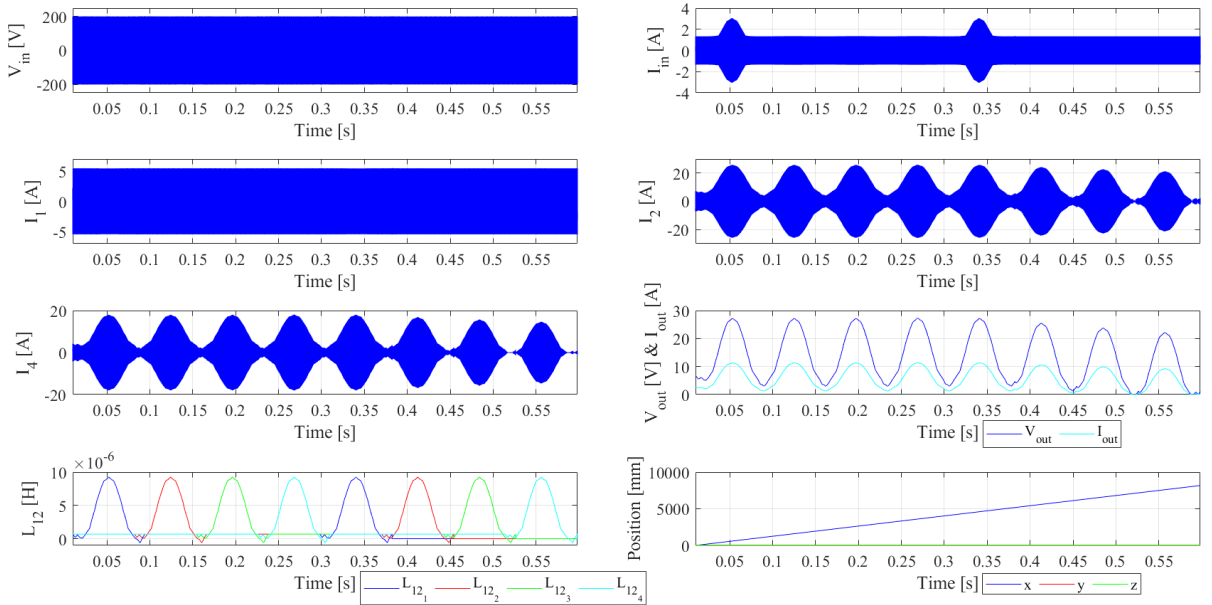


Figure C.10: Simulation results for the impact of the vehicle velocity, 50 *km/h* with a distance between pads of 1000 *mm*. v_{in} , i_{in} , i_1 , i_2 , i_4 , v_{out} , i_{out} , L_{12} and x , y and z position.

C. DETAILED RESULTS FROM CHAPTER 5

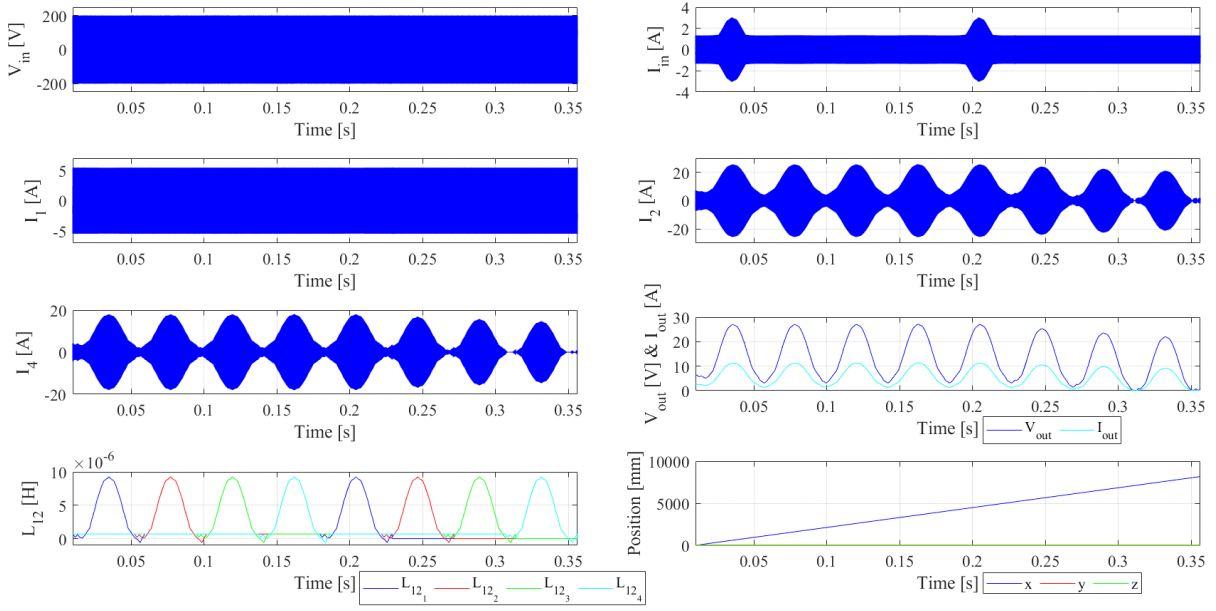


Figure C.11: Simulation results for the impact of the vehicle velocity, 85 km/h with a distance between pads of 1000 mm . v_{in} , i_{in} , i_1 , i_2 , i_4 , v_{out} , i_{out} , L_{12} and x , y and z position.

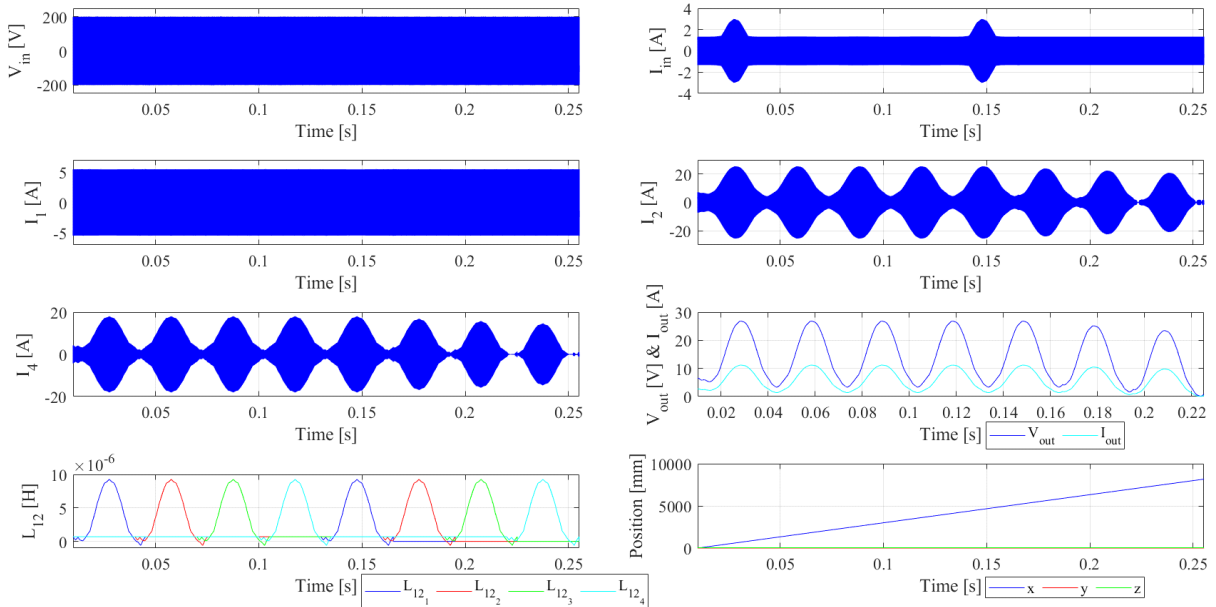


Figure C.12: Simulation results for the impact of the vehicle velocity, 120 km/h with a distance between pads of 1000 mm . v_{in} , i_{in} , i_1 , i_2 , i_4 , v_{out} , i_{out} , L_{12} and x , y and z position.

C.3 Different Source Arrangements

This section shows the detailed simulation results of the study of the impact of arrangements of sources. The behaviour of three different arrangements among three transmitters was compared: each transmitter with a source C.13; all transmitters in parallel powered by one source C.14; and all transmitters in series powered by one source C.15.

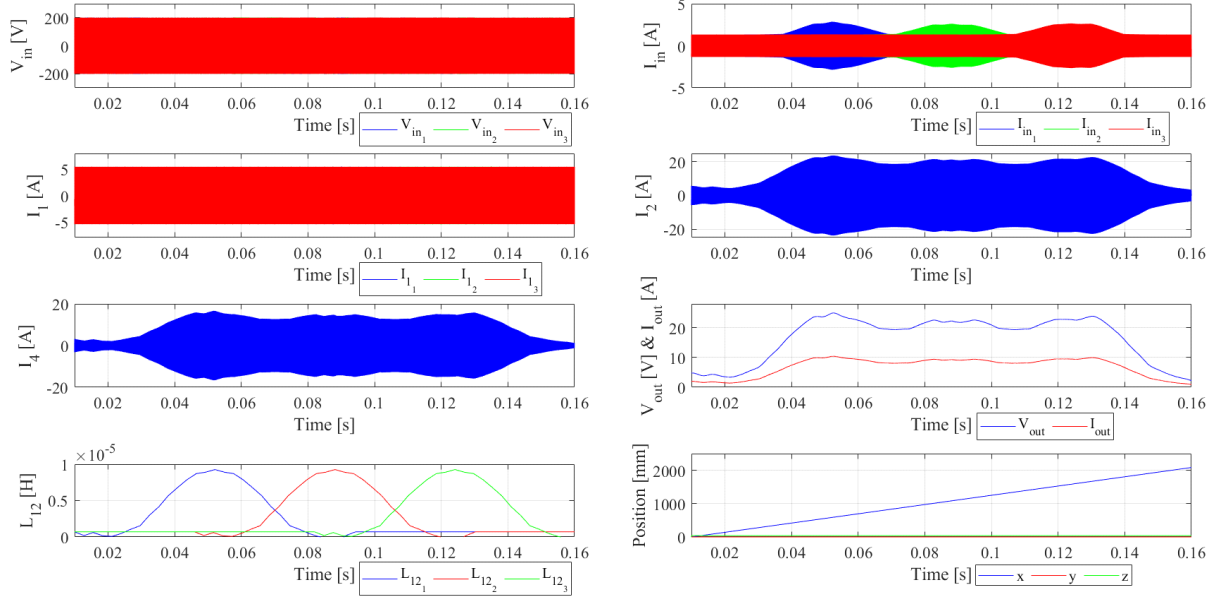


Figure C.13: Simulation results for the impact of the source arrangements, each ORMC transmitter pad powered individually. v_{in} , i_{in} , i_1 , i_2 , i_4 , v_{out} , i_{out} , L_{12} and x , y and z position.

C. DETAILED RESULTS FROM CHAPTER 5

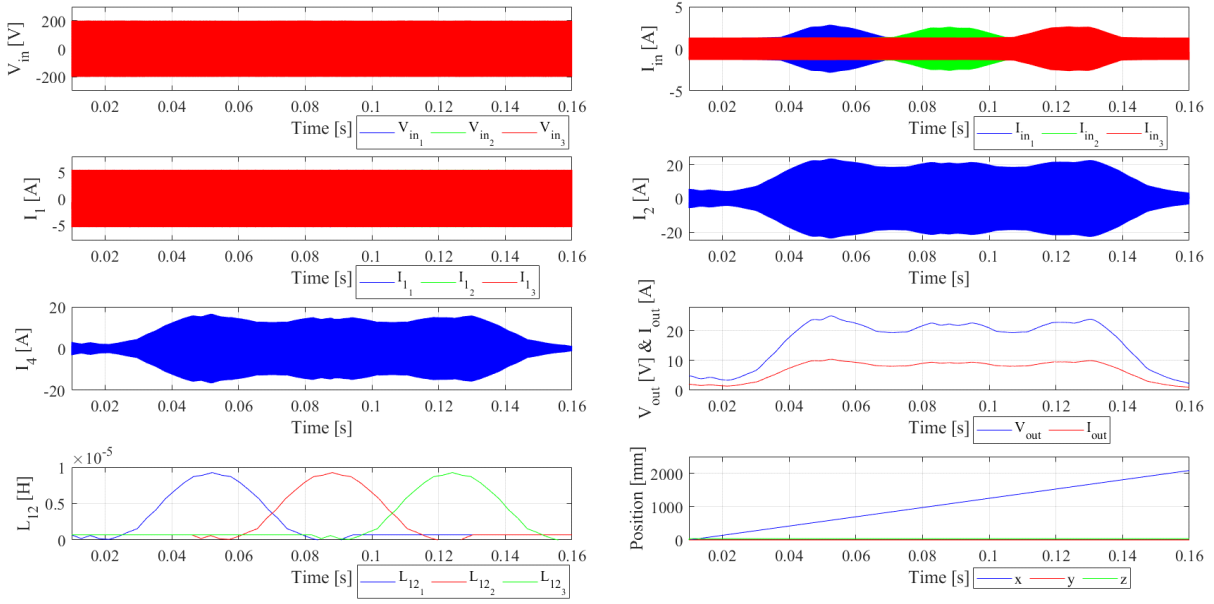


Figure C.14: Simulation results for the impact of the source arrangements, ORMC transmitter pads powered in parallel. v_{in} , i_{in} , i_1 , i_2 , i_4 , v_{out} , i_{out} , L_{10} and x , y and z position.

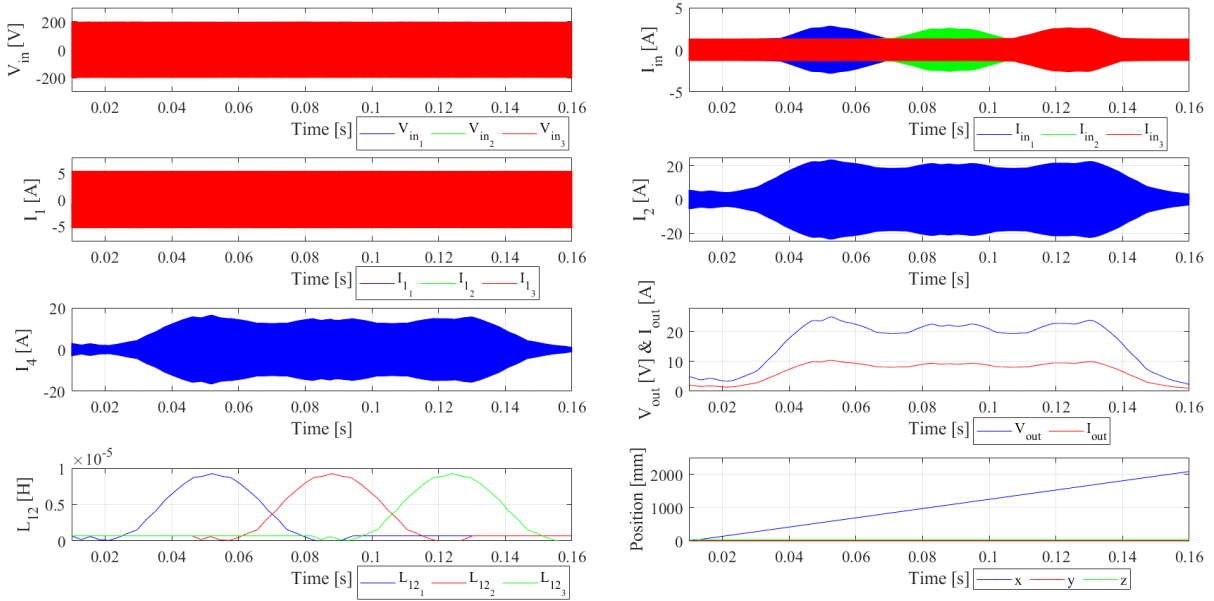


Figure C.15: Simulation results for the impact of the source arrangements, ORMC transmitter pads powered in series. v_{in} , i_{in} , i_1 , i_2 , i_4 , v_{out} , i_{out} , L_{12} and x , y and z position.

D Detailed Results from Chapter 6

D.1 Polarity test

An experimental test was conducted to prove the polarity of the ORMC transmitter pads. The test involves comparing the system's behaviour when it passes through two transmitter pads under two scenarios: one where the pads have the same polarity, and another where the pads have opposite polarities. In Fig. D.1, the results for the scenario where the pads have the same polarity are shown, and in Fig. D.3 on the left is illustrated, the orientation of currents and magnetic fields. In Fig. D.2, the results for the scenario where the pads have the opposite polarity are shown, and on Fig. D.3 on the right is illustrated the orientation of currents and magnetic fields.

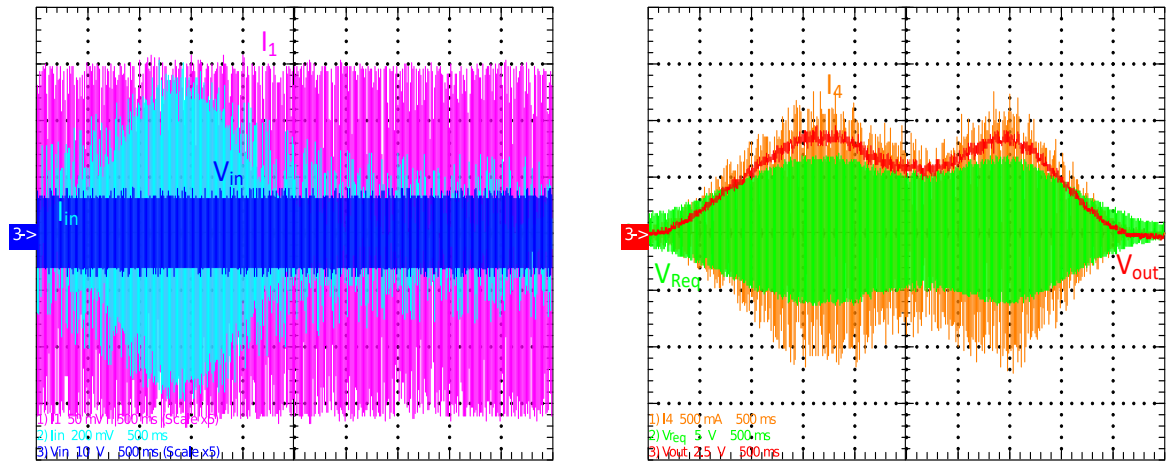


Figure D.1: Experimental results for both pads with the same polarity. On the left v_{in} [50V/div], i_{in} [200, A/div] and i_1 [250mV/div] in blue, cyan, and pink respectively. On the right i_4 [500mA/div], v_{Req} [5V/div], v_{out} [2.5V/div] in orange, green, and red respectively.

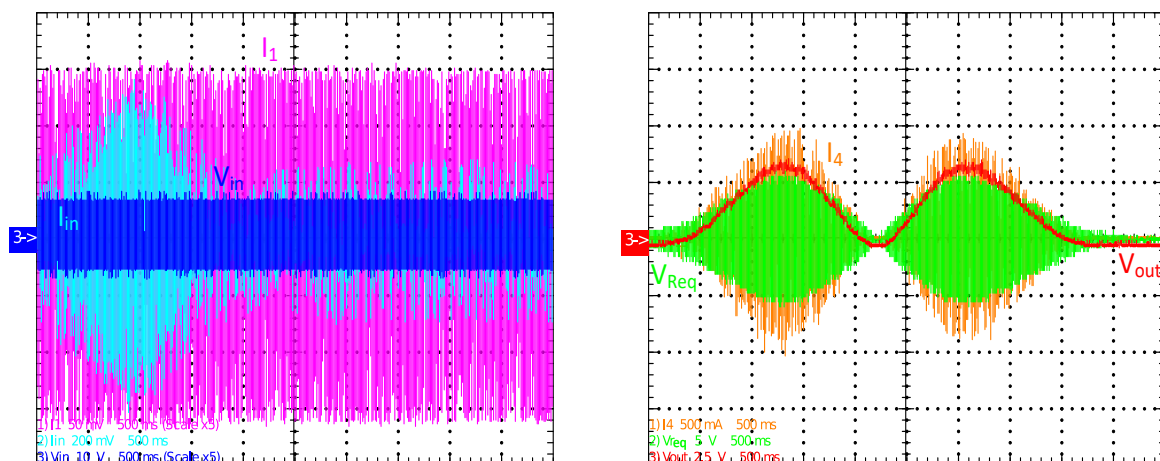


Figure D.2: Experimental results for both pads with the opposite polarity. On the left v_{in} [50V/div], i_{in} [200mA/div] and i_1 [250mV/div] in blue, cyan, and pink respectively. On the right i_4 [500mA/div], v_{Req} [5V/div], v_{out} [2.5V/div] in orange, green, and red respectively.

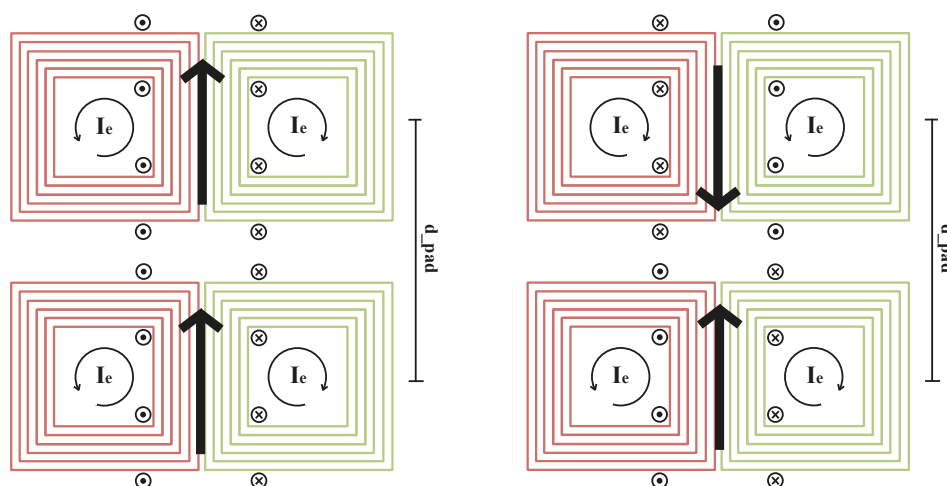


Figure D.3: Illustration of the interaction between two consecutive pads, with currents and magnetic fields denoted. On the left, the pads have the same polarity and on the right the pads have the opposite polarity.

D.2 Experimental Results

The following figures presents the experimental and simulation results of the chapter 6 for a load of $2,4 \Omega$. Figures D.4 and D.5 show the results for the LCL-S-S for a coupled and decoupled situation, respectively. Figure D.6 shows the results for the coupled situation for the S-S-S. Figures D.7 and D.8 are the results for the LCL-S-S for a coupled and decoupled situation, respectively.

D.2.1 LCL-S-S

D.2. EXPERIMENTAL RESULTS

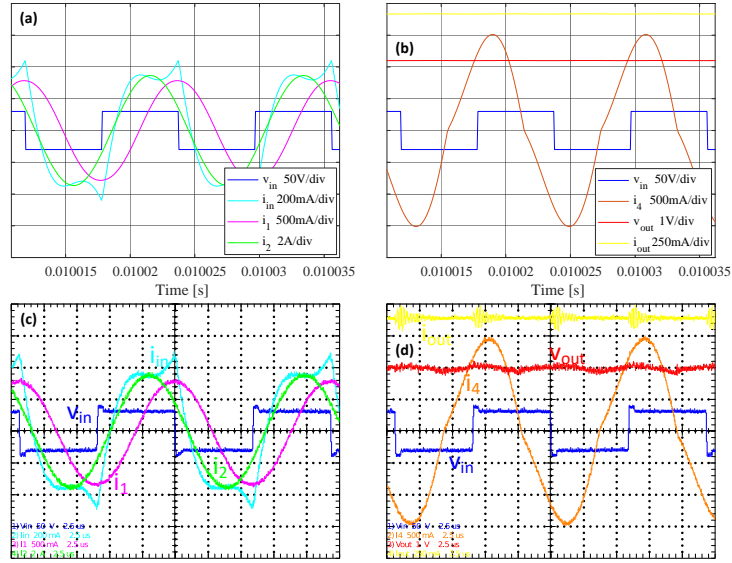


Figure D.4: Static results for a load of $2,4 \Omega$ on an aligned situation. *a)* & *c)* shows v_{in} [50V/div], i_{in} [200mA/div], i_1 [500mA/div] and i_2 [2A/div] in blue, cyan, pink and green, respectively. *b)* and *d)* v_{in} [50V/div], i_4 [500mA/div], v_{out} [1V/div] and i_{out} [250mA/div] in blue, orange, red and yellow, respectively.

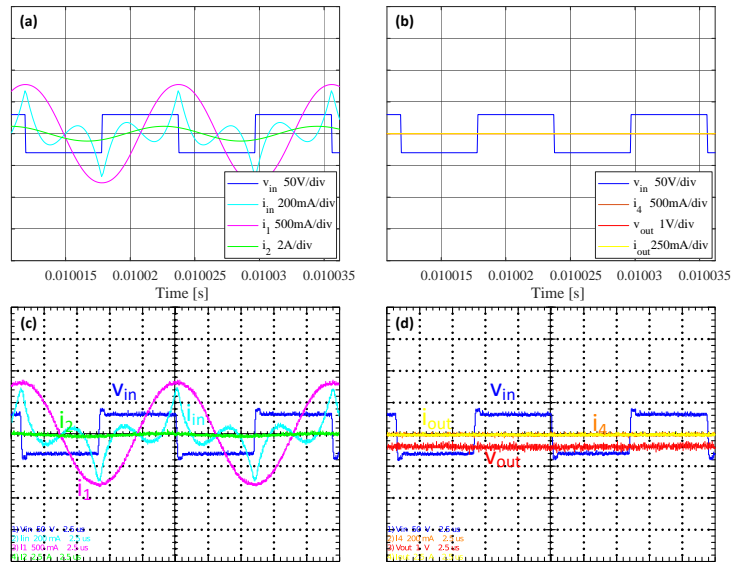


Figure D.5: Static results for a load of $2,4 \Omega$ on a decoupled situation. *a)* & *c)* shows v_{in} [50V/div], i_{in} [200mA/div], i_1 [500mA/div] and i_2 [2A/div] in blue, cyan, pink and green, respectively. *b)* and *d)* v_{in} [50V/div], i_4 [500mA/div], v_{out} [1V/div] and i_{out} [250mA/div] in blue, orange, red and yellow, respectively.

D.2.2 S-S-S

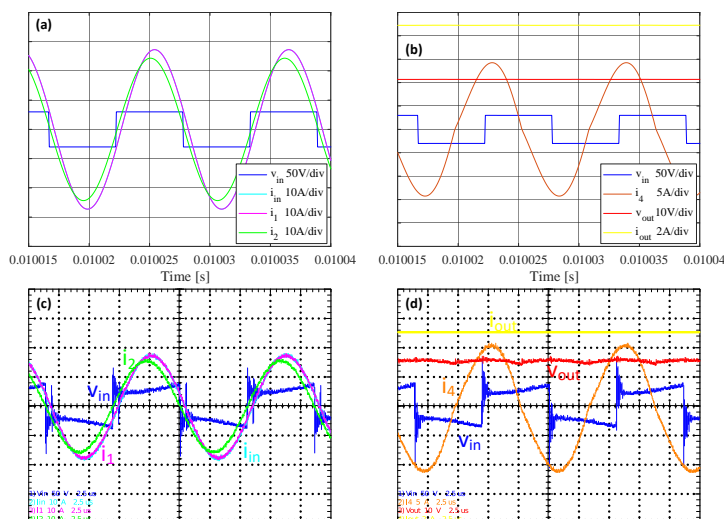


Figure D.6: Static results for a load of 2,4 Ω on an aligned situation. *a)* & *c)* shows v_{in} [50V/div], i_{in} [10A/div], i_1 [10A/div] and i_2 [10A/div] in blue, cyan, pink and green, respectively. *b)* and *d)* v_{in} [50V/div], i_4 [5A/div], v_{out} [10V/div] and i_{out} [2A/div] in blue, orange, red and yellow, respectively.

D.2.3 LCC-S-S

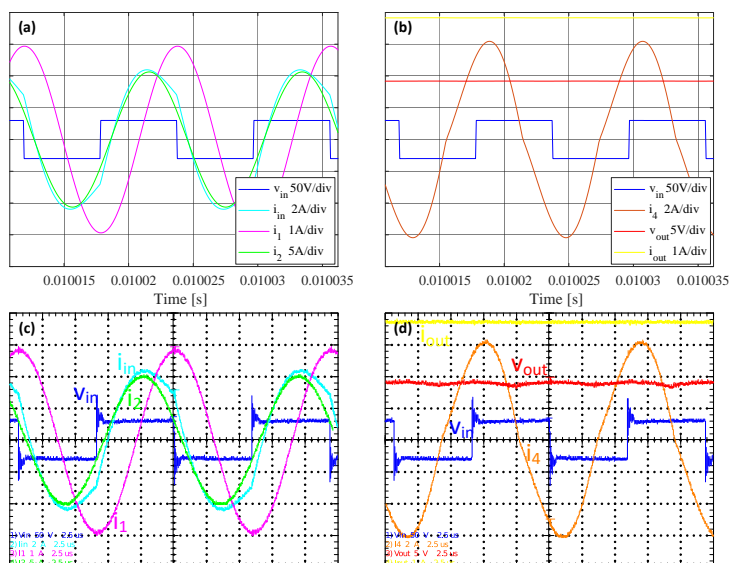


Figure D.7: Static results for a load of 2,4 Ω on an aligned situation. *a)* & *c)* shows v_{in} [50V/div], i_{in} [2A/div], i_1 [1A/div] and i_2 [5A/div] in blue, cyan, pink and green, respectively. *b)* and *d)* v_{in} [50V/div], i_4 [2A/div], v_{out} [5V/div] and i_{out} [1A/div] in blue, orange, red and yellow, respectively.

D.2. EXPERIMENTAL RESULTS

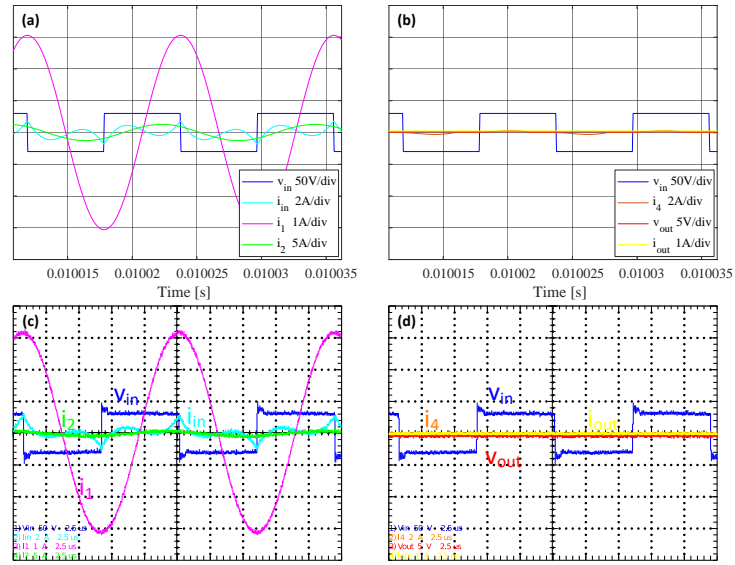


Figure D.8: Static results for a load of 2.4Ω on an decoupled situation. *a)* & *c)* shows v_{in} [50V/div], i_{in} [2A/div], i_1 [1A/div] and i_2 [5A/div] in blue, cyan, pink and green, respectively. *b)* and *d)* v_{in} [50V/div], i_4 [2A/div], v_{out} [5V/div] and i_{out} [1A/div] in blue, orange, red and yellow, respectively.